Mapping Crustal Structure of the Nechako Basin using Teleseismic Receiver Functions

by

Hyun-seung Kim
B.S., University of Washington, 2007

A Thesis Submitted in Partial Fulfillment
of the Requirements for the Degree of

MASTER OF SCIENCE

in the School of Earth and Ocean Sciences

Supervisory Committee

Mapping Crustal Structure of the Nechako Basin using Teleseismic Receiver Functions

by

Hyun-seung Kim
B.S., University of Washington, 2007

Supervisory Committee

Dr. John F. Cassidy (School of Earth and Ocean Sciences)
Co-Supervisor

Dr. Stan E. Dosso (School of Earth and Ocean Sciences)
Co-Supervisor

Dr. Honn Kao (School of Earth and Ocean Sciences)
Departmental Member

Dr. George D. Spence (School of Earth and Ocean Sciences)
Departmental Member

Supervisory Committee
Dr. John F. Cassidy (School of Earth and Ocean Sciences)
Co-Supervisor
Dr. Stan E. Dosso (School of Earth and Ocean Sciences)
Co-Supervisor
Dr. Honn Kao (School of Earth and Ocean Sciences)
Departmental Member
Dr. George D. Spence (School of Earth and Ocean Sciences)
Departmental Member

Abstract

This thesis describes a passive-source seismic mapping project in the Nechako Basin of central British Columbia (BC), Canada, with the ultimate goal of assessing the hydrocarbon and mineral potential of the region. The Nechako Basin has been the focus of limited hydrocarbon exploration since the 1930s. Twelve exploratory wells were drilled; oil stains on drill chip samples and the evidence of gas in drill stem tests attest to some hydrocarbon potential. Seismic data collected in the 1980s were of variable quality due mainly to effects of volcanic cover in this region. For the present study, an array of nine seismic stations was deployed in 2006 and 2007 to sample a wide area of the Nechako Basin and map the sediment thickness, crustal thickness, and overall geometry of the basin. This study utilizes recordings of about 40 distant earthquakes from 2006 to 2008 to calculate receiver functions, and construct S-wave velocity models for each station using the Neighbourhood Algorithm inversion. The surface sediments are found to range in thickness from about 0.8 to 2.7 km, and the volcanic layer below ranges in thickness from 2.3 to 4.7 km. Both sediments and volcanic cover are thickest in the central part of the basin. The average crustal thickness across the basin is about 30-32 km; it is thicker in the northern and western parts of the basin, and thinner in the southern and eastern parts. This study complements other research in this region, such as independent active-source seismic studies and magnetotelluric measurements, by providing site-specific images of the crustal structure down to the Moho and detailed constraints on the S-wave velocity structure.

Table of Contents

List of Tables

List of Figures

Acknowledgments

First, I would like to thank everyone at the SEOS at the UVic and PGC for their time and assistance. Special thanks to my supervisors John Cassidy and Stan Dosso for all support and guidance. I appreciate my committee members for reviewing this thesis; especially to Honn Kao for the suggestions and help for the inversion, and to George Spence for the great courses. I also gratefully acknowledge the financial support of the Geoscience BC, BC Ministry of Enerery, Mines, and Petroleum Resources and the Geological Survey of Canada in deploying and operating this seismic network.

세상에서 제일 사랑하고 존경하는 아빠와 엄마, 계속 공부할 수 있도록 힘이 되어주시는 외할머니, 최고 멋진 우리 큰이모, 미국이모, 막내이모 언제나 믿고 응원해주셔서 감사합니다. 사촌이지만 친동생보다 더 가까운 웅이랑 현정이도 고마워. 인생에 있어서 첫 스승이신 김지은 선생님 언제나 감사하는 마음입니다. 멀리 있어도 항상 마음만은 함께하는 나의 정신적 지주 허니 지영이, 자주 못봐도 잊지 않고 반겨주는 오랜 친구들 지금까지도 앞으로도 고마워요. Thanks for being my dear friend Nastasja. 이제 한 단계 마무리 짓고 다음 단계로 넘어가려고 합니다. 더 많은 것을 배워, 사회에 조금이라도 이바지 할 수 있도록 앞으로도 열심히 살아가겠습니다.

Chapter 1 Introduction

The Nechako Basin has been a region of geophysical interest since the 1930s due to the hydrocarbon and mineral potential of this region. Since the 1980s, a number of geophysical studies have been conducted in the Nechako Basin, such as seismic surveys and exploration wells. A study by the Geological Survey of Canada suggested that the basin may contain as much as a trillion cubic meters of gas and a billion cubic meters of oil (Osadetz et al., 2007). However, there have been limitations on active source seismic methods for exploring the basin because of the extensive volcanic blanket near the surface within the basin. This Eocene and Neogene volcanic cover and Quaternary sediments near the surface which overlie the sequences with hydrocarbon and mineral potential are difficult to penetrate with active seismic sources at the surface. Therefore, geophysicists have considered techniques using passive seismic sources including receiver function and ambient noise methods to investigate the crustal structure in the Nechako Basin.

This study applies receiver function inversion that utilizes recordings of distant earthquakes (teleseisms) to map the sediments and crustal thickness within the Nechako Basin as well as the overall geometry of the basin. An array of seven Portable Observatories for Lithospheric Analysis and Research Investigating Seismicity (POLARIS) seismic stations was deployed in September 2006 to sample a wide area of the basin, and two additional stations were deployed in October and November 2007 due to unexpected local earthquake swarms (Cassidy et al., by personal communication,

2008). This study will complement independent active and passive source seismic studies by providing site-specific images and constraints on the S-wave velocity structure.

The first chapter briefly describes the study area providing the geological setting and tectonic history. The second chapter summerizes previous studies conducted in the 1980s and ongoing geophysical studies in the Nechako Basin area. In the third chapter, the methods used in this study are explained: the receiver function technique and the Neighbourhood Algorithm inversion. The dataset used in this study is described in the fourth chapter. Also, three important parameters for data processing are clarified in this chapter, such as layer thicknesses, the near-surface structure with a thin low velocity layer on the top, and a dipping interface, with simple examples. The fifth chapter contains the results of modeling data from the nine seismic stations in the basin. Crustal models are presented for each station. The observed receiver functions which are used as an input for the inversions are also shown in this chapter, with the synthetic receiver functions calculated from the crustal model described above. Chapter six presents conclusions and a summary of the crustal structure across the basin.

1.1 Study area

The study area of this project is the Nechako Basin in the central part of British Columbia, Canada (Figure 1.1). It is a Mesozoic fore-arc basin located in the Intermontane Belt of the southern Canadian Cordillera (Monger et al., 1982), which is a collage of oceanic and micro-continental terranes accreted to North America in the early

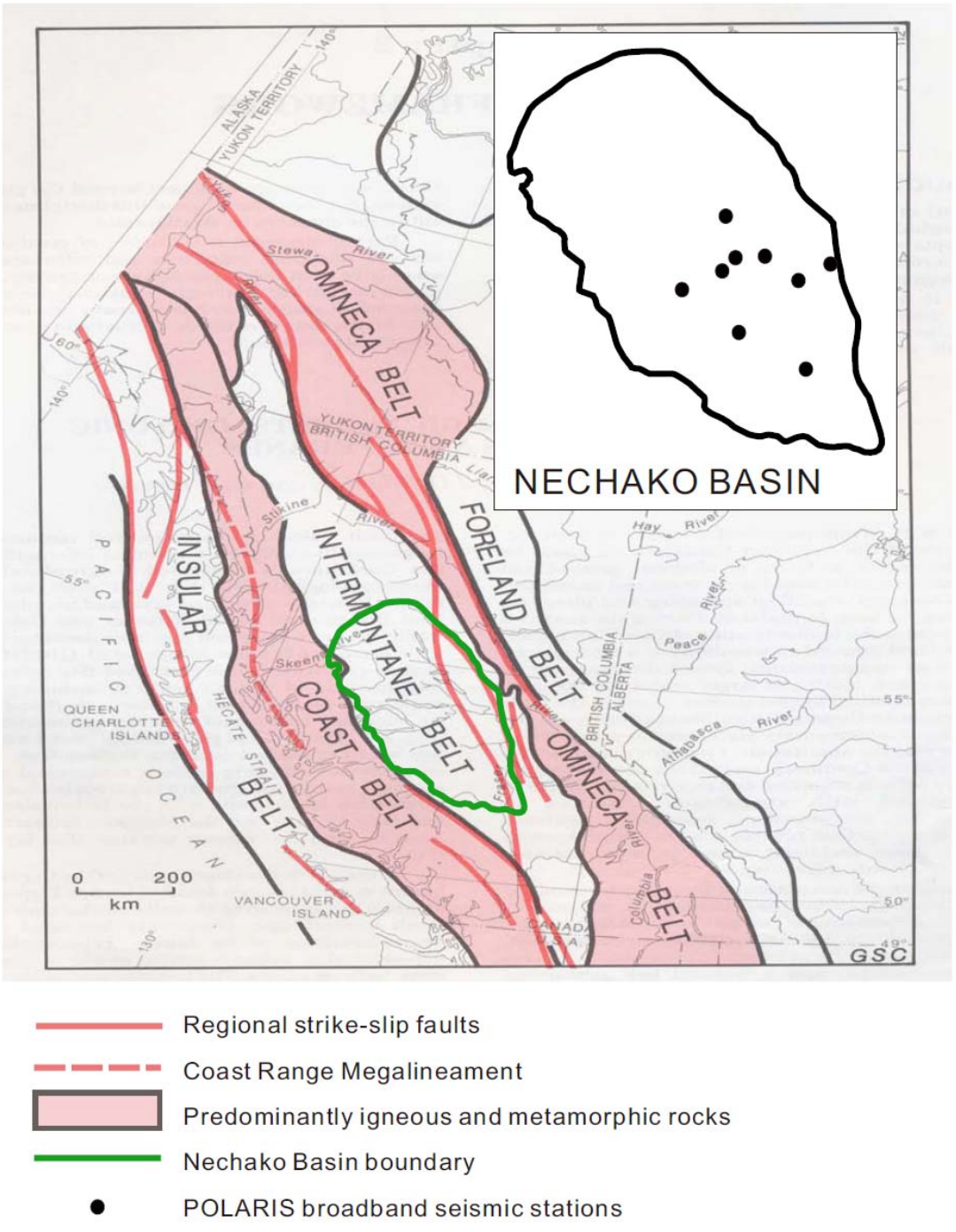

Figure 1.1 Location of the five morphogeological belts of the Canadian Cordillera, including the location of the Nechako basin within the Intermontane belt (original by Gabrielse et al., 1991a, modified by Idowu, 2009 and this thesis).

Mesozoic (Monger and Nokelberg, 1996; Monger et al., 1972). Two main accretion events created five morphogeological belts with a northwest-southeast trend; from west to east, they are the Insular, Coast, Intermontane, Omineca, and Foreland (Figure 1.1; Majorowicz and Osadets, 2008).

The western-most Insular Belt contains the Queen Charlotte Islands and Vancouver Island, and the Saint Elias Mountains. The Coast Belt is a mountainous belt which consists of igneous and metamorphic rocks within the Coast and Cascade Mountains. The Intermontane Belt, which contains the Nechako Basin, is underlain by various igneous and sedimentary rocks. It has generally subdued relief from modest Late Cretaceous and Cenozoic erosion surfaces. The Omineca and Foreland belts are made up of sedimentary rocks. Rock in the Omineca Belt have been intensely folded, metamorphosed and intruded by granitic rocks (Gabrielse et al., 1991b).

1.1.1 Intermontane Belt

The Intermontane Belt is a region of high plateaus, rolling uplands and deeply cut valleys that underlie much of south-central British Columbia, with generally low topography except for the Skeena Mountains in northwestern BC. The western boundary of the Intermontane Belt with the Coast Belt is the trace of the Pasayten, Fraser and Hungry Valley faults. The eastern boundary with the Omineca Belt is defined by changes in physiogeography and lithology, and by regional strike-slip faults, such as the Kutcho and Teslin faults. In contrast to the Omineca and the Coast Belts, it contains rocks which are rarely metamorphosed up to greenschist facies. Plutonic rocks are associated with

Late Triassic, Early Jurassic, Late Cretaceous, and Early Tertiary volcanism. Eastward directed structures of Cretaceous and Tertiary ages are in the western part of the belt, and westward directed structures of Middle and Late Jurassic ages are common in the eastern belt (Gabrielse et al., 1991a).

1.1.2 Nechako Basin

The Nechako Basin, the area of this study, is one of the four major basins within the Intermontane Belt. The other basins are the Bowser, Subtut, and Skeena. The Nechako Basin covers about 69,000 square kilometers. There are several strike-slip structures in the basin, which have produced an extensional basin filled with over 3 km of thick Mesozoic to Cenozoic clastic sequences. The clastic sequences represent overlapping successions deposited during and after accretion of volcano-sedimentary rocks. There are four main sequences in the Nechako basin: the Jurassic and Cretaceous, the Cenozoic, the Mesozoic, and the Eocene volcanic sequences. The first two sequences are composed of marine and fluvial clastics, whereas the last two are mostly volcanic rocks. The Eocene volcanic sequence with Miocene flood basalt covers most of the other sequences in the basin. All the rock sequences underwent mid-Cretaceous compression and Late Cretaceous to Paleocene transcurrent faulting (Yorath, 1991).

1.2 Local geology of the Nechako Basin

1.2.1 Tectonic history

The tectonic history of the Nechako Basin is obscure because the bedrock surface exposure is insufficient to collect the necessary information. Extensive Tertiary volcanic rocks and Quaternary sediments cover the Late Jurassic and Early Cretaceous sedimentary sequences (Figure 1.2).

In Triassic to Early-mid Jurassic ages, the volcanic and sedimentary Takla and Hazelton groups were deposited. Then in mid-Jurassic to Early Cretaceous ages, the Intermontane and Insular Belts were accreted to each other and to North America (Monger et al., 1982). During this accretion, the sediments were deposited in the basin. In the Tertiary, strike-slip faulting laterally displaced surrounding terranes, and a number of volcanic events covered most of the basin with basaltic flows. The folds and thrust faults in the basin are produced by Early Mesozoic accretionary prisms and subduction zones (Gabrielse, 1991b; Best, 2004).

1.2.2 Sedimentary units

There are five major sedimentary units within the Nechako Basin, consisting of the Cache Creek Group, and the Triassic to mid-Jurassic, mid-Jurassic to mid-Cretaceous, Late Cretaceous, and Tertiary units.

The Cache Creek Group (blue unit in Figure 1.3) is up to 2 km thick and consists of limestone, chert, volcanic layer, siltstone, and shale. The area is complicated by

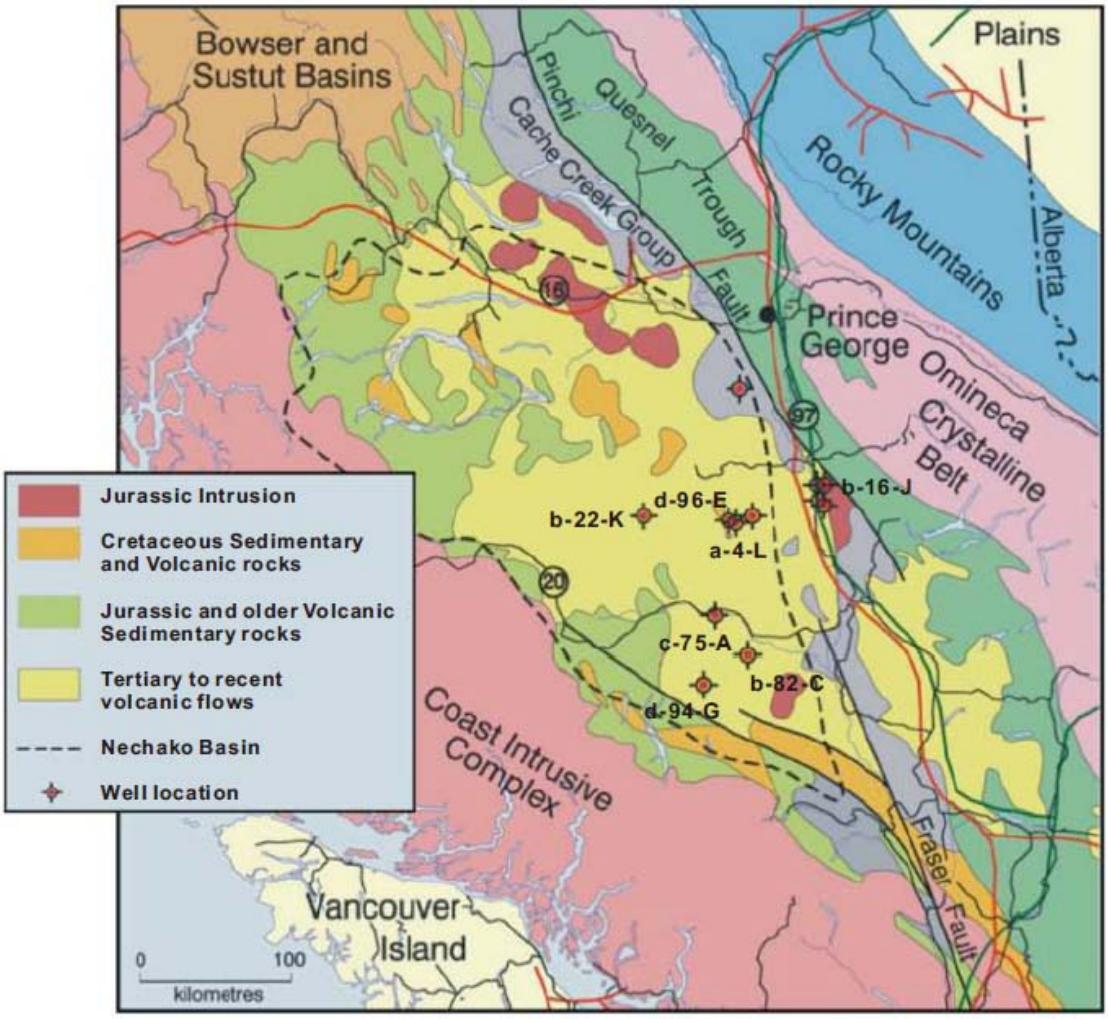

Figure 1.2 Regional geological map of the Nechako basin (Hayward and Calvert, 2008, modified in this thesis).

structural deformation and regional metamorphism. The Triassic to mid-Jurassic unit (green unit in Figure 1.3) consists of volcanic strata interbedded with lesser amounts of classic rocks. It reaches up to 3 km thick, but it is not continuous across the basin. The mid-Jurassic to mid-Cretaceous unit (red unit in Figure 1.3) is about 3 km thick and contains mainly course-grained clastic rocks with minor volcanic rocks. Sorting and maturity is poor in the thick non-marine section, but is better defined in the marine strata.

The Late Cretaceous unit (purple in Figure 1.3) is about 1.5 km of conglomerates in the southeast part of the basin. It was laid uncomformably on the mid-Jurassic to Cretaceous unit. In the northwest, marginal marine sandstones coarsen upward, locally to conglomerate. The most recent Tertiary unit (yellow in Figure 1.3) is dominated by volcanic rocks, but it is not consistent across the basin (Hayes et al., 2002).

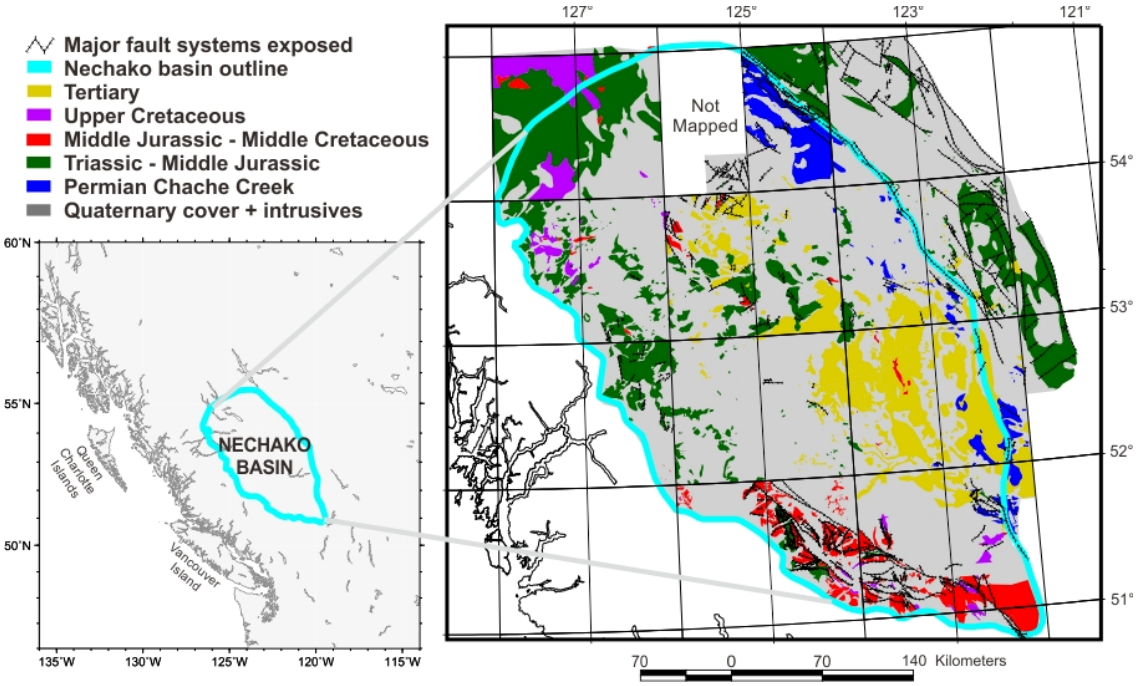

Figure 1.3 The location of the Nechako Basin, BC (left). Simplified geological map of the Nechako Basin (right, Hayes et al., 2002).

Chapter 2 Other studies in the Nechako Basin

A number of geophysical studies have been undertaken to map the structure of the Nechako Basin over the past 3-4 decades, and several are currently underway. Wickens (1971, 1977) started to examine this area using regional surface wave studies, and Berry and Forsyth carried out a seismic refraction study of the Canadian Cordillera (Berry and Forsyth, 1975). They suggested that there is a low-velocity zone in the upper mantle beneath the basin. After these studies, several other methods were utilized in the 1980s. 2-D seismic survey lines were conducted by Canadian Hunter Exploration Limited, and exploration wells were drilled by Canadian Hunter, Esso, Honolulu Oil Corporation Limited, and Hudson's Bay Oil and Gas Company Limited. However, these seismic data were of limited use because the sediments of interest lie beneath the highly-reflective volcanic cover. Currently, the 1980s industry seismic lines are being reprocessed and analysed with more modern methods (Hayward and Calvert, 2008). In recent years, ambient noise, magnetotellurics (MT), gravity and other geophysical methods have also been utilized for mapping the structure of the Nechako basin.

2.1 Active seismic studies

Recent active studies carried out in northern BC, partly Intermontane Belt including the Nechako area, including seismic refraction and wide angle reflection (Welford et al., 2001) to construct a velocity model of the crust and upper mantle. The

study area of this project crossed the Intermontane belt, to the northwest of the Nechako basin. Results from this study interpret the crustal structure as 5 layers, including the upper mantle. In addition, the S-wave velocities for the layers are estimated from the P-wave velocity model using a Vp/Vs ratio of 1.69 (Fernandez-Viejo et al., 2005). The thin first layer (<1 km) beneath the surface consists of Quaternary sediments, and another thin layer (<1 km) is present underneath it, which contains Phanerozoic sedimentary rocks with a wide range of S-wave velocities (Vs): from 1.43 km/s to 3.78 km/s. The third layer, the upper crust, is about 9 km thick with Vs of 2.80-3.43 km/s, and the lower crustal layer is about 23 km thick with Vs of 3.33-4.19 km/s. The Moho is present at about 33 km depth in general in the Nechako basin; the Vs of the upper mantle layer starts at 4.32 km/s.

Another active seismic method is the first-arrival tomographic inversion by Hayward and Calvert (2008). This method uses the travel time of the first arrival (direct wave or head wave) during a seismic reflection profile in order to determine the P-wave velocity in the near surface, to a depth of a few hundred meters. The study area is divided into four blocks in the southern part of the basin (Figure 2.1). Triangles in this figure are the seismic stations in the POLARIS array used in my study: FLLB is in block A, THMB and UBRB are in block C, and FPLB and RAMB are in block D. The results from this first-arrival tomographic inversion give details of the ray density and P-wave velocity near the surface (Figure 2.2). This project is still ongoing (Hayward and Calvert, by personal communication, 2010).

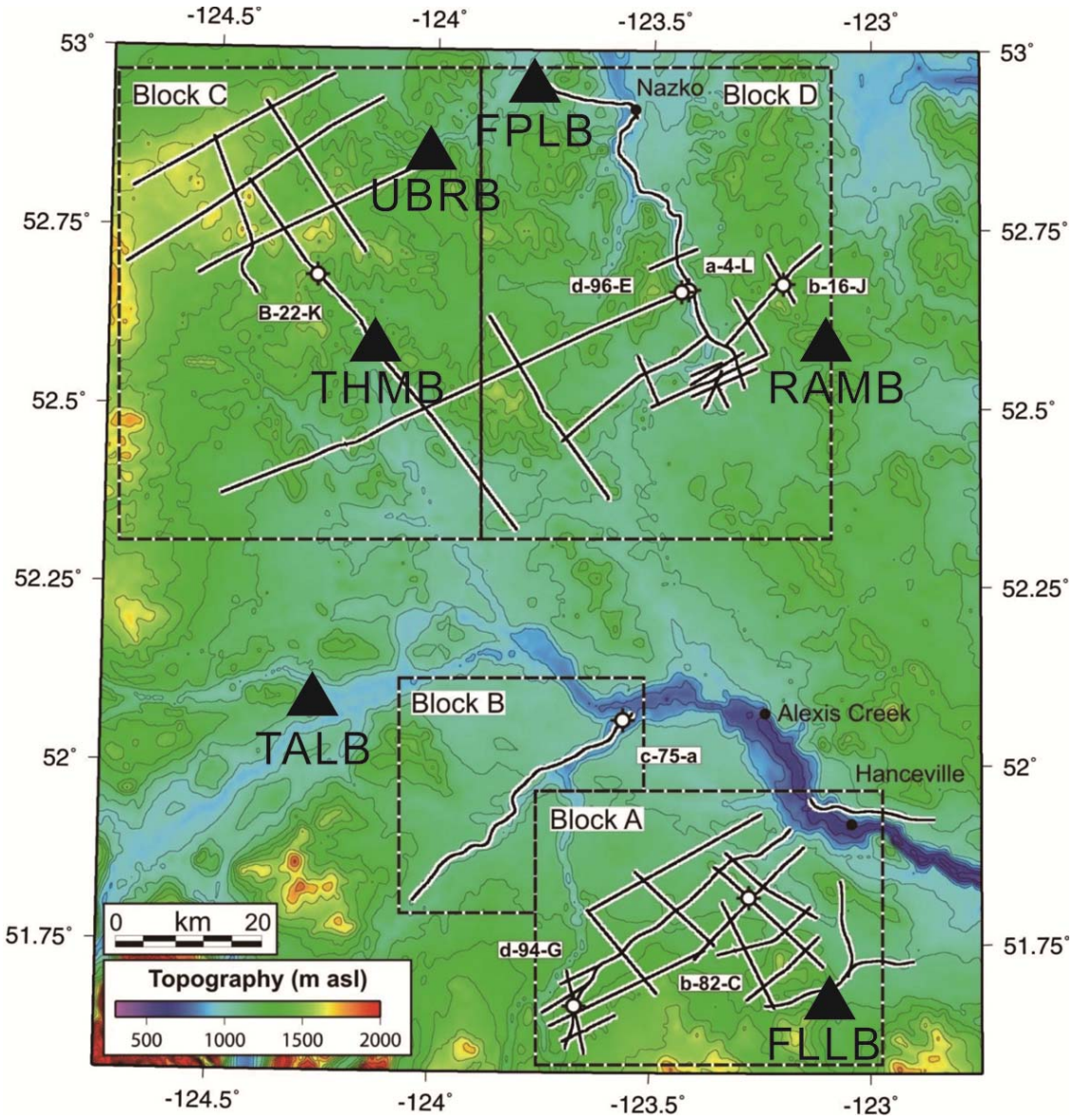

Figure 2.1 Location of the 1980s Canadian Hunter seismic reflection lines (white bordered black lines) and topography of the study area, southeastern Nechako basin (original by Hayward and Calvert, by personal communication, 2010, and modified in this paper). Contour interval 100 m. Large dashed boxes show the original study blocks (A, B, C, and D). Black circles show well locations, and triangles show the location of the seismic stations in the POLARIS array.

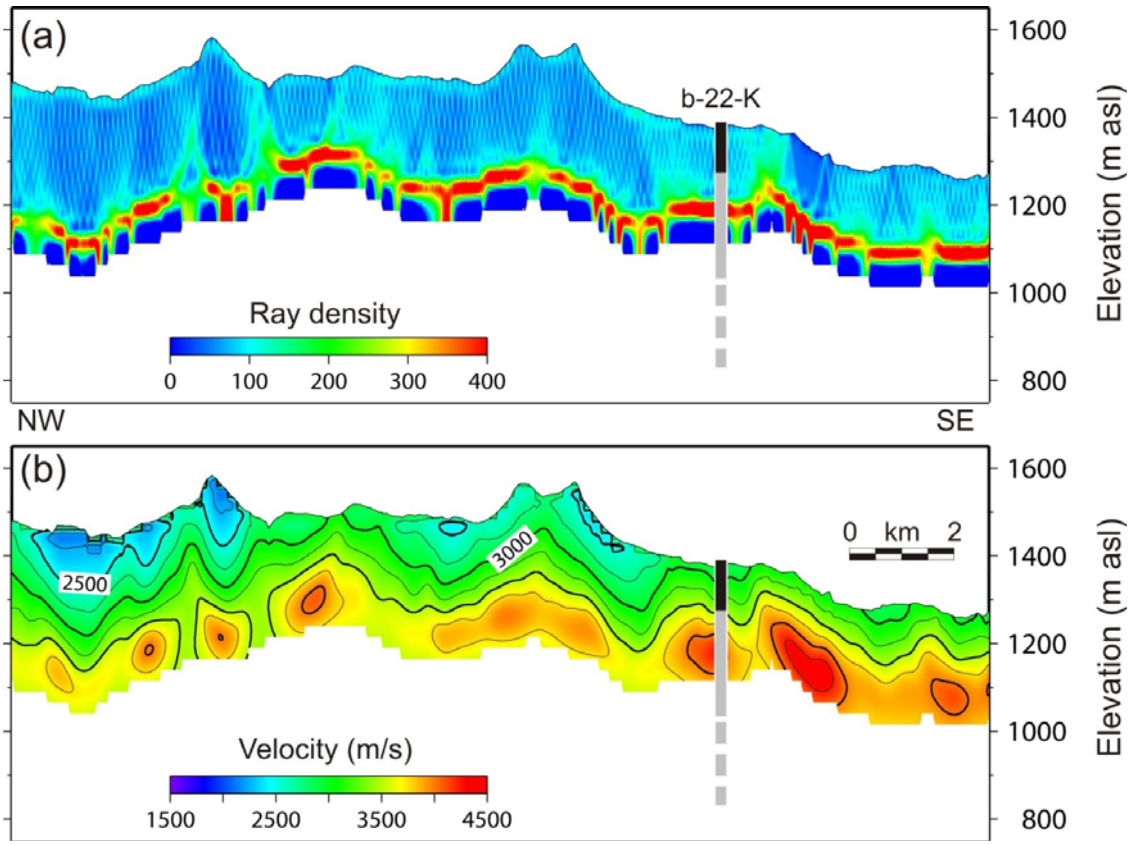

Figure 2.2 First-arrival tomographic inversion model for a section of Canadian Hunter line CH161-03, near well b-22-K and seismic station THMB. (a) Ray density and (b) P-wave velocity. Heavy black line shows the thickness of Neogene Chilcotin Group volcanic in well b-22-K (Hayward and Calvert, by personal communication, 2010).

2.2 Passive seismic studies

A typical geophysical method which is complementary to receiver function inversion is ambient noise inversion. It illustrates the average velocity structure of the crust between two seismic stations whereas the receiver function method provides information on the structure beneath each seismic station. The ambient noise method utilizes the dispersion curves for the Rayleigh waves which dominate the ambient noise. The ambient noise method used in the Nechako basin constructed 2-D group velocity

maps between 0.03 and 0.55 Hz and 1-D S-wave velocity models (Idowu, 2009). The average 1-D model within the basin was based on 6 layers: 1.8-km-thick near surface sediments, 0.6-km-thick volcanic rocks, 2.0-km-thick sedimentary basin, 9.1-km-thick Precambrian basement (upper crust), 17.0-km-thick lower crust, and the upper mantle. The model for outside the basin was similar to the model above, except for the volcanic and sedimentary layers which were not present outside of the basin. The average crustal thickness of the Nechako basin is about 30-32 km, and the thickness of the top surface sediments and volcanic cover beneath the sediments are about 0.3-1 km and 0.6-1.2 km respectively (Figure 2.3).

Passive seismic transmission tomography is also being applied in the Nechako basin (Best and Lankings, 2007). This method utilizes the acoustic energy generated by micro-earthquakes in the upper few kilometers of the crust and produces 3-D multi-component velocity volumes. Since the energy crosses the highly-reflective volcanic layer only once, the signal is less attenuated and more coherent than seismic methods based on surface sources. Seismic transmission tomography studies that were started in 2007 are still in progress.

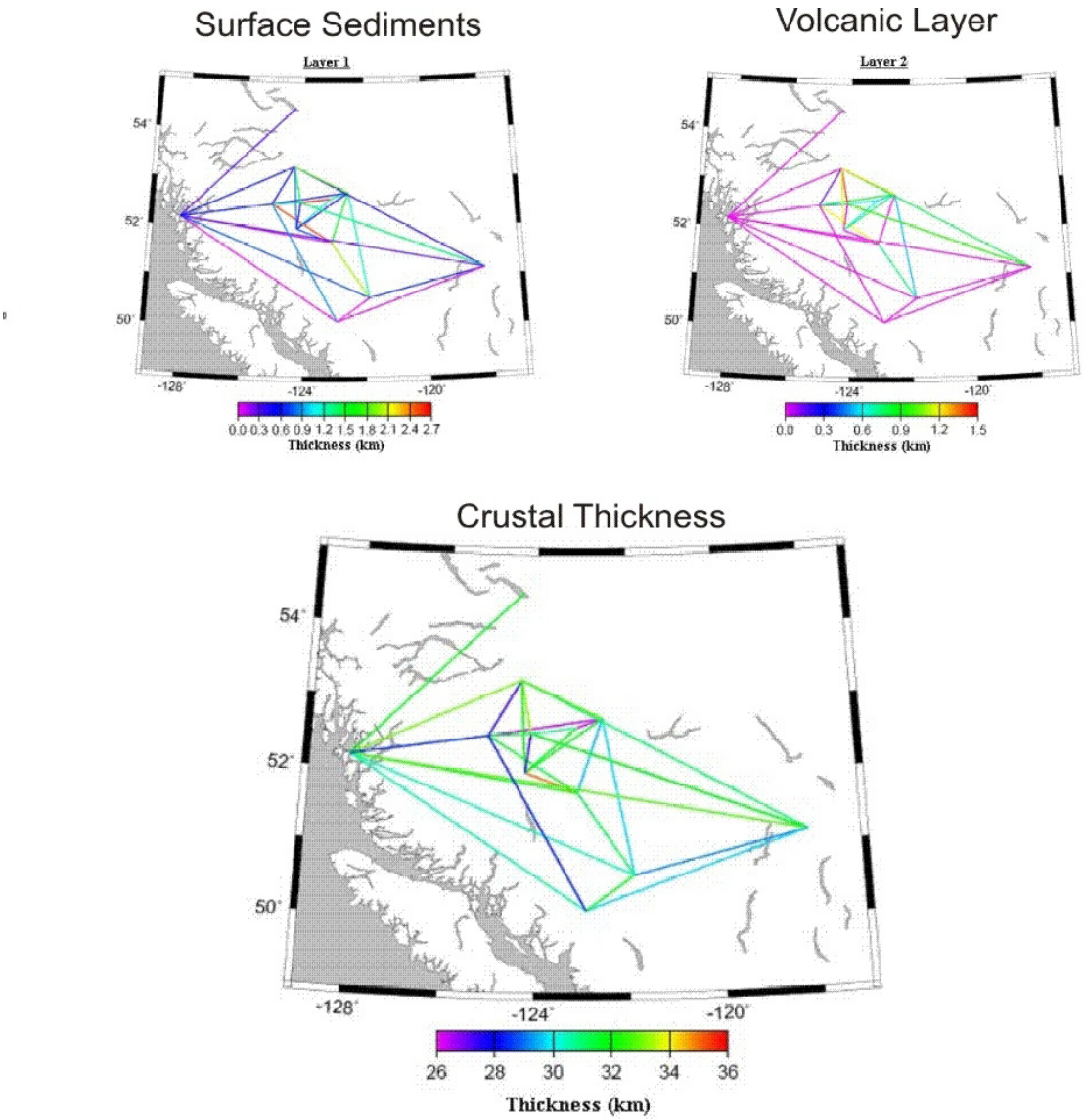

Figure 2.3 Average thickness of sediments, volcanic, and the total crust in the Nechako basin based on ambient noise data (Idowu, 2009).

2.3 Wells in the Nechako basin

Exploration wells were drilled within the Nechako basin by Canadian Hunter Exploration Limited, Esso, Honolulu Oil Corporation Limited and Hudson's Bay Oil and

Gas Company Limited in the 1980s. The stratigraphy from seven of them (detailed by Ferri and Riddell, 2006) are reviewed in this study. In this section, the well descriptions from the stratigraphic column (Ferri and Riddell, 2006) will be covered, but sonic logs with velocity will be described in Chapter V (results section for each station). The locations of all wells are shown in Figure 2.1, and the stratigraphic columns from Ferri and Riddell (2006) are presented in Figure 2.4.

2.3.1 Canadian Hunter et al. Nazko d-96-E

Well d-96-E is located between THMB and RAMB (40 km to the east of THMB and 20 km to the west of RAMB). The well description of d-96-E indicates that this location contains a 2.95 km-thick Cretaceous sedimentary rock layer above a dominantly volcanic sequence. This volcanic layer starts at 2.95 km depth, and is composed of minor varicolored chert, intrusive rocks, and shale which probably belongs to the Cache Creek Group. Greenish shale and siltstone (Jackass Mountain Group) are shown at depths between 2.95 km and 2.49 km, and conglomerate, sandstone, siltstone and shale start from 2.49 km to 0.65 km. These are equivalent in age to the Taylor Creek Group. Sedimentary features such as mud drapes and ripple-cross laminations, which may come from a marine depositional environment, are observed in the layers near the surface.

Well d-96-E

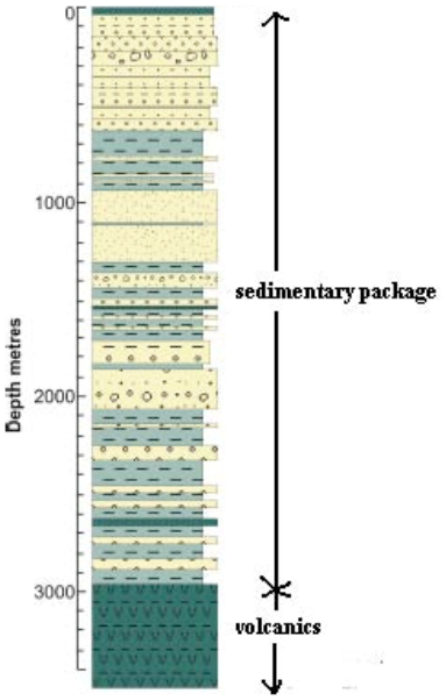

Well a-4-L

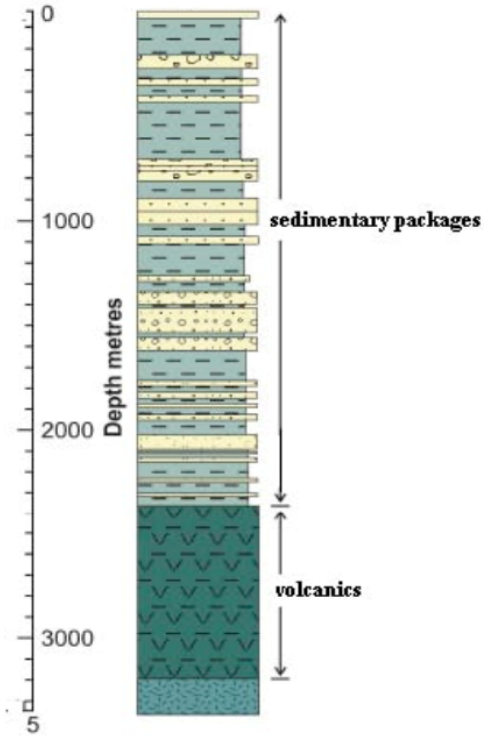

Well b-22-K

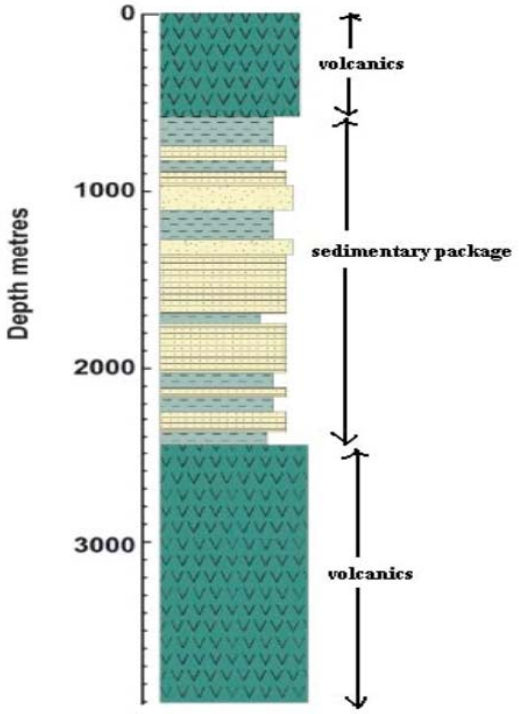

Well b-16-J

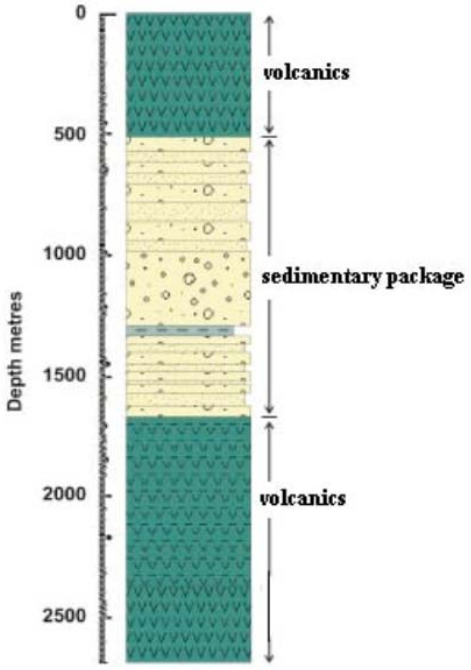

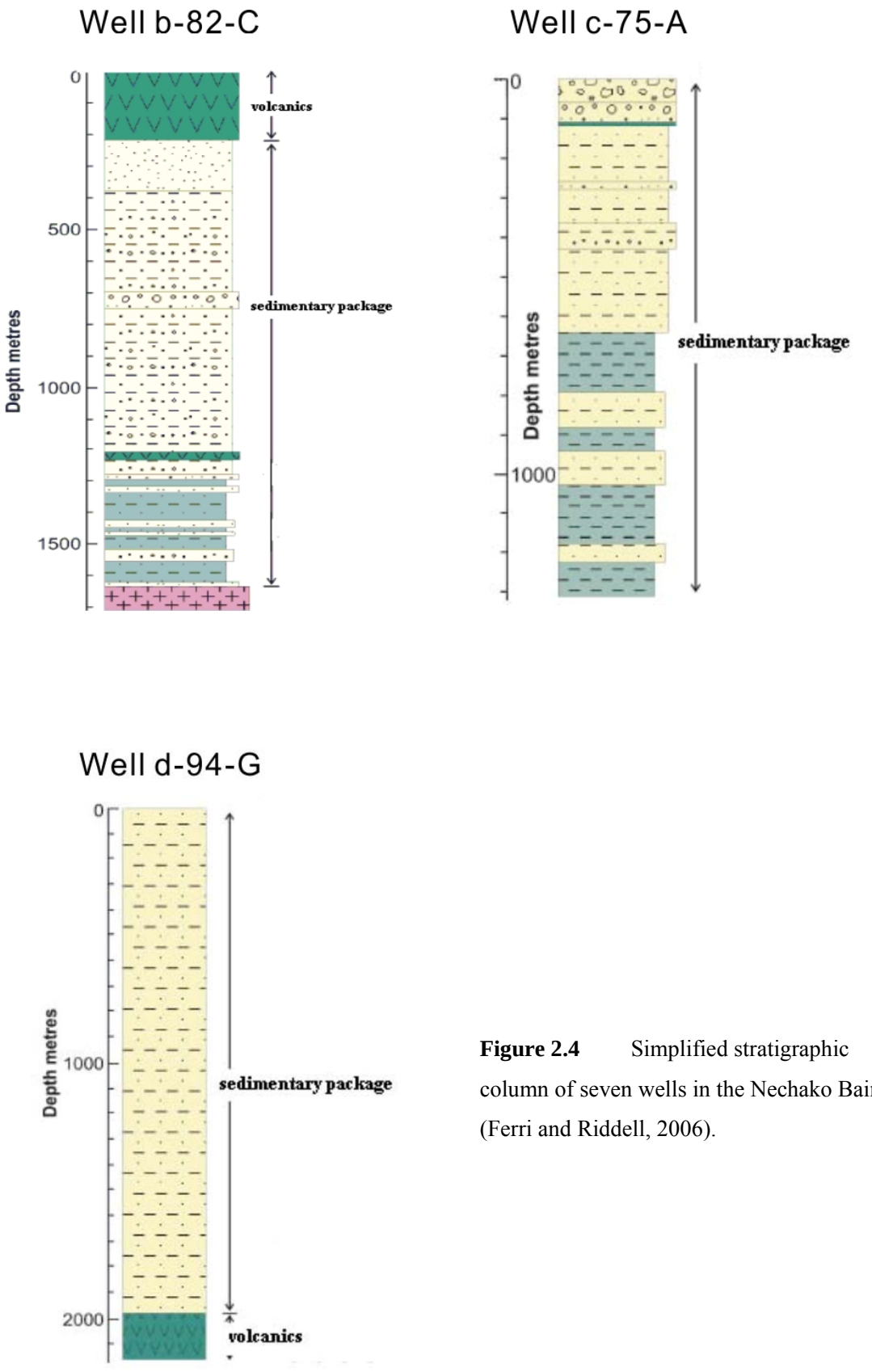

Figure 2.4 Simplified stratigraphic column of seven wells in the Nechako Bain (Ferri and Riddell, 2006).

2.3.2 Honolulu Nazko a-4-L

Well a-4-L is located only about 2 km to the east of the well d-96-E, and hence there are many similarities to well d-96-E. A layer of Cretaceous sediments lies above the volcanic layer, although several coarse clastic sequences have less shale to the east. The lowest part of the well contains diorite (Cache Creek Group), and basalt, tuff and shale overlay it to 2.38 km depth. As at d-96-E, the greenish sedimentary rocks (Jackass Mountain Group or Paradise formation) are at depths of approximately 2.1 km. However, the conglomerate and sandstone sequence (which is present at the top of d-96-E) is absent here. A thick conglomerate and sandstone layer (Taylor Creek Group) occurs from 1.62 to 1.36 km depth for a-4-L.

2.3.3 Canadian Hunter et al. Chilcotin b-22-K

Well b-22-K is only about 5 km away from THMB, and 50 km from d-96-E to the east. Palynology data from Hunt (1992) indicate that this stratigraphy is entirely younger than the sequence within d-96-E. At the bottom of the well, maroon to greenish hornblende-plagioclase volcanic rocks overlie conglomerates of the Silverquick formation. Succeeding these, volcanic and reworked volcanics are present at depths between 2.7 and 1.55 km, above the sedimentary rocks (greenish claystone, shale) with minor volcanics beginning from 1.2 km depth. From 1.55 km to the surface, shale and mafic volcanic rocks of Eocene, Oligocene, and Miocene are present. The Eocene and Oligocene layer is associated with the Kamloops Group and Australian Creek Formation, while the Miocene layer is Chilcotin Group basalt.

2.3.4 Canadian Hunter Esso Nazko b-16-J

Well b-16-J is close to RAMB (10 km to the northwest from RAMB), as are wells d-96-E and a-4-L. It is about 15 km from d-96-E to the east. However, b-16-J has a different stratigraphic column from the others, with volcanic rocks dominating. A Tertiary sedimentary sequence is present in the central part, between the volcanics. The bottom sequence of the well is basalt (Cache Creek Group) which is overlain by 0.7 km-thick tuff and minor mafic lava. The tuffs are light in color and less cherty, which is typical of local Tertiary rocks in this region, but not of the Cache Creek Group. The sedimentary rocks in the middle (1.68 km to 0.5 km depth) are composed of maroon, grey and green polymict conglomerate, sandstone, siltstone and lesser shale form. The top 0.5 km thick volcanic sequence is Endako Group, continuing to the surface.

2.3.5 Canadian Hunter et al. Redstone b-82-C

Well b-82-C is located about 20 km from FLLB. It intersected a granite to granodiorite layer at a depth of 1.63 km. The upper 20 m of the igneous section has been interpreted to consist of reworked igneous material, suggesting an unconformity between Cretaceous sediments and the intrusive body (Cosgrove, 1981). Dark grey shale and interbedded ‘salt and pepper’ chert sandstone and conglomerate are present to a depth of 1.28 km. The general characters of these are similar to the Taylor Creek Group, which is indicated as middle Cretaceous in age. The section between 1.28 km and 0.22 km depth contains poorly consolidated maroon to green or grey sandstone, polymict conglomerate,

siltstone, and shale. An unconformity clearly exists at the bottom of this section (1.28 km depth). The top 0.22 km of well b-82-C consists of a mafic flow and tuff (Endako Group).

2.3.6 Hudson's Bay Redstone c-75-A

Well c-75-A is located between FLLB and TALB (50 km to the northwest of FLLB and 40 km to the east of TALB). It is only about 1.3 km deep, and located northwest of the Gap Narrows bridge across the Chilko River, where there is a small window of exposed sedimentary rock. Chert-pebble conglomerate, sandstone, and minor siltstone are present in this well, which suggests a fluvial environment that may be related to the Silverquick formation. The bottom section is dominated by dark grey to grey shale, dark red siltstone, and lesser sandstone. The top 90 m suggests the Taylor Creek Group.

2.3.7 Canadian Hunter et al. Redstone d-94-G

Well d-94-G is also located between FLLB and TALB (35 km to the west from FLLB and 55 km to the southeast from TALB), and about 40 km away from well c-75-A to the south. The volcanics at the bottom of the well contain varicolored feldspar and hornblende-bearing rocks and are of an intermediate to felsic nature (Cosgrove, 1986). A 1.98 km thick sedimentary unit (interbedded sandstone, shale, and siltstone) is present over the volcanic sequence at the bottom of the well. The sequence above 0.68 km was formed in the middle Cretaceous, and becomes older as the depth increases.

2.4 Magnetotelluric measurements

Magnetotelluric (MT) methods provide information on the electrical resistitivity of the subsurface by measuring natural time-varying electromagnetic fields at the Earth's surface. The electrical currents in the Earth are induced by natural variations in the Earth's magnetic field by high-frequency thunderstorms and low-frequency solar winds. Estimating an earth resistivity model by inverting MT data provides an approach to distinguish crustal layers: sedimentary rocks typically have resistivities between 1 and 1000 ohm-m, whereas volcanic rocks have average resistivities larger than 1000 ohm-m. Therefore it is useful to determine each lithological unit in the crust using MT (Spratt and Craven, 2008). Seven MT lines were collected in the Nechako basin, and some of them are near the seismic stations in the POLARIS array (Figure 2.5): UBRB, FPLB, CLSB, and FLLB. 2-D profiles from MT studies show the resistivity distribution in the crust, down to about 15 km depth.

In the model of Profile A, there is a ~0.5 km thin high-resistivity layer (blue color in Figure 2.6) near the surface, which is the evidence of the Chilcotin basalts. In addition, there is a low-resistivity layer underneath the basalt cover; which may be Cretaceous/Eocene sediments (Spratt and Craven, 2008). Precambrian Hazelton basement has high resistivity and is shown in blue.

The thin top volcanic layer is absent in Profile B (Figure 2.7), and only the low-resistivity layer of Cretaceous sediments is present near the surface, down to about 2.5-km depth. These MT results correspond to the well log in this Profile (a-4-L).

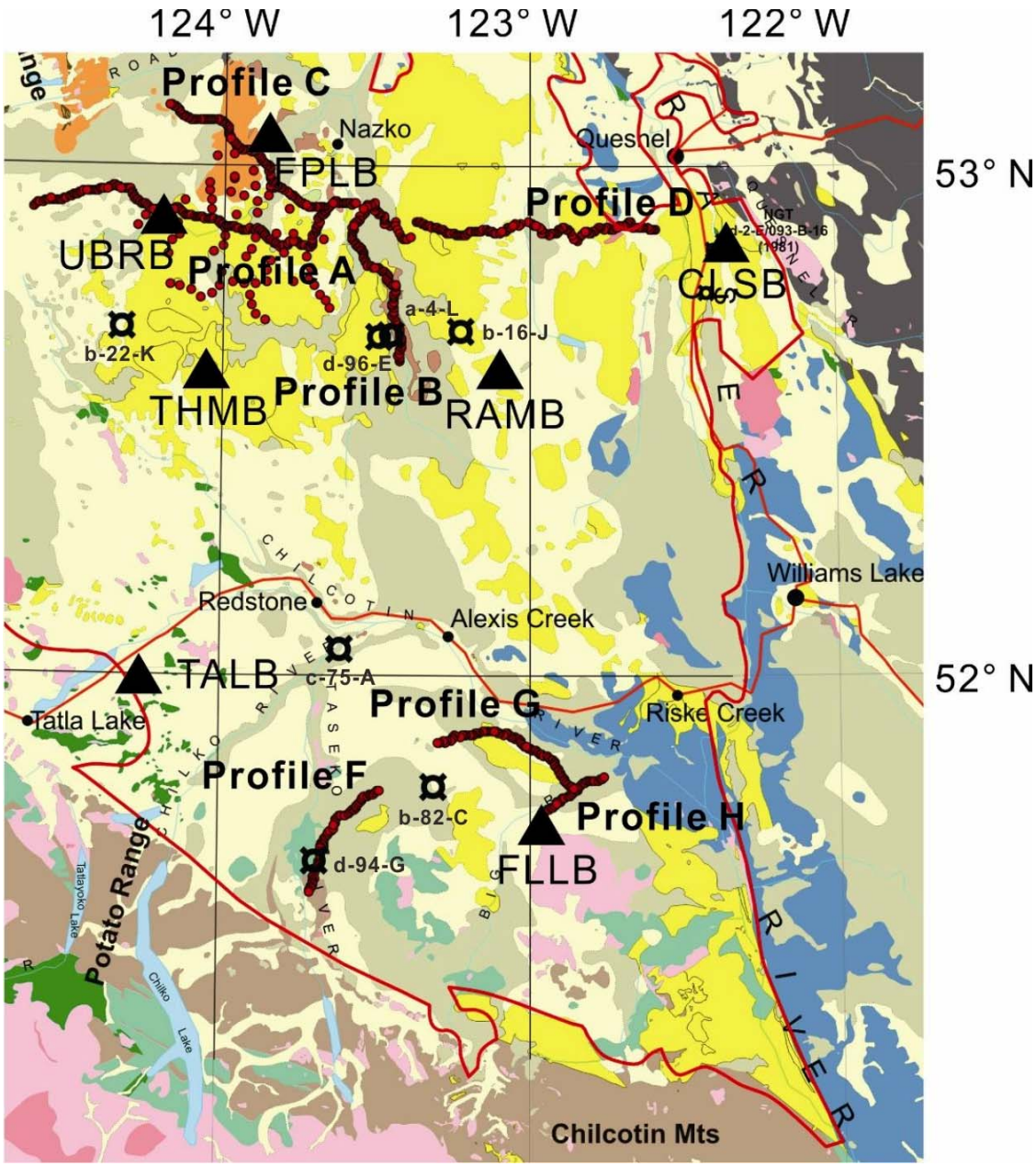

Figure 2.5 Location of the MT profiles (A,B,C,D,F,G,H) (original by Spratt and Craven, by personal communication, 2009 and modified in this thesis). Black circles show well locations, and black filled-triangles show the location of the seismic stations.

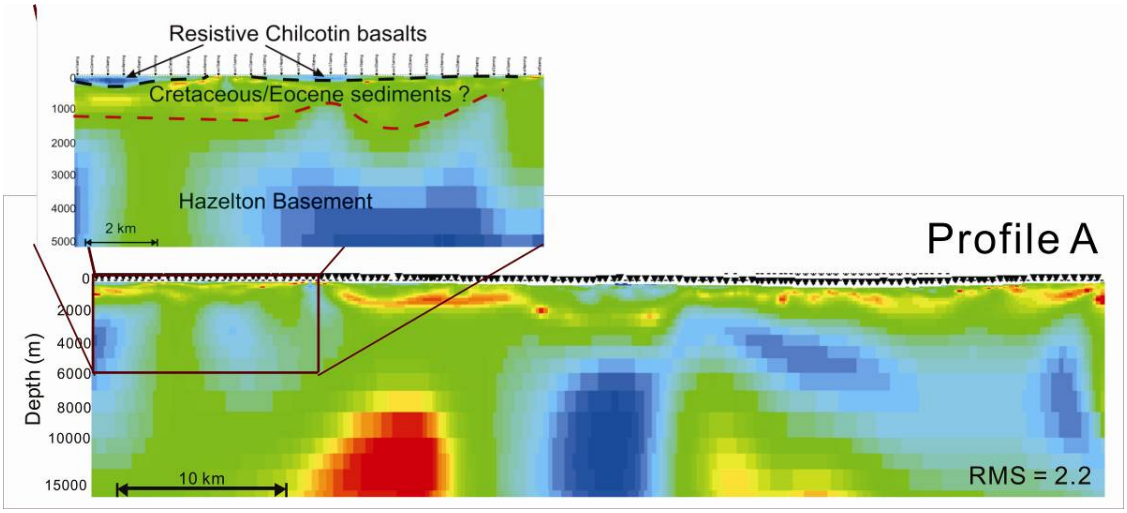

Figure 2.6 Cross-section illustrating the 2-D resistivity model generated along Profile A (Figure 2.5). Red represents low resistivity and blue represent high resistivity. The top high-resistivity layer indicates the volcanic layer on the surface, corresponding to the Chilcotin basalts (Spratt and Craven, by personal communication, 2009). Colour scale of resistivity is shown below.

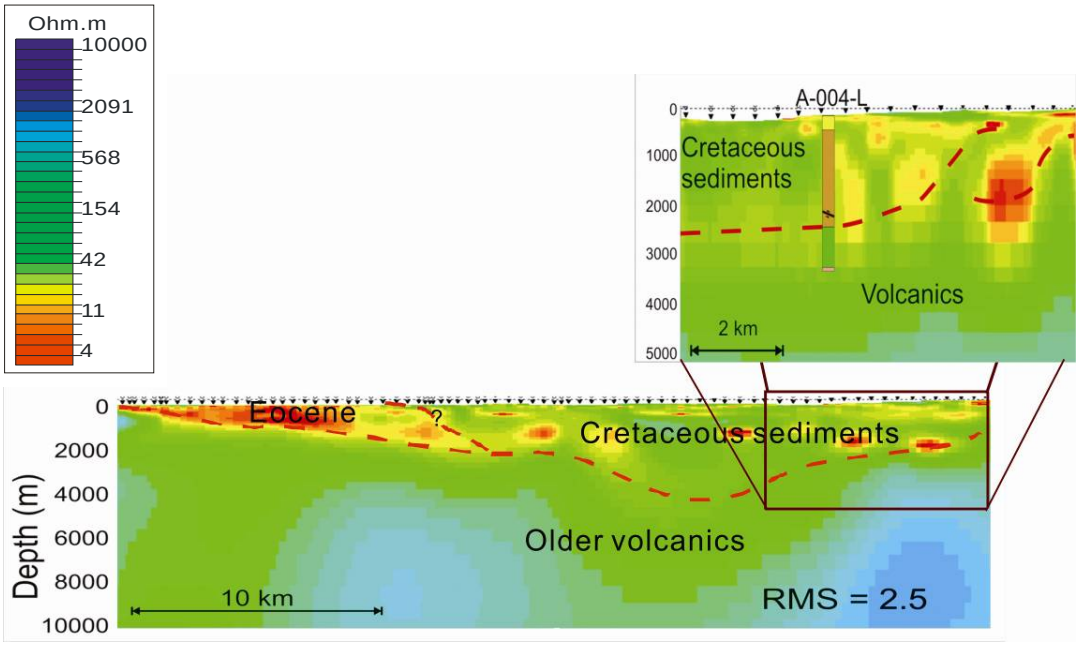

Figure 2.7 Cross-section illustrating the 2-D resistivity model generated along Profile B (Figure 2.5). Red represents low resistivity and blue represent high resistivity. Thick Cretaceous sediments are present near the surface down to ~2.5 km depth, and agree with the borehole data (a-4-L, Spratt and Craven, by personal communication, 2009). Colour scale of resistivity is shown on left side.

2.5 Gravity

The first gravity survey in the Nechako basin was performed in 1980 by Canadian Hunter Exploration Ltd, and the map from this survey was digitalized by Ferri et al. in 2004 (Figure 2.8). The high-gravity zones generally indicate volcanic and/or high-density intrusive rock and the low-gravity zones indicate thick sedimentary rocks with average density. However, the low-gravity zone may be consistent with low-density intrusions, such as granite, within a denser dominant volcanic layer (Ferri and Riddell, 2006).

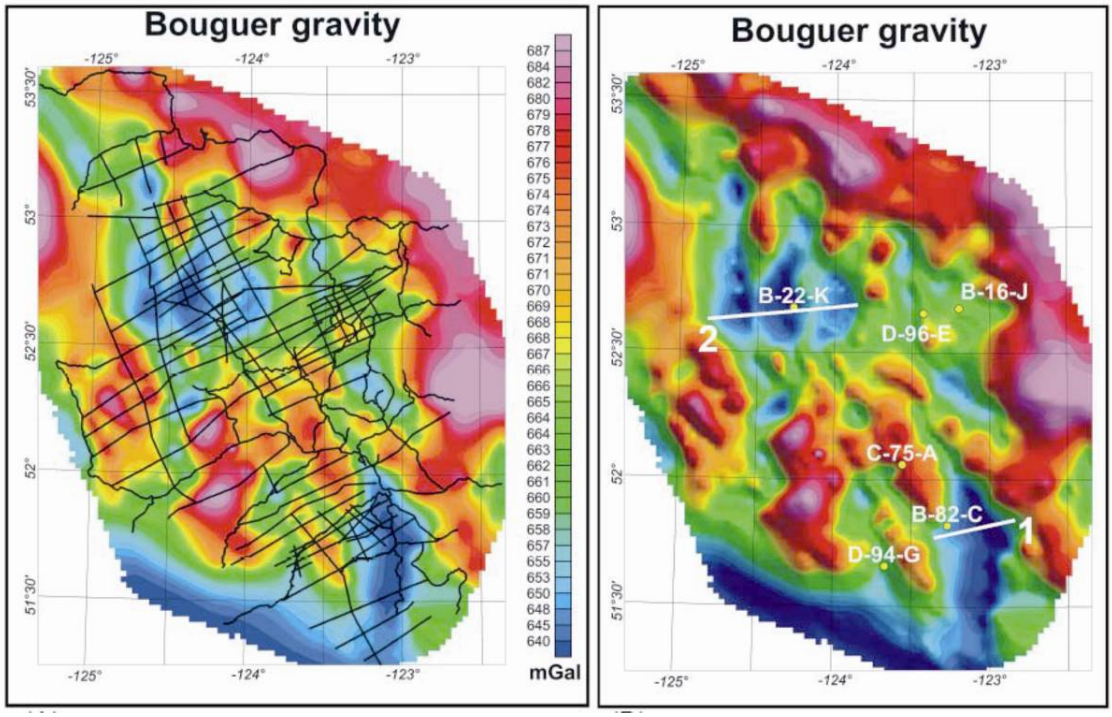

Figure 2.8 Bouguer gravity map of the Nechako basin (Ferri and Riddell, 2006). Red shows high gravity area (volcanic and high density intrusions), blue shows low gravity area (sedimentary rocks). (Left) seismic lines are shown in black lines. (Right) wells are shown in yellow dots, and gravity survey sites are shown as white lines.

Chapter 3 Methods

3.1 Receiver Function

This study uses receiver function analysis as the main method of investigation to construct a model for the S-wave velocity structure. This method uses teleseismic P-waves arriving at a receiver. When the waves arrive, they contain valuable information about the structure near the source, mantle path effects and the structure of the crust directly beneath the receiver. The receiver function is calculated by deconvolving the vertical component from the horizontal component of the P-waveforms.

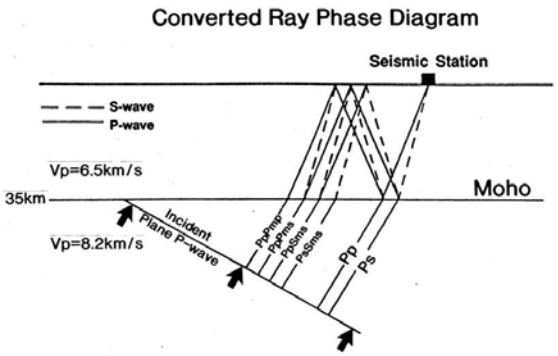

Figure 3.1 Example of ray path of P- and S-waves. The receiver function from this set of ray paths is represented in Figure 3.2 (Cassidy, 1992).

Figure 3.1 illustrates the ray paths of P- and S-waves within a horizontal layer which has a discontinuity in velocity at depth h: the solid line represents the P-wave path and the dashed line represents the S-wave path. Each conversion of the ray due to the

discontinuity generates the spike of the receiver function (Figure 3.2) by the deconvolution.

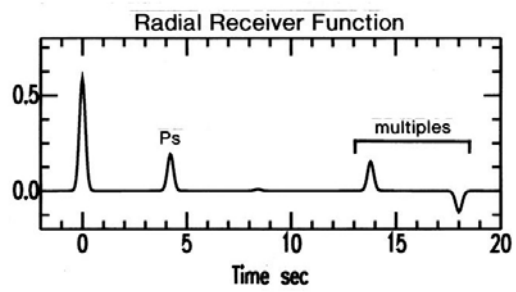

Figure 3.2 Example of receiver function generated by horizontal layers with sharp arrivals (Cassidy, 1992).

The amplitudes of the arrivals in a receiver function depend on the incidence angle of the impinging P-wave and the magnitude of the velocity contrasts generating the conversions (Ps) and multiples (PsPhs, PpShs, PpPhs). The arrival times of the converted phase and multiples depend on the depth of the velocity contrast, the P- and S-wave velocity between the contrast and the surface, and the P-wave incidence angle or ray parameter (Cassidy, 1992).

3.1.1 Receiver function analysis

The typical processing flow of receiver function analysis has five main steps. The first step is to organize the observations and study variations in the response with respect to the back azimuth, distance, and depth of the source. The second step uses three-component observations to equalize near-source effects and isolate the receiver effects

from the observed waveforms. Isolating the local response requires deconvolution of the vertical component of ground motion from the horizontal components. The third and fourth steps are forward modeling and inversion through computation of receiver functions for various earth models. Finally, the best solution is chosen taking into account information from previous studies and geologic constraints.

3.1.2 Receiver function estimation and Gaussian filters

In an ideal case (Langston, 1979; Owens, 1984; Ammon, 1991), the radial receiver function is given by

$$E_R(\omega) = D_R(\omega) / D_Z(\omega)$$

where $D_R(\omega)$ and $D_Z(\omega)$ are the frequency-domain representation of the recorded radial and vertical ground motions. However, the water-level method (Clayton and Wiggins, 1976) is usually applied to stabilize the frequency-domain spectral division as required because of data noise and the band-limited nature of signals. Therefore, the deconvolution is given by

$$\tilde{E}_R(\omega) = D_R(\omega)\, A(\omega) / D_Z(\omega)$$

where $\tilde{E}_R(\omega)$ is an estimate of the true receiver function $E_R(\omega)$. $A(\omega)$ is the averaging or blurring function associated with the deconvolution and is given by

$$A(\omega) = D_Z(\omega)\, D^*_Z(\omega)\, G(\omega) / \varphi(\omega)$$

where

$$G(\omega) = \exp(-\omega^2 / 4a^2)$$

and

$$\varphi(\omega) = \max \{ D_Z(\omega)\, D^*_Z(\omega), c \cdot \max [D_Z(\omega)\, D^*_Z(\omega)] \}.$$

In this equation, $D^*_Z(\omega)$ is the complex conjugate of $D_Z(\omega)$ and c is the water-level parameter expressed as a fraction of the maximum vertical component power spectrum, and *a* controls the width of the frequency-domain Gaussian filter used to remove high-frequency noise. Lower *a* values are used to examine the low frequency components of the data whereas higher *a* values are used for high frequency components (Cassidy, 1992). In this study, all receiver functions were calculated with *a* values being 2 and 5. An *a* value of 2 removes the frequencies greater than 1 Hz, and an *a* value of 5 removes frequencies greater than 2.4 Hz. More *a* values with corresponding cut-off frequencies are listed in Table 3.1.

a value	Frequency (Hz) at which G(f) = 0.1
10	4.8
5	2.4
2.5	1.2
2	1.0
1.25	0.6
1	0.5
0.625	0.3
0.5	0.24
0.4	0.2
0.2	0.1

Table 3.1 *a* value corresponding to frequency at with G(f) = 0.1.

Receiver functions calculated with a larger *a* value include higher frequency components of the data, which allows for mapping more detailed structures, whereas small *a* values pass only lower frequency components leading to more simple and general features. As an example, in Figure 3.3, I compare an observed low frequency receiver

function (a = 2) in black with a higher frequency receiver function (a = 5) in red. For a = 2, the Moho arrival occurs at around 4 s, but other features are not easily visible because the low-pass Gaussian filter makes the synthetics smoother and simpler. However, as shown in the same figure, the synthetic with higher frequency content represents the details more, especially for the near surface structures.

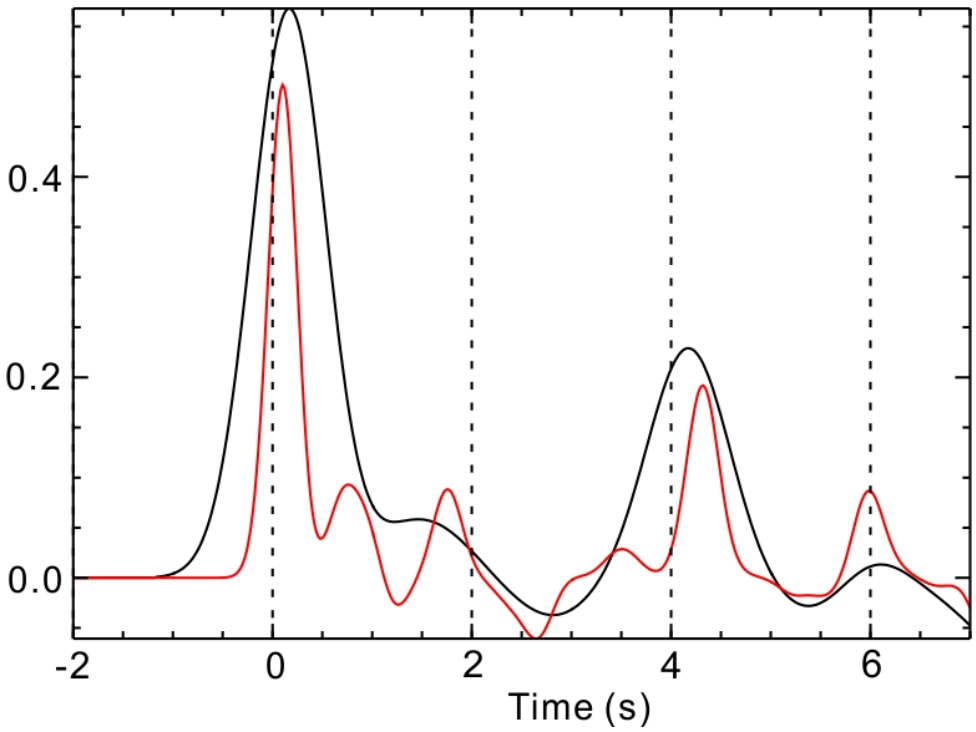

Figure 3.3 Example of effect of the Gaussian filter. Both observed receiver functions are calculated with the same original teleseismic waveform, but with different a value for the Gaussian filter; 2 for black, and 5 for the red line.

3.1.3 Iterative deconvolution

Iterative deconvolution is developed to minimize of the difference between the observed horizontal seismogram and a synthetic receiver function generated by the

convolution of the iteratively updated spike train with the vertical component seismogram (Ammon, 1991). First, the cross-correlation of the vertical component and the radial component is used to estimate the lag of the first largest peak in the receiver function. Then, the convolution of the current estimate of the receiver function with the vertical component is subtracted from the radial component seismogram. These steps are repeated to estimate other spike lags and amplitudes. The difference between the observed horizontal component and vertical receiver function convolution is reduced with the iteration for additional spikes in the receiver function. The iteration stops when there is no significant improvement in misfit between the observed and synthetic receiver functions (Ammon, 1991).

It is different to use the iterative deconvolution in water-level from the inversion codes. If the receiver functions are used for simple stacking, normalization is not critical. However, to use the receiver function calculated with iterative deconvolution, it is necessary to normalize by the area of the averaging function, which is shown in Table 3.2. In this study, all receiver functions computed with an *a* value of 2 were divided by 1.2, and receiver functions computed with an *a* value of 5 were divided by 2.83.

Gaussian width factor *a*	Divide Iterdecon Rftn by
0.5	0.29
1.0	0.57
1.5	0.85
2.0	1.20
2.5	1.42
3.0	1.70
5.0	2.83

Table 3.2 Constants for the normalization of iterative deconvolution receiver function.

3.1.4 Sampling range of receiver functions

The sampling range of a receiver function depends on the signal range and the depth of the velocity contrast. Figure 3.4 illustrates the geometry of P- and S-wave ray paths for an upper layer, with Ps conversion (P-to-S) and PpPmp (one of the P-wave multiples) if the bottom discontinuity is the Moho. This multiple is not normally used in receiver function analyses, but provides a useful bound on the lateral sampling of the structure.

The Ps phase samples very close to the station, while the multiples average the structure over a distance slightly less than 3 Xp as shown in Figure 3.4. From Snell's Law

$$Xs = h * \tan(\sin^{-1}(p*Vs))$$

$$Xp = h * \tan(\sin^{-1}(p*Vp))$$

where h is the thickness of the upper layer, p is the ray parameter, Vp is the P-wave velocity, and Vs is the S-wave velocity (Ammon, 1997). Therefore, the lateral sampling is generally three times the depth to the deepest discontinuity.

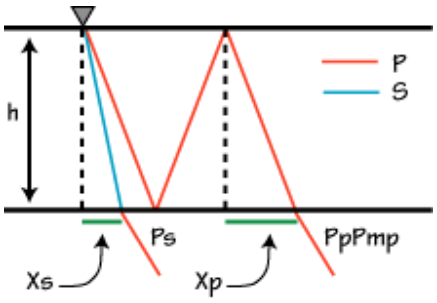

Figure 3.4 Ray diagram to illustrate how to estimate the lateral resolution of receiver function (Ammon, 1997).

3.1.5 Advantages of receiver function analysis

In the Nechako Basin, receiver functions are suitable for modeling the crustal structure, especially under the volcanic layer near surface. Because of this volcanic cover, it is difficult for energy from a surface source to penetrate into the crust. Since receiver function analysis uses the teleseismic energy coming from below, it is an effective method to produce images of the structure beneath the stations in the Nechako Basin.

Using this teleseismic energy through receiver functions provides site-specific information (directly under the recording site) whereas ambient noise studies give the average structure between two stations. Therefore, the two methods can be used to complement each other.

Receiver functions also have the ability to determine if the interface is dipping. A number of receiver functions with different back azimuths may be used to detect the presence of a dipping layer. Examples of dipping structure will be given in the next chapter on data processing.

The cost of the receiver function analysis is lower than other geological studies since the main charge is only for portable broadband seismic stations to collect the suitable teleseismic waveforms. The relatively simple procedure for calculating the receiver function is another advantage of receiver function analysis.

3.2 Neighbourhood Algorithm

Receiver function inversion is well-known to be a complex non-linear problem. It is difficult or impossible to solve it with a linearized approximation since the linearization requires calculation of partial derivatives of data with respect to model parameters. Therefore, the derivative-free direct search methods are commonly used for this complex non-linear and non-unique problem. The inversion method used in this study is based on the Neighbourhood Algorithm developed by Malcolm Sambridge (Sambridge, 1999).

3.2.1 Non-linear inversion

Early direct search methods were based on uniform pseudo-random sampling of a parameter space (Wiggins, 1969). Monte Carlo methods (Hammersley & Handscomb, 1964) were used extensively for probabilistic or randomized searching of a finite dimensional parameter space. The main problem with these early direct search methods was that they were limited by the dimensionality of the parameter space due to computational constraints. Moreover, early direct search methods had difficulties to uniquely determine model parameters, which also occurs in linearized methods. There may be no or an infinite number of models that satisfy the data.

To address this issue, the simulated annealing (SA) method was introduced into geophysics (Kirkpatrick et al., 1983). This stochastic direct search method was developed for global optimization problems. After SA, genetic algorithm (GA) was also brought into geophysics (Stoffa and Sen, 1991) from computer science (Holland, 1975), which

also seeks a model giving a globally optimal data misfit value within a pre-defined finite-dimensional parameter space. For both SA and GA, the basic method needs more applications to determine suitable control parameters to fit the data to a satisfactory level (Gallagher and Sambridge, 1994; Sen and Stoffa, 1995); however, it is not always so easy to determine these parameters. In addition, it is possible to have many local minima, or a very complex data misfit function. It may be inappropriate to optimize the model properties. In this case, an optimal model is not easy to find. On the other hand, Neighbourhood algorithm (NA) has a different point of view rather than optimization in order to make up for the weak point of SA or GA. It characterizes the entire emsemble of acceptable solutions directly by first trying to generate as many members as possible, and then analyzing them.

3.2.2 Searching a parameter space for non-linear inversion

The idealized algorithm has three steps for searching a parameter space properly. First, it is necessary to construct the approximate misfit surface from the previous models for which the forward problem has been solved. Second, this approximation is used for generating the next set of samples with a chosen search algorithm. Finally, these new samples are added to the previous samples, and then the algorithm goes back to the first step. Sambridge refers to this as the idealized search algorithm in developing NA (Sambridge, 1999). NA uses the previous model space samples to approximate the misfit function everywhere in the model space. This is a simple but powerful searching algorithm, which is different from other methods. Uniform Monte Carlo search (UMC)

makes no use of previous samples in the parameter space because each new sample is independent from the previous samples, and both GA and SA uses the previous samples but in complex ways.

3.2.3 Voronoi cells

The NA uses a special geometrical construct called a Voronoi cell (Figure 3.5) (Okabe et al., 1992; Watson, 1992; Sambridge et al., 1995). It is simply the nearest neighbour region about one of the previous samples as measured by a particular distance measure. This is not only a unique way of dividing the multidimensional model space, but also a simple way. The neighbourhood approximation to the misfit surface is generated by setting the misfit to a constant value inside each cell since the data misfit function is known at all previous samples.

Both Figure 3.5 and 3.6 show how new Voronoi cells are developed from the previous samples, the distribution and density of cells. Nine initial points are shown as black filled-dots, one for each Voronoi cell, and seven circles in the middle shaded cell represent the new centers for the next models (Figure 3.5 a). Those seven circles change into the new initial points for the next samples. As those steps are processed, the previous cells shrink when new cells are generated (Figure 3.5 b). While the parameter space is divided into smaller Voronoi cells, the samples always keep the distance between their neighbours and themselves so that the cell boundary is halfway between the initial point and each neighbour. This way makes each cell unique. The size and shape of the neighbourhoods about each sample are completely determined by the samples themselves.

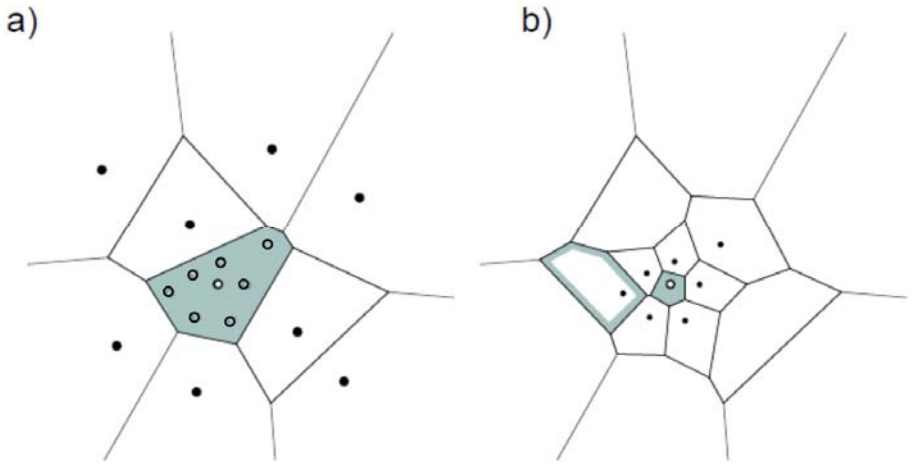

Figure 3.5 Voronoi cells in searching parameter space (Sambridge, 1999).

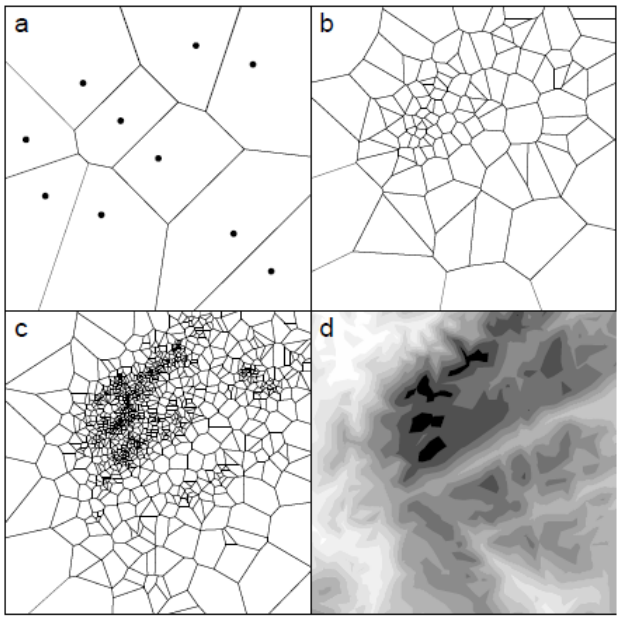

Figure 3.6 a) 10 quasi uniform random points and their Voronoi cells. b) The Voronoi cells about the first 100 samples generated with the neighbourhood approximation. c) Similar to b) for 1000 samples. d) Contours of the test objective function. As samples are generated, the approximation to the multi-modal surface becomes more accurate (Sambridge, 1999).

Also, it is clear that the local sampling density has increased with the new models. The center of sampling density in parameter space for NA can increase, decrease or shift. However, for any distribution and density of samples, the size of each cell is inversely proportional to the sampling density (Figure 3.5 and 3.6).

3.2.4 Neighbourhood Sampling

The neighbourhood approximation represents an idealized algorithm, as stated in chapter 3.2.2 of this thesis, in terms of the NA-surface with Voronoi cells. This approximation can be incorporated into any existing direct search method; for example, GA or SA can be inserted into the second step of the idealized algorithm. However, a new direct search method, Neighbourhood sampling algorithm, uses the spatial properties of the Voronoi cells to directly guide the sampling of the parameter space. This generates new samples by resampling chosen Voronoi cells with a locally uniform density.

The Neighbourhood sampling algorithm has one more step than the idealized algorithm, i.e., four steps in total. It starts with an initial set of models generated in the parameter space. After the misfit function is calculated for the models which were most recently generated, the lowest misfit of all models is determined. Then, new models are generated by performing a uniform random walk in the Voronoi cell of each of the chosen models with the lowest misfit. The new models generated in the third step are added to the parameter space, and the algorithm returns to the second step. If a larger value is used for the number of the lowest misfit models which are picked in the third step, sampling at each iteration is spread over more cells. This makes the algorithm more

exploratory in nature; on the other hand, the sampling should be more localized with smaller values.

3.2.5 Advantages of Neighbourhood Algorithm

The NA has two significant features. First, the size and shape of the neighbourhoods are determined automatically and uniquely by the previous samples. Second, the algorithm only requires models to be evaluated for their relative fit to the data, not seeking for the best fit, because it uses only the rank of the misfit/objective function. This helps to determine the 'better-fit-model' when it is difficult to quantify the difference accurately between two different models.

It is well-known that GA can produce an ensemble containing models that are partial or full copies of each other (Shibutani et al., 1996). However, NA not only carries out sparser sampling in the model space than other non-linear inversion methods, but also more concentrated sampling near the model with smallest misfit. Sambridge presented an example which illustrates this advantage of NA (Sambridge, 1999). He used both GA and NA for the comparison of the inversion of receiver functions recorded in eastern Australia with the same parameterization of crustal structures as was used by Shibutani et al. (1996). In Figure 3.7, ensembles of 10000 models generated by GA and NA and plotted on the left and right, respectively. The best model among them is represented as a red cross, and the true model of this inversion is shown as a blue x. The distance between the best model generated by NA and true model is closer than that for GA in all cases, which means NA produced a better final model. Furthermore, all samples of GA fall on a

relatively coarse grid, while NA produces a diverse cloud of samples with sampling concentrated in the neighbourhood of the best-fit model. This diversity of NA ensembles is more useful for characterizing the region of acceptable models (Sambridge, 1999).

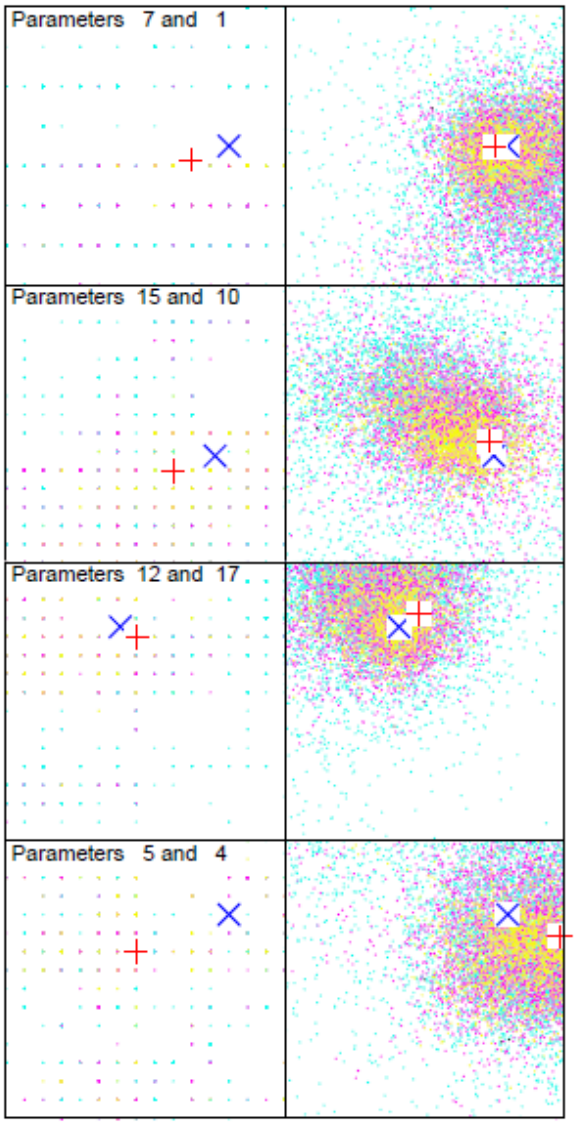

Figure 3.7 Comparison of ensembles produced by GA (left panels) and NA (right panels) projected onto four pairs of parameter axes (labeled) for the receiver function inversion. The best of the 10000 models in each panel is shown as a red cross and the true model as a blue x. The dots are colored from blue through red to yellow as the data fit increases (Sambridge, 1999).

Chapter 4 Data Collection & Processing

4.1 Data collection

The technique used in this study, receiver function analysis, is based on matching P-wave Ps conversions in measured and synthetic seismic waveforms for distant earthquakes. In order to calculate the receiver functions properly, these distant earthquakes (teleseisms) should have intermediate to large magnitudes (M > 5.5) since earthquakes with smaller magnitudes do not generate clear peaks and troughs in the waveforms. Furthermore, it is important to record teleseisms within the distance range of 30-100° (3,360-11,200 km). For measurements closer than 30°, the P-wave of the waveform is complicated by upper mantle travel path effects. On the other hand, if it is farther than 100°, the station is located within the shadow zone of the direct P-wave.

4.1.1 POLARIS seismic station array

In September 2006, seven three-component broadband seismic stations were deployed across the Nechako basin area in order to sample a large portion of the basin, and two additional stations were deployed in October and November 2007 due to unexpected local earthquake swarms in this area (Cassidy et al., by personal communication, 2008). Some of these stations (CLSB, RAMB, THMB, and FLLB) are close to existing boreholes or areas of the basin been studied previously. All stations are

shown in Figure 4.1, and the exact locations are listed in Table 4.1 in terms of latitude, longitude, and elevation.

The POLARIS stations utilize solar power and satellite data transmission to continuously record ground shaking and transmit the data in real time. The data are archived at data collection centres of Geological Survey of Canada in Sidney, BC and Ottawa, ON.

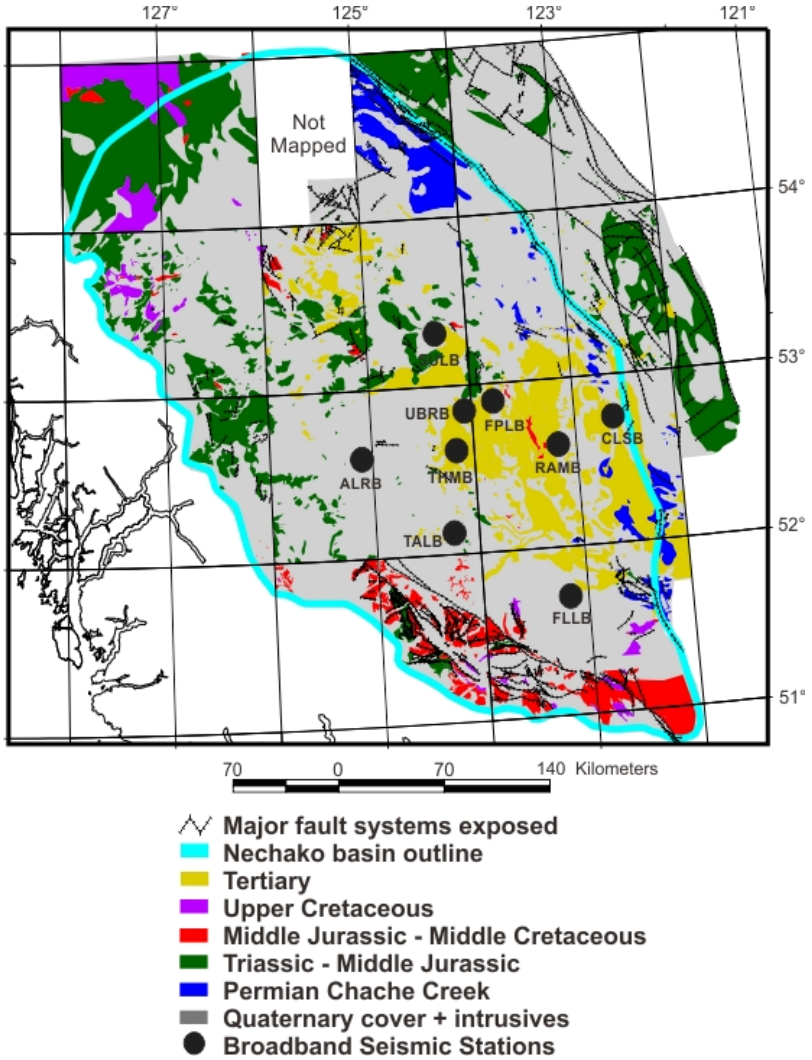

Figure 4.1 The location of POLARIS seismic stations on the simplified geological map of the Nechako Basin (base map from Hayes et al., 2002).

Seismic Station Location	Code	Latitude	Longitude	Elevation (km)
Anahim Lake, BC	ALRB	52.5104	-125.0846	1.237
Cack Lake, BC[1]	CLSB	52.7589	-122.5565	0.792
Fletcher Lake, BC	FLLB	51.7396	-123.1087	1.189
Southwest Quesnel, BC	RAMB	52.6320	-123.1237	1.259
South of Vanderhoof, BC	SULB	53.2786	-124.3576	1.171
Tatla Lake, BC	TALB	52.0145	-124.2546	1.127
Thunder Mountain, BC	THMB	52.5486	-124.1320	1.126
Upper Baezaeko River, BC	UBRB	52.8918	-124.0832	1.243
Fishpot Lake, BC	FPLB	52.9540	-123.7790	1.005

[1] unofficial place name

Table 4.1 Location for POLARIS seismic stations.

4.1.2 Dataset

During the two years of operation (September 2006 – August 2008), more than 1000 intermediate to large teleseisms were recorded by the POLARIS stations, but among these events, about 40 waveforms have sufficient quality for receiver function analysis (Figure 4.2). These events cover a wide range of azimuths and distances, providing a suitable dataset for examining geometry (dip angle and strike direction) of the structural boundaries beneath the seismic stations.

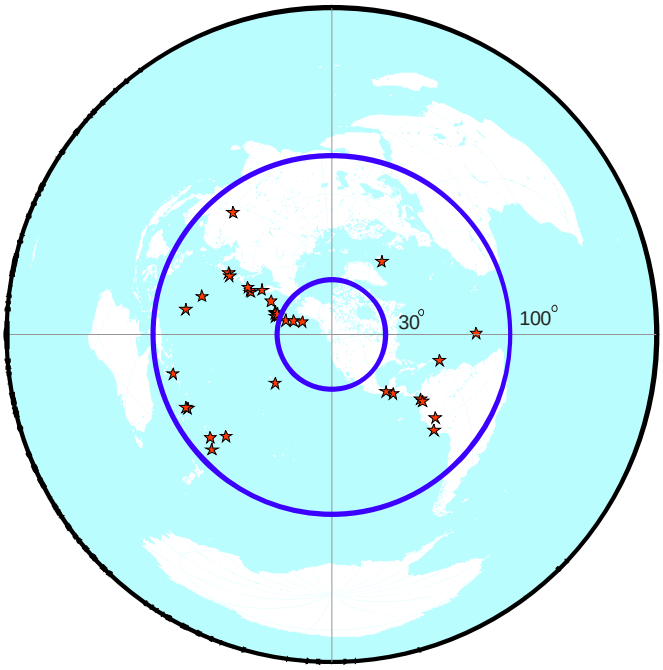

Figure 4.2 Earthquake locations used to calculate the receiver functions are shown as red stars. The map is centered on the study area of the Nechako Basin. Blue circles indicate the minimum and maximum distance range of useful teleseisms, which is 30˚ and 100˚, respectively.

4.2 Data processing

In this thesis, receiver functions are generated using a three-dimensional ray tracing code written by Owens (1984) and based on Langston (1977). To calculate receiver functions from the teleseismic waveforms and subsequently invert them for the Earth model, it is important to understand how the parameters in the crustal structure model affect the receiver function. In this section, the relationship between the three main parameters (layer thicknesses, near-surface structure with thin low velocity layer on the top, and dipping interface) and the arrivals in the receiver function will be explained with several simple examples.

For the layer thicknesses, there are three examples with different thicknesses: 10 km, 15 km, and 20 km. The examples of near-surface structure contain 0.75 km thick and 1.5 km thick sediments on the surface, and they are compared with a model without any thin sedimentary layer. Finally, a model with a dipping layer is shown with seven synthetics of radial and tangential receiver functions sampling a range of back azimuths.

The example models have three layers each, with constant P-wave velocity and S-wave velocity ratio (Vp/Vs) of 1.79. All examples have the same ray parameter (slowness) of 0.068 s/km (at $\Delta = 45°$). In terms of S-wave velocity (Vs), the top layer is 2.60 km/s, the middle layer is 3.60 km/s, and the bottom layer is 4.60 km/s, and densities are 2.53 g/cm^3, 2.80 g/cm^3, 3.30 g/cm^3 respectively (Figure 4.3 (A)).

4.2.1 Layer thickness

One of the main properties in the crustal model is the thickness of the various layers. In general, layer thickness directly controls the arrival times of the peaks or troughs in the receiver function. Model (A) in Figure 4.3 is the base model for all examples in this chapter. It has two 15 km thick layers above the Moho. The synthetic receiver function generated for this model has three sharp peaks at 0, 2.5, and 4.5 s (relative time).The first peak corresponds to the direct P-wave arrival, the second peak is the Ps conversion from the first discontinuity at 15 km depth, and the third peak is from the Moho (30 km depth).

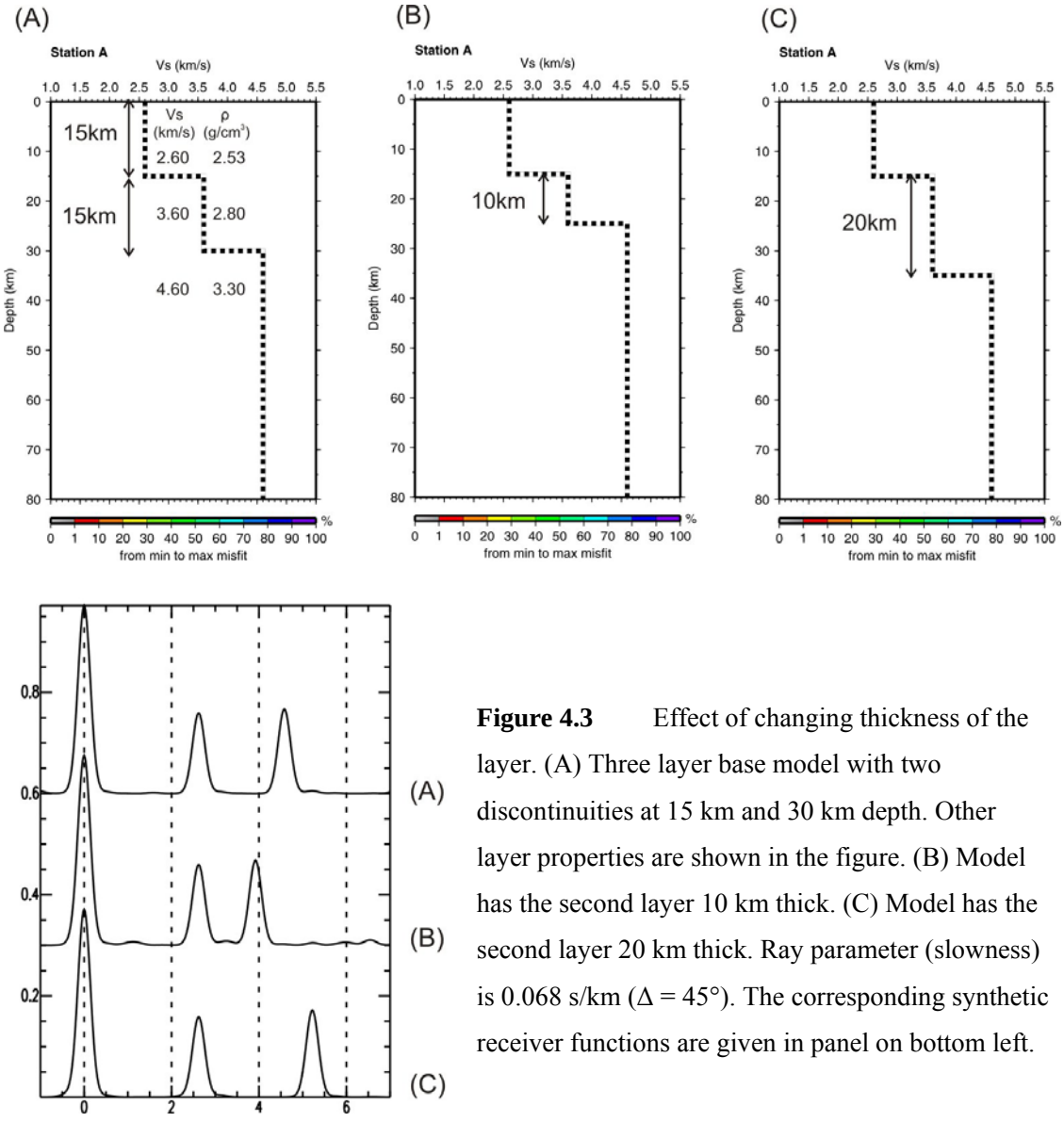

Figure 4.3 Effect of changing thickness of the layer. (A) Three layer base model with two discontinuities at 15 km and 30 km depth. Other layer properties are shown in the figure. (B) Model has the second layer 10 km thick. (C) Model has the second layer 20 km thick. Ray parameter (slowness) is 0.068 s/km ($\Delta = 45°$). The corresponding synthetic receiver functions are given in panel on bottom left.

In model (B), the second layer is thinner (by 5 km) than that in model (A). This decreases the arrival time of the third peak by about 0.5 s, but the direct P-wave arrival and the first converted arrival do not change since only the depth of the second discontinuity is changed. On the other hand, model (C) has a second layer that is thicker than (A) by 5 km, measuring a deeper Moho. Therefore, the synthetic receiver function

generated for model (C) shows the third peak about 0.5 s later than for (A). It is clear that if the discontinuity is located at shallower depth, the converted arrival is earlier, but if it is at deeper depth, the corresponding arrival comes later.

4.2.2 Shallow structure

It is common to have thick sediments on the surface, especially in basins. In this section, two simple models with sedimentary layers at the surface are presented to compare with a model having no sediment layer (Figure 4.3 (A)). The previous section shows that the receiver function arrival time is related to the layer thickness (discontinuity depth). This section shows that the shallow structure affects the amplitude or width of the peaks.

In Figure 4.4, models (D) and (E) are similar to model (A) in Figure 4.3 but include a 0.75 km or 1.50 km thick low S-wave velocity layer (Vs = 1.60 km/s) at the surface, respectively. Figure 4.4 shows that the synthetic receiver functions are changed significantly by the low-velocity layer, relative to those computed for model (A) in Figure 4.3, with arrivals of smaller amplitude and increased time duration. In addition, the arrival structure is more complicated, particularly the direct P-wave arrival, with the single sharp peak changed into a double or triple peak. The near surface structure also generates minor peaks and troughs due to the constructive or destructive effects from multiples. However, all three main peaks from model (A) are maintained in both model (D) and (E) at about the same arrival time.

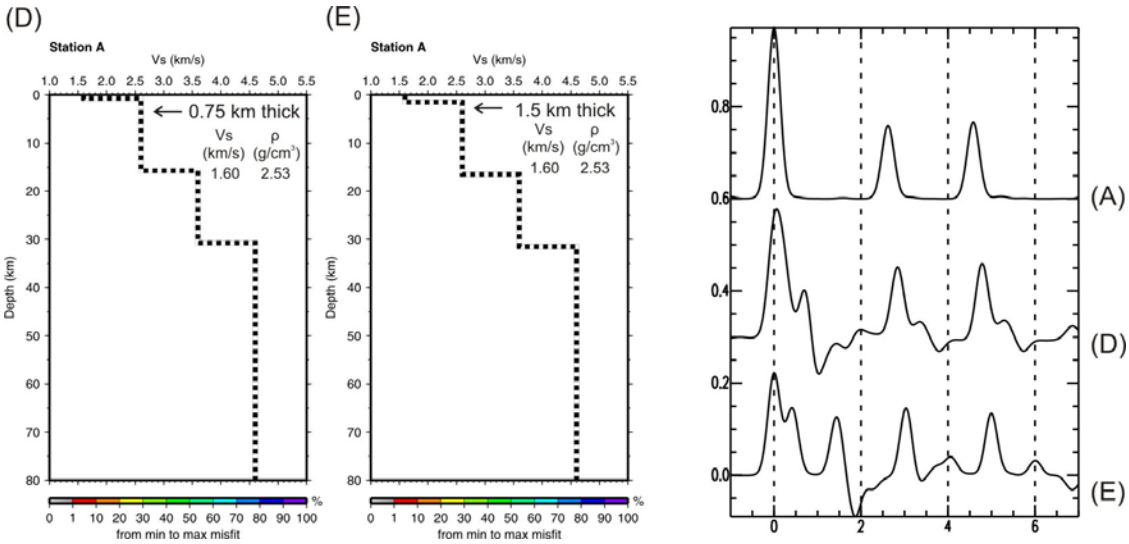

Figure 4.4 Effect of shallow structure. (D) and (E) Models with 0.75 and 1.5 km thick low velocity layer at surface, respectively (Vs = 1.60 km/s, ρ = 2.53 g/cm^3; other properties are the same as Figure 4.3 model (A)). The corresponding synthetic receiver functions are given in panel on right.

4.2.3 Dipping structure

The previous models presented in this chapter include only horizontal layers. However, dipping structures such as faults and folds are not uncommon in the Nechako Basin. In this section, an example of dipping structure is shown to illustrate the azimuthal variation in the receiver functions from both radial and tangential synthetic waveforms.

Model (F) in Figure 4.5 is identical to Model (A) in Figure 4.3, except that the first discontinuity at 15 km depth dips southward at 20°.

In the radial synthetics, the first peak is direct P-wave arrival, the second peak at about 2.5 s corresponds to the Ps conversion from the dipping discontinuity, and the third peak is related to the Moho. After the main three peaks, other arrivals are generated by multiples. Although the arrival times are almost the same, the amplitudes vary

significantly with back azimuth. The waveforms from the south, which is the dip direction, have higher amplitude arrivals than others because the relative angle of this waveform to the dipping surface is more vertical. When the waveform is coming from the opposite direction (north), the angle between the dipping plane and the ray path is larger. Therefore, the result of deconvolution of the vertical component by the corresponding radial component has smaller amplitude. Other than the amplitudes of the second arrivals, there is another change: the presence of multiples after the Moho arrival, which do not exist in the synthetics generated by Model (A). In addition to the radial synthetic waveforms, the tangential receiver functions are often useful to determine dipping layers in the crustal structure. As shown in Figure 4.5, tangential receiver functions indicate the dipping discontinuity by polarity changes. Based on the dip direction (south for this example), the tangential receiver function from the same direction as the dip does not show any new arrivals or arrivals with smaller amplitude. However, when there are several interfaces dipping in different directions, finding the pattern in the tangential receiver function to determine the dipping angles and directions may be very difficult. Therefore, I modelled only the radial receiver functions in this thesis.

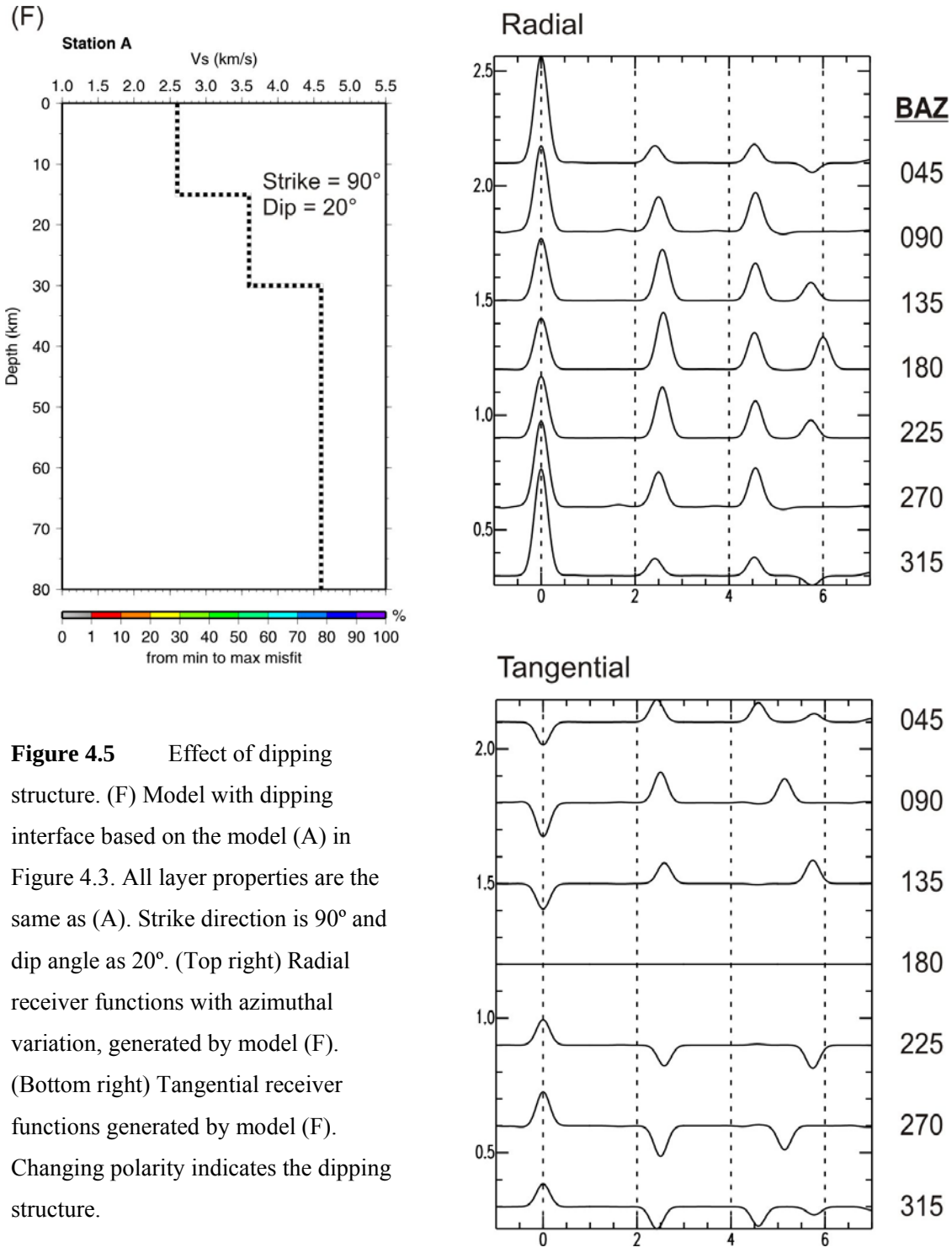

Figure 4.5 Effect of dipping structure. (F) Model with dipping interface based on the model (A) in Figure 4.3. All layer properties are the same as (A). Strike direction is 90º and dip angle as 20º. (Top right) Radial receiver functions with azimuthal variation, generated by model (F). (Bottom right) Tangential receiver functions generated by model (F). Changing polarity indicates the dipping structure.

Chapter 5 Results

Constructing velocity models for the crustal structure of the Nechako Basin from teleseismic receiver functions using the Neighbourhood Inversion Algorithm is the purpose of this study. In this chapter, crustal S-wave velocity models are determined for each station in the Nechako basin and observed and synthetic teleseismic receiver functions are compared. Most of the models contain 6 layers: sediments on the top, volcanic cover, upper crust, middle crust, lower crust, and upper mantle. In some cases, dipping structures are required for the top two layers (sediments and volcanic cover).

5.1 SULB

SULB is the northern-most station of the seven original POLARIS broadband seismic stations in the Nechako Basin. It is located south of Vanderhoof, BC at 53.2786 N, 124.358 W and at an elevation of 1.171 km (Figure 4.1). There are limited data from previous geophysical studies at this site - seismic lines (such as the Canadian Hunter 1980's reflection line) and wells are relatively far away. The closest seismic line and gravity study line are about 25 km from SULB, and well (b-22-K) is 58 km to the south. Moreover, seismic image quality (reflection strength/continuity) near SULB is poor compared to other stations. The 2008 MT study (Spratt and Craven, 2008) line is adjacent to SULB, and preliminary MT results show a low resistivity layer from the surface to about 2 km depth; however, it is not clear whether this is due to Eocene Ootsa Lake

volcanics or Cretaceous sediments. Nevertheless, the MT results and the well sonic logs from b-22-K provide some useful information (see Figure 2.1 for the location of wells).

SULB is on the Miocene-Pliocene flood basalts, which is part of the Chilcotin group (Figure 4.1). This flood basalt layer is generally up to 150 m thick in this region (Ferri and Riddell, 2006), and is shown in the well log in chapter 2. The estimated S-wave velocity from the well log and first-arrival tomography inversion for the near surface is about 1.6-2 km/s. Furthermore, the MT results suggest that there is a 2 km thick high resistivity layer (likely late granitic plutons or basement terranes) at about 2-4 km depth.

Although SULB has limited constraints from previous studies (as discussed above), it has the simplest receiver functions of all the stations in the POLARIS Nechako array. All radial receiver functions calculated at SULB show large and relatively simple direct P-wave arrivals. They also have a clear phase (interpreted as the Moho Ps conversion) near 4.2 s. Those phases are consistent in all receiver functions at this site (Figure 5.1).

At this site, I used six horizontal layers, including top surface sediments and volcanic cover, as a starting model. Note that there is evidence for shallow structure (surface sediments) because most of the observed receiver functions have a phase with small amplitude immediately following the direct P-wave arrival. Modeling these data revealed that horizontal layers could not match the observed delay of the direct P-wave arrivals for some of the receiver functions (specifically back azimuths of 114, 129, and 132˚).

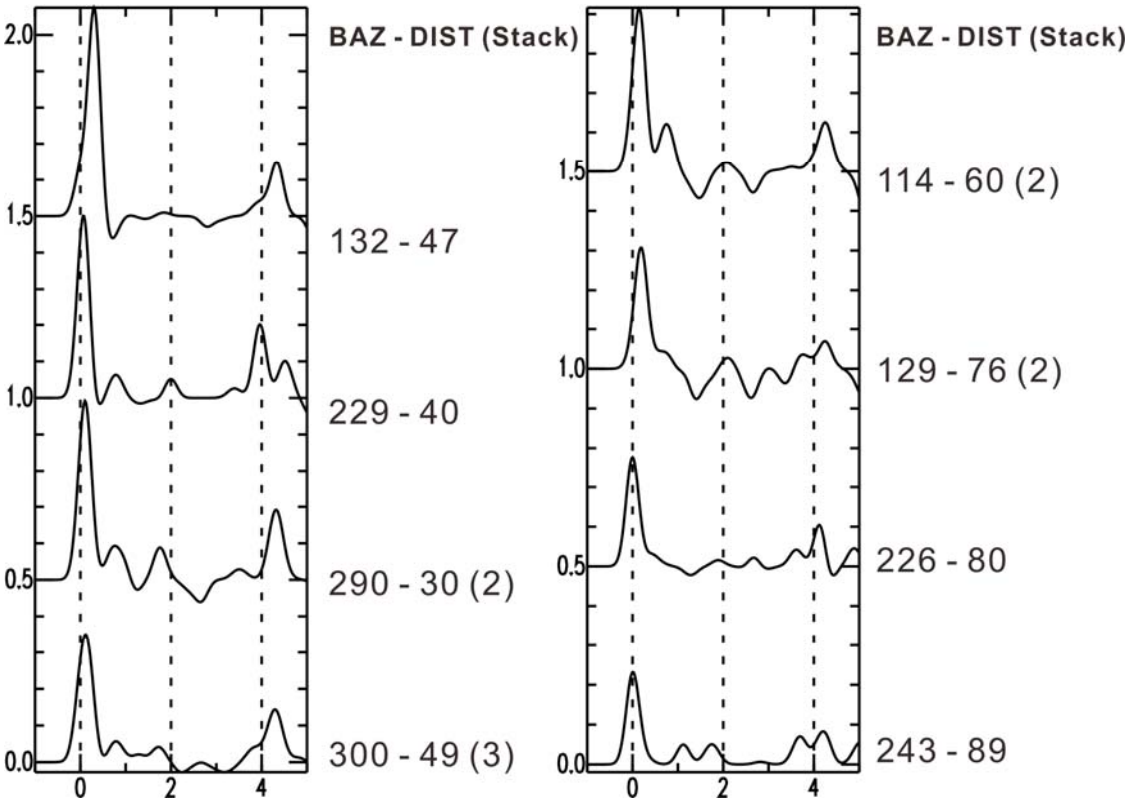

Figure 5.1 Observed radial receiver functions for SULB, plotted in order of back azimuth (BAZ) and distance (DIST) from the event. Stacked waveforms are labeled with the number of original waveforms included in the stacked trace. The Moho Ps conversion is clear at about 4.2 s.

This azimuthal variation in the arrival time of the direct P-wave requires shallow dipping structure beneath SULB. Based on the simple forward modeling in chapter IV, the dip direction is approximately in the direction of the synthetics which exhibit shifting. For SULB, all waveforms from the east and southeast directions show clear shifting of the direct P-wave arrival. They also have smaller amplitudes which suggest that the top layer is dipping in the same direction as well. Initially, I utilized forward modeling to examine dipping layers (upper two layers) for strike directions ranging from 45 to 135 degrees. An assumption of the forward modeling is that the upper two layers are dipping

in the same direction because these layers are both too thin to have different dip directions.

Figure 5.2 shows one of the best solutions obtained from modeling (using NA inversion) for the SULB receiver functions. The top sediment layer is 1.0 km thick with Vs of 2.0 km/s, and the second volcanic cover is 3.9 km thick with Vs as 3.7 km/s. Both layers are dipping at an angle of 7.1° with a strike of 85.7°.

Figure 5.3 compares the observed waveforms (black) and the synthetics generated using this model (red). Note that in the inversion process, those traces that are stacks of more than one event (e.g., trace 300-49 in Figure 5.2) have a higher weighting. Overall, this model provides a very good fit to the observed data – especially to the Moho conversions near 4.2-4.3 s.

According to the model in Figure 5.1, the Moho is at about 36 km depth with a large contrast in Vs. This is consistent with the data since the peak for the Moho has high amplitude with clear sharp feature at about 4.2 s (Figure 5.3). In addition, the negative phase before the Moho phase (around 3 s) indicates a low velocity layer above the Moho, which extends from about 28 to 36 km depth in the model.

The model in Figure 5.2 contains reasonable features, and generates the synthetics with relatively low misfit. However, to examine constraints on the shallow structure especially, I developed a second model for SULB. It uses the same receiver functions, and under the same condition of boundaries for all layers, except the first layer. In the first model (Figure 5.2) the minimum thickness for the first layer is 1 km, and the inversion result yields a thickness of 1.0 km. To explore the possibility of a thinner layer,

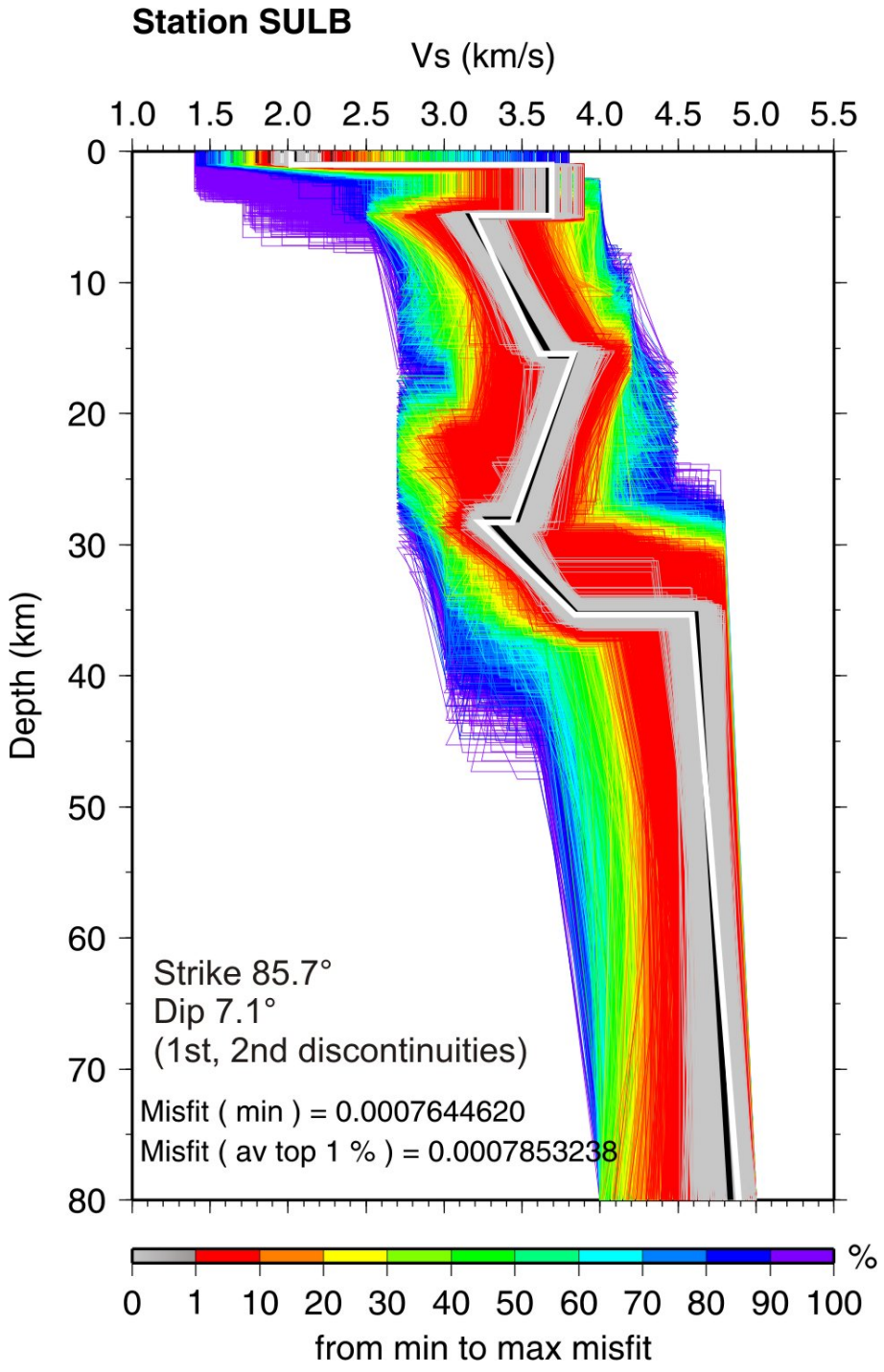

Figure 5.2 S-wave velocity model of SULB, in terms of a density plot of the 2000 best-fitting models generated by the NA with the minimum thickness of 1 km for the top layer. The best-fitting model is plotted in white, and the average model computed from the 1% of models with the lowest misfit is plotted in black. The misfit of the best-fitting model and top average 1% models are given. The rainbow colour scale shows decreasing misfit, from purple to red and grey.

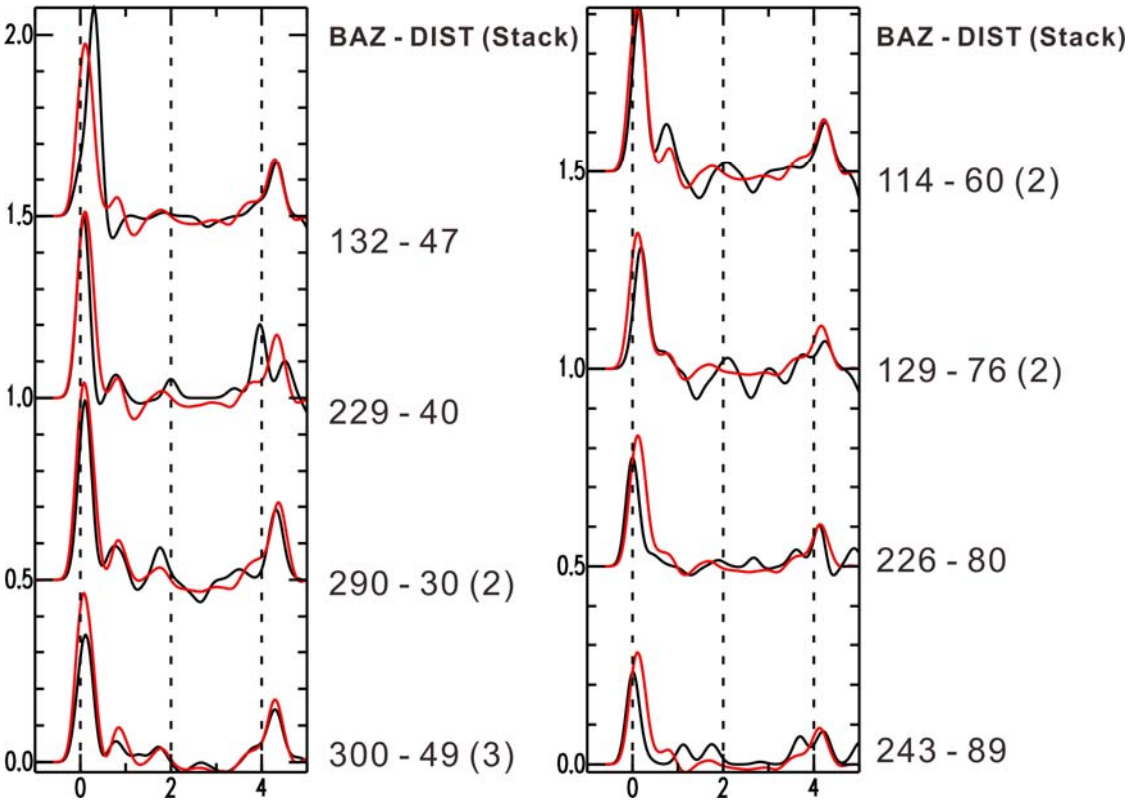

Figure 5.3 Observed waveforms (black) and synthetic receiver functions for the best-fitting model (red) for SULB, generated by the model with minimum boundary of 1 km depth for the uppermost layer. Receiver functions are plotted in order of back azimuth (BAZ) and distance (DIST) from the event. Stacked waveforms are labeled with the number of original waveforms included in the stacked trace. The Moho Ps conversion is clear at about 4.2 s.

the inversion was re-run with a minimum layer thickness (for layer 1) of 0.1 km. The resulting model, shown in Figure 5.4, has a first layer thickness of 0.5 km.

The two models shown in Figures 5.2 and 5.4 have general features of upper, middle, and lower crust which are similar to each other, as well as the depth of Moho. Also, the dip direction and angle of the first two layers agree to within about 5°. Because the second model allows for a thinner layer for the top surface, the main difference between the two models is in the top two layers. For the second model, the top two layers

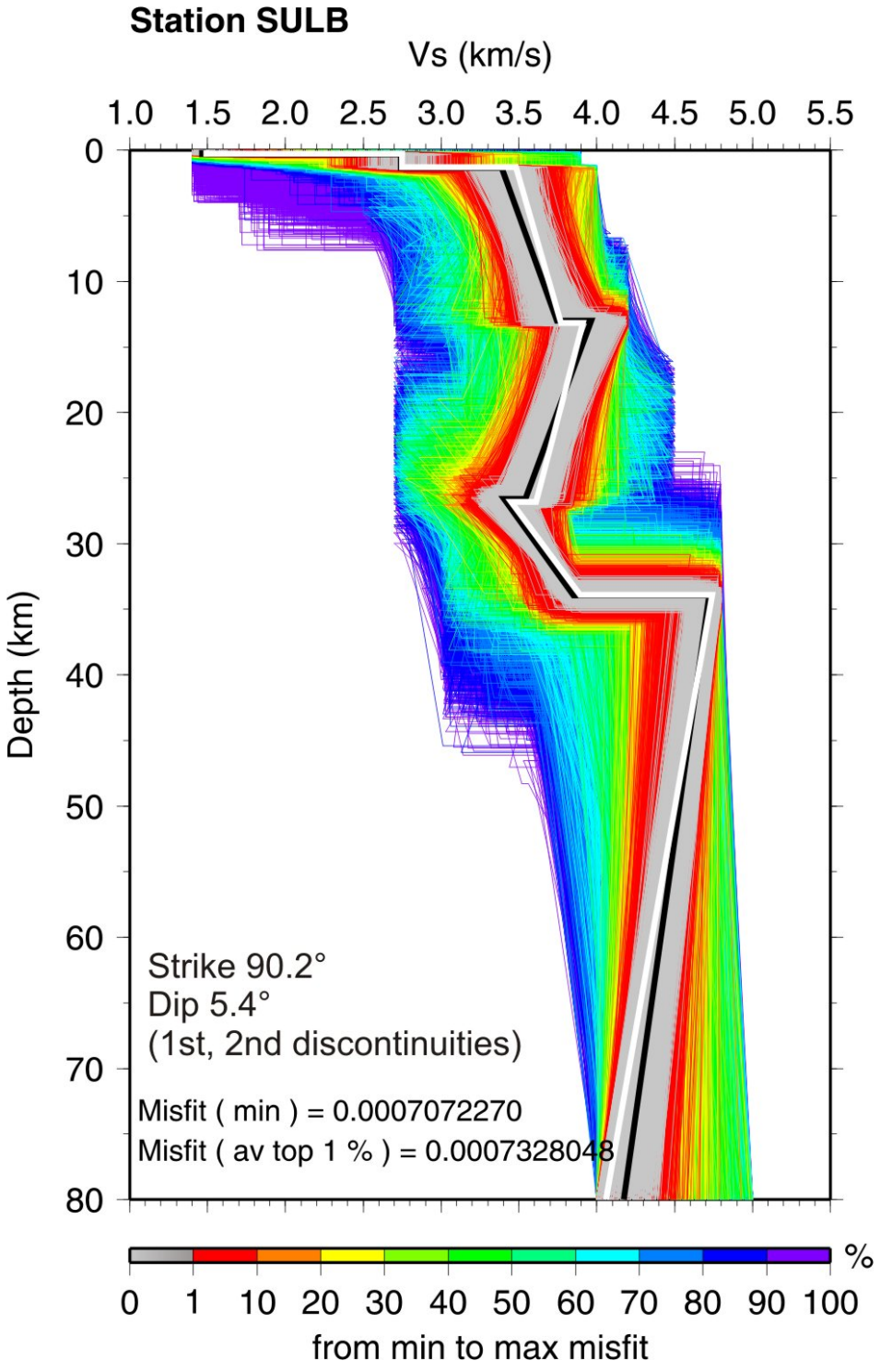

Figure 5.4 S-wave velocity model of SULB, in terms of a density plot of the 2000 best-fitting models generated by the NA with the minimum thickness of 0.1 km for the top layer. Other descriptions are the same as for Figure 5.2.

show a gradient whereas the first model has high contrast of S-wave velocity between the first and second layers, changing from 1.5 km/s to 2.8 km/s at 0.5 km depth, then to 3.5 km/s at about 2.3 km depth. Also the thickness of second layers is different: the second model has a 1.8 km thick second layer while the thickness for the first model is 3.9 km. Since the synthetic receiver functions from both models provide a good fit to the observed data (Figure 5.3 and 5.5), it is not clear which is better. Misfits of the best model in each case are also similar; for the first model, it is about 0.00076, and for the second model, it is about 0.00070. Note that in both cases the velocity gradient in the mantle is not constrained by the data or modeling.

As the result from the two final models above for SULB, it is obvious that there is a sharp Moho in this area, it is located at about 36 km depth, and there is a low velocity zone above the Moho that is about 7 km thick. Furthermore, it is clear that a layer of low velocity sediments exists near the surface with Vs of about 1.5-2 km/s. Another layer of high Vs (3.5-3.8 km/s) is found beneath, perhaps representing the volcanic cover.

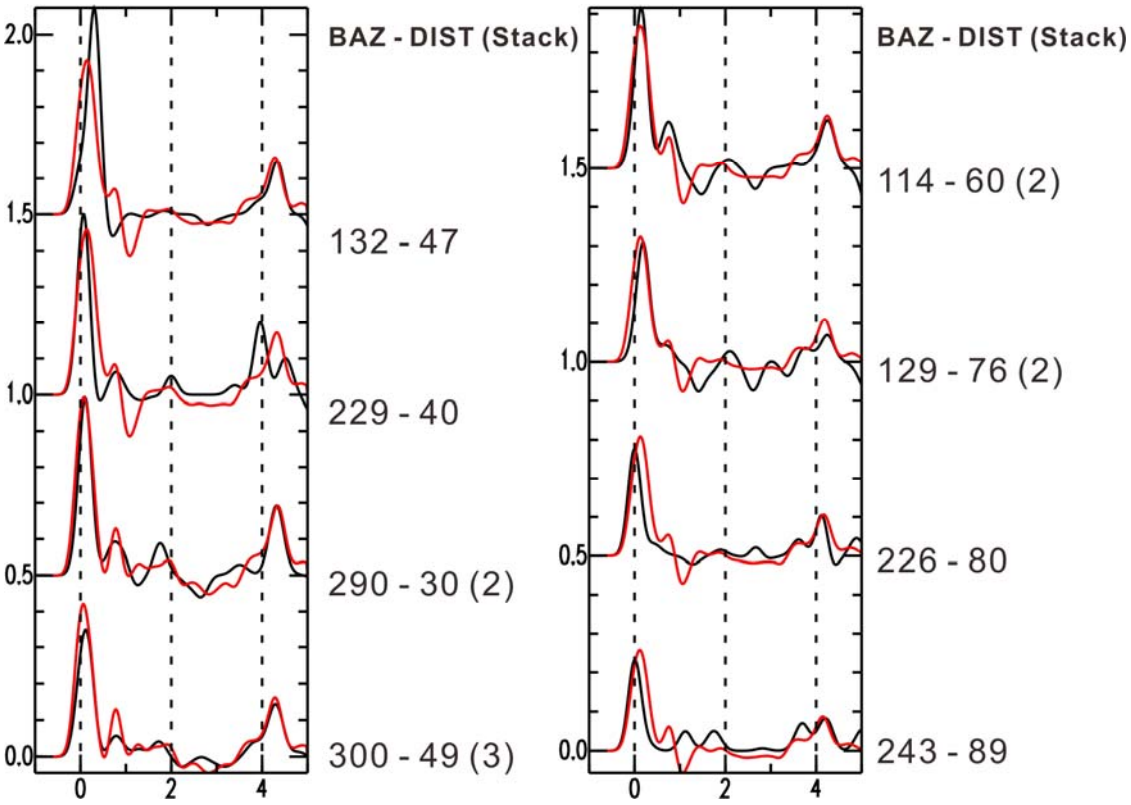

Figure 5.5 Observed waveforms (black) and synthetic receiver functions for the best-fitting model (red) for SULB, generated by the model with minimum boundary of 0.1 km depth for the uppermost layer. Other descriptions are the same as for Figure 5.3.

5.2 CLSB

The second station CLSB (Figure 4.1) is located at Cack Lake near Quesnel, BC (52.759 N, 122.555 W, elevation 0.792 km). The receiver functions for CLSB are more complex than those for SULB, but they have consistent features, such as the Moho conversion near 4 s. This station provides the largest number of suitable waveforms for all different back azimuths. Another advantage of this station is that three boreholes (d-2-E, c-86-L, and c-84-D) are located only 5-10 km east of the station (Figure 2.1). Samples

from those boreholes indicate that from the surface to about 1.5 km depth the material consists mainly of shale, clays, and gravels, while below 1.5 km to the bottom of the well (around 3 km depth) the material is more metamorphosed volcanics, and green and grey quartzites. Because of the information from previous exploration of the basin and consistent features from all receiver functions, CLSB was chosen to be the second station for constructing an Earth model in this study.

Although CLSB has more near-surface constraints than SULB due to well logs, CLSB is not in any of the study areas for active seismic studies, MT, or gravity surveys. Moreover, there is no available sonic log which provides high-resolution P-wave velocity. Therefore, in my modeling, it is necessary to set large inversion search boundaries for S-wave velocity in each layer, based on the rock type in the description of well log.

For the first layer, the minimum of the top Vs is set to 0.5 km/s because the material contains loose gravels, clays, and shale. For the second layer, the minimum for the Vs is set to be 3.3 km/s since this is mainly metamorphozed volcanic, based on borehole indications.

For the CLSB inversion, receiver functions with Gaussian filter of $a = 2$ were used, whereas $a = 5$ receiver functions were applied for SULB. This is because the $a = 5$ receiver functions for CLSB are extremely complicated for straightforward inversion. Consequently, I use $a = 2$ receiver functions (Figure 5.6) to provide constraints on the main crustal features beneath CLSB. The purpose is to resolve the most important characteristics of the crust.

Phase shifting of the first direct P-wave arrival is generally related to either dipping structure or low velocity sediments near the surface (Cassidy, 1992). If phase

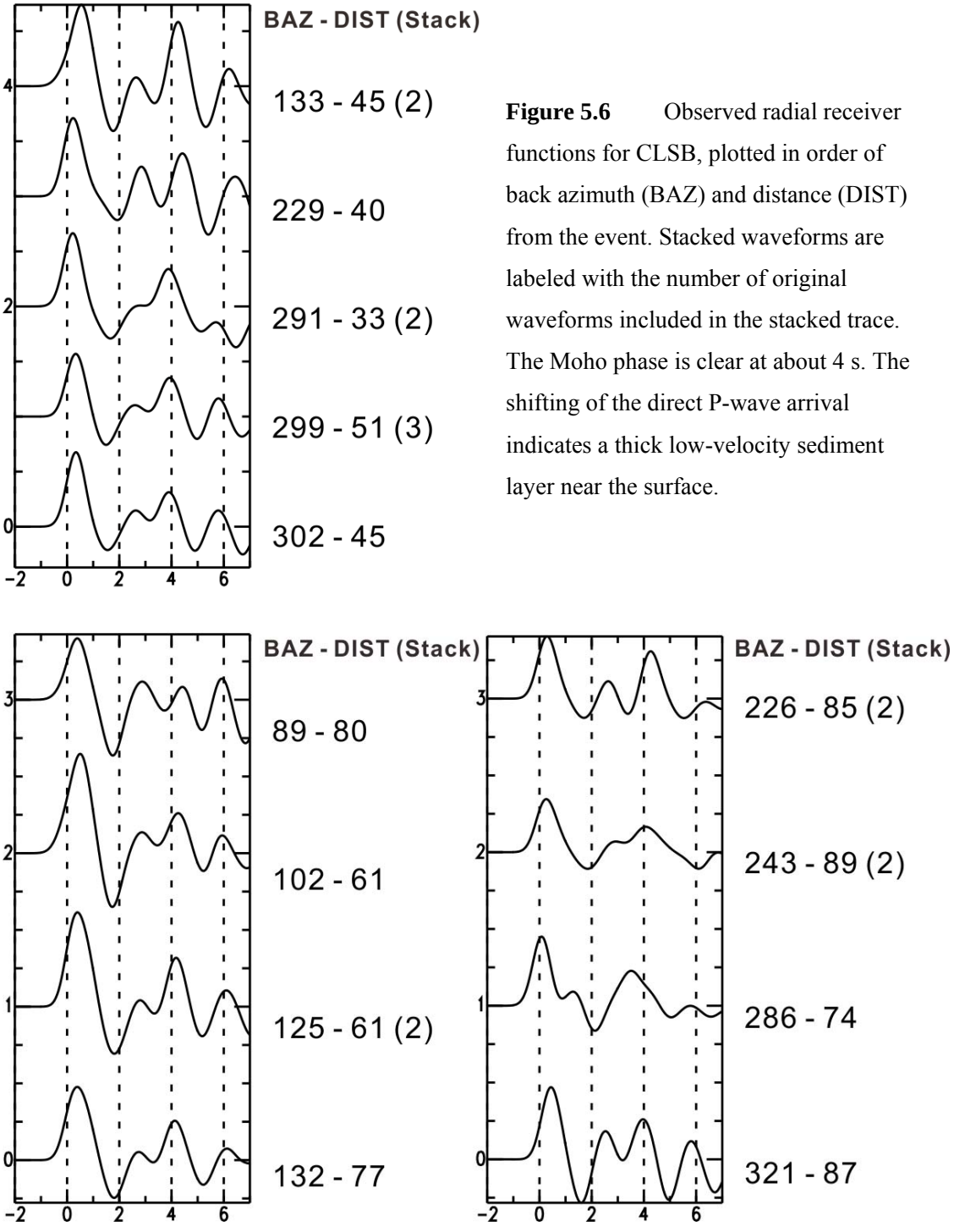

Figure 5.6 Observed radial receiver functions for CLSB, plotted in order of back azimuth (BAZ) and distance (DIST) from the event. Stacked waveforms are labeled with the number of original waveforms included in the stacked trace. The Moho phase is clear at about 4 s. The shifting of the direct P-wave arrival indicates a thick low-velocity sediment layer near the surface.

shifting is due to dipping structure, then there are azimuthal variations in the shifting. However, the receiver functions for CLSB show the late arrival for all back azimuths (Figure 5.6), which means it is caused by a low-velocity surface layer. This is consistent with the description from the nearby well logs.

The model for CLSB uses the same six layers as SULB: top sediments, volcanics, upper, middle, lower crust, and mantle. All layers are assumed to be horizontal since there is no significant dipping evidence while SULB has the dipping structure. The top two layers have narrow boundaries for the thickness: minimum of 1.5 km, and maximum of 2 km, based on the well description.

Given the similarities between the observed waveforms, I developed a CLSB model (Figure 5.7) by inverting a single high-quality stacked receiver function (45° distance and a back azimuth of 133°, upper left Figure 5.6). Although the model is produced by one waveform, synthetic waveforms generated by this model provide a very good match at all other azimuths and distances (Figure 5.8).

The main features of the crust are similar to SULB, but with larger velocity contrasts. CLSB also has a low velocity sedimentary layer at the surface, a thin high-velocity layer beneath it (likely volcanic cover), and also a low velocity zone above the Moho (like SULB). The Moho Ps conversion is at about 4 seconds, which is slightly earlier than SULB Moho Ps. This Moho Ps timing suggests that the Moho is shallower under CLSB compared to SULB. This is consistent with the models that have a Moho at 29 km depth at CLSB and 36 km depth at SULB. The high amplitude of the peaks for the Moho conversion implies a larger Vs contrast, and the trough before it corresponds to a low velocity zone above the Moho discontinuity.

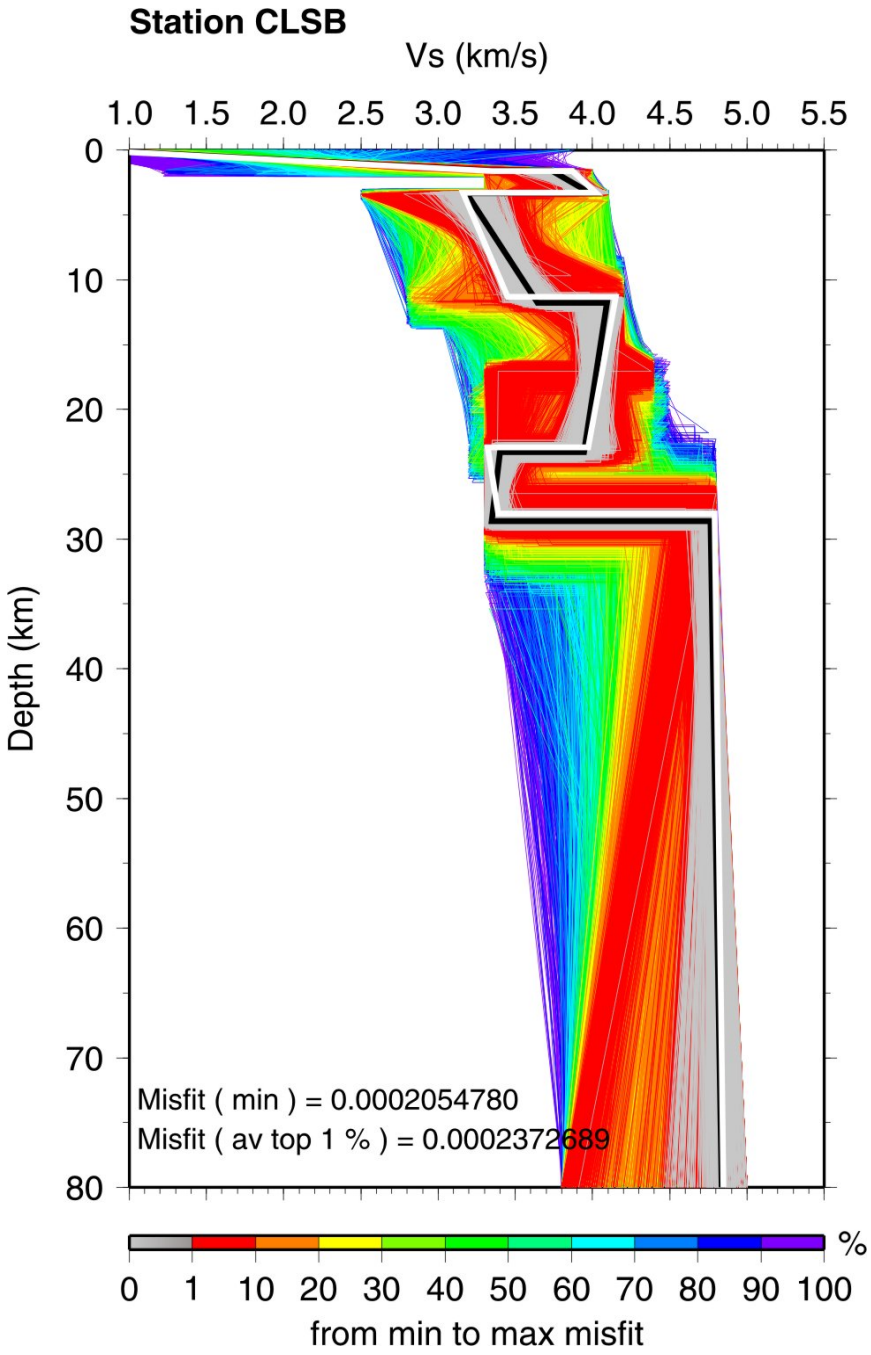

Figure 5.7 S-wave velocity model of CLSB, in terms of a density plot of the 2000 best-fitting models generated by the NA. The best-fitting model is plotted in white, and the average model computed from the 1% of models with the lowest misfit is plotted in black. The misfit of the best-fitting model and top average 1% models are given. The rainbow colour scale shows decreasing misfit, from purple to red and grey.

The first layer of the Earth model for CLSB (Figure 5.7) is 1.6 km thick and has a Vs ranging from 0.8 km/s at the top to 3.4 km/s at the bottom. This strong gradient results from the extremely low velocity surface sediments. The second layer of volcanic cover is 2.3 km thick with the top velocity of 3.8 km/s and bottom of 4.0 km/s. Layer thicknesses of 8.0 km, 11.1 km, 5.1 km were determined for the upper, middle, and lower crust respectively, with an average Vs of 3.3 km/s for the upper and lower crust, 3.9 km/s for the middle crust.

Since the model is generated by inverting one receiver function (back azimuth 133°), the synthetics show the best fit for this waveform. The more distant events (Δ = 60°-100°) from the similar direction, southeast, also show a slightly better fit than the ones from the other directions (Figure 5.8).

Even though a = 2 receiver functions resolves primary crustal features than a = 5 receiver functions as mentioned above, they still have enough resolution to generate thin near-surface sedimentary and volcanic layers. To prove this, a receiver function generated by a simple model (Figure 5.9) is presented below. The receiver function in black is the same as input for the model in Figure 5.7 (left top), and the synthetic receiver function in red is generated by a modified model from Figure 5.7, by removing the volcanic layer. Since removing only a thin layer completely changes the synthetic waveform, it proves that a = 2 receiver functions are capable of resolving the thin volcanic layer.

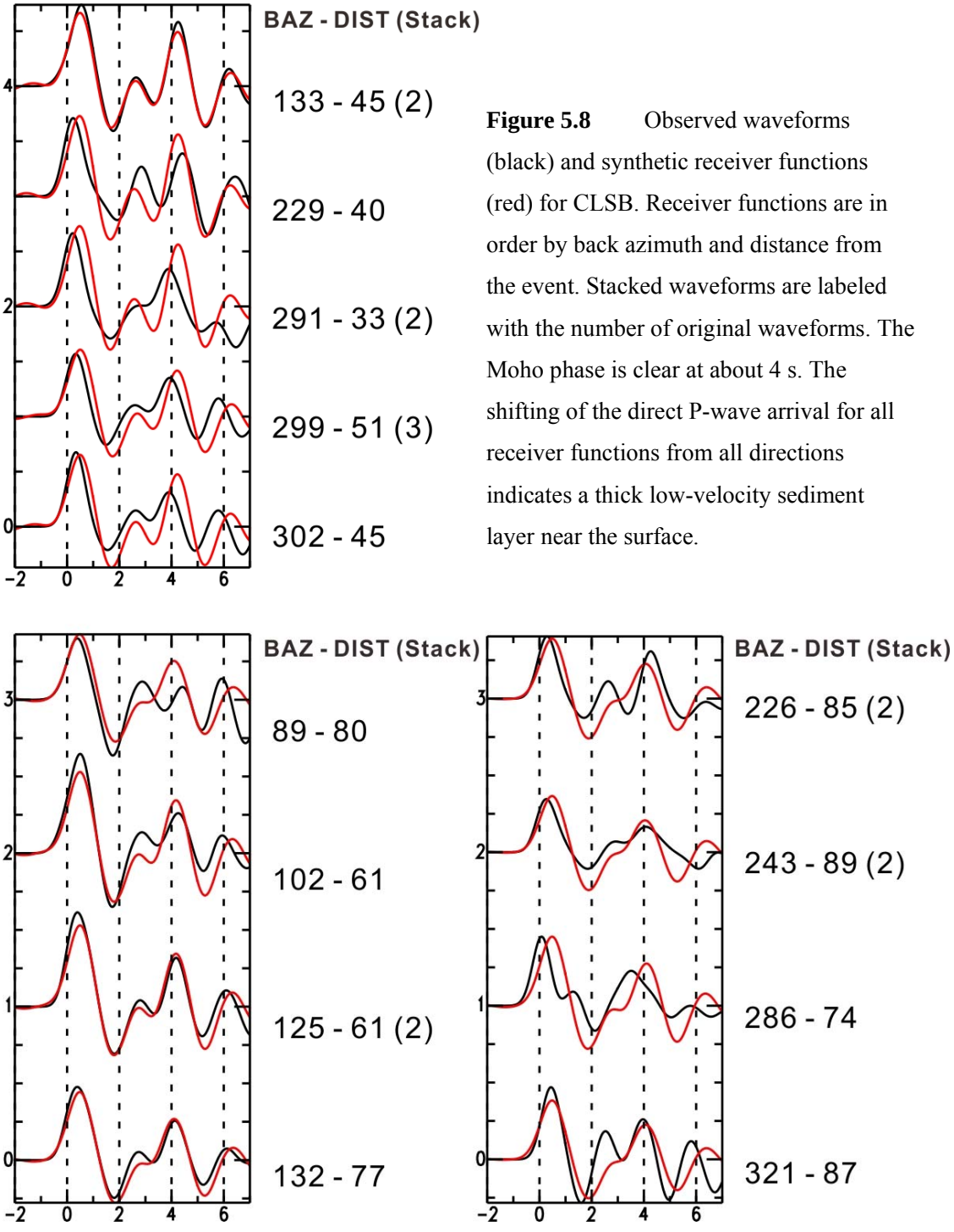

Figure 5.8 Observed waveforms (black) and synthetic receiver functions (red) for CLSB. Receiver functions are in order by back azimuth and distance from the event. Stacked waveforms are labeled with the number of original waveforms. The Moho phase is clear at about 4 s. The shifting of the direct P-wave arrival for all receiver functions from all directions indicates a thick low-velocity sediment layer near the surface.

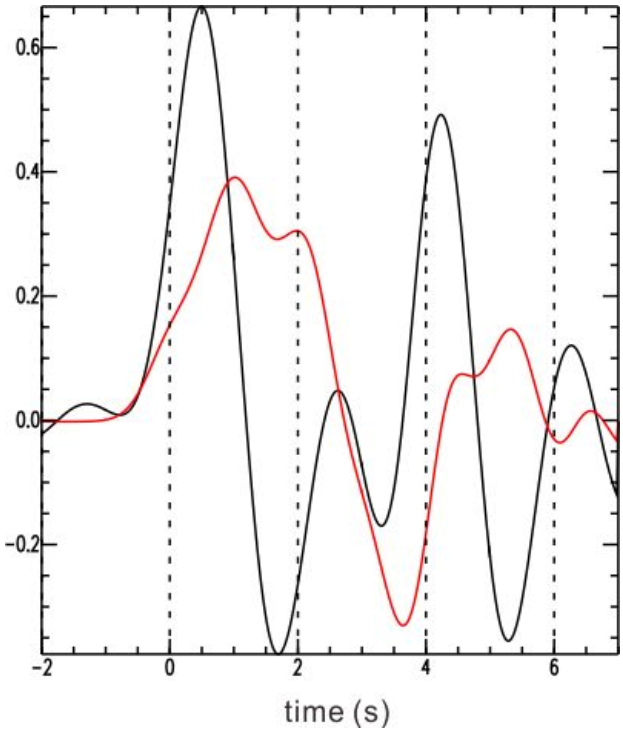

Figure 5.9 Observed receiver function (black) has the back azimuth of 133˚ and distance of 45˚ (Stacked by two receiver functions). Synthetic receiver function (red) is generated by a model (Figure 5.7) without the volcanic layer.

2.3 THMB

THMB is located in the central part of the Nechako Basin (52.5489 N, 124.1323W, elevation 1.126 km), which is about 50 km away from Nazko cone to the southwest. Unlike stations SULB and CLSB, this station has more information from previous geophysical studies. THMB is close to well b-22-K, about 5 km to the west, and is in the study area of first-arrival tomographic inversion (block C) (Figure 2.1; Hayward and Calvert, 2008). The results from first-arrival tomographic inversion provide some information on the velocity of the very shallow structure (to a maximum depth of about

1.5 km), and the well description and sonic log of b-22-K show the near surface structure clearly, up to the 4 km depth.

THMB is deployed on the Eocene volcanic and sediments of the Ootsa Lake and Chilcotin Groups. Chilcotin Group basaltic rocks are overlying shale, siltstone and minor volcanic rocks of Ootsa Lake Group. The information from well b-22-K suggests the existence of about 0.45 km thick volcanics on the top, with 2 km of sedimentary rocks, and another volcanic layer below it. The lowest Vs is about 1.0 km/s in the uppermost 100 m below the surface, but the general Vs near the surface is about 2.2 km/s. The average Vs for the bottom volcanic layer at about 3 km depth is 3.2 km/s.

The initial model for THMB was generated by a single receiver function (distance 50°, back azimuth 300°, 4 stacked receiver functions) with 6 horizontal layers as for stations SULB and CLSB. The top layer of this model shows a large Vs gradient from 2.3 km/s to 3.7 km/s over a thickness of 2.7 km. The second layer has a very high velocity of 4.1 km/s and a thickness of 1.4 km, which would be considered as the volcanic layer. Beneath this high velocity layer, there are three crustal layers with an average Vs of 3.5 km/s. In addition, the Moho shows a large Vs contrast from 3.2 km/s to 4.4 km/s at 34.8 km depth.

The receiver functions for THMB indicate the existence of a dipping structure by azimuthally-varying time delays of the direct P-wave arrivals as explained in the previous chapter. For THMB, the receiver functions with southeast and southwest back azimuths have significant time delays of the direct P-wave arrivals (Figure 5.10). The dip direction of the near surface structure was determined through forward modeling as south (strike 90°), which is similar to SULB.

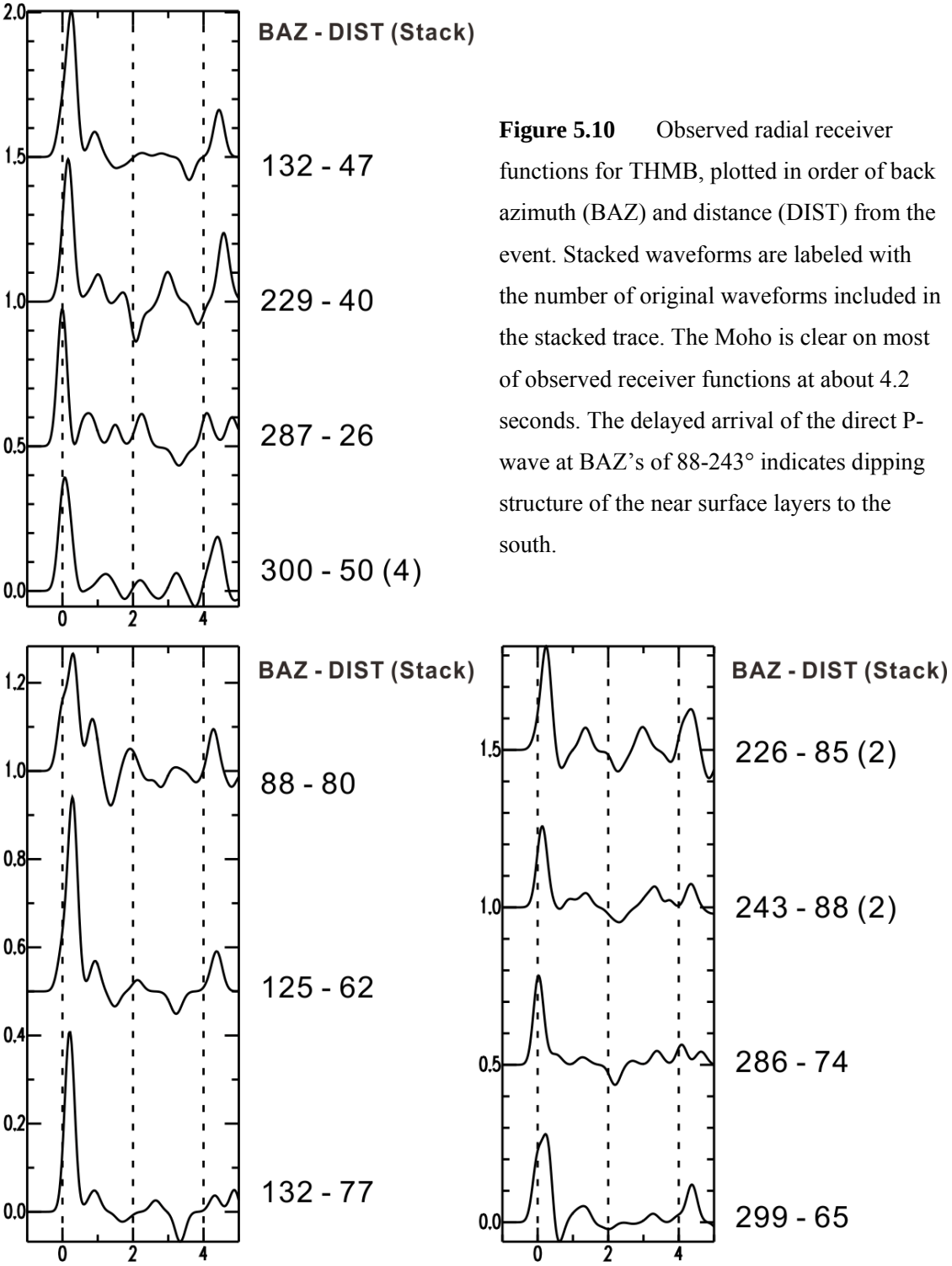

Figure 5.10 Observed radial receiver functions for THMB, plotted in order of back azimuth (BAZ) and distance (DIST) from the event. Stacked waveforms are labeled with the number of original waveforms included in the stacked trace. The Moho is clear on most of observed receiver functions at about 4.2 seconds. The delayed arrival of the direct P-wave at BAZ's of 88-243° indicates dipping structure of the near surface layers to the south.

The inversion code used in this study does not allow for both a gradient and dipping structure for the same layer. If the layer is dipping, it is forced to have a constant Vs through the whole layer. Since THMB clearly has dipping structure for at least the top two layers (which also likely have a large gradient - especially the surface layer), they are divided into five sub-layers: the top layer into three, and the second layer into two. Each of these sub-layers is 0.8 km thick, and dipping at 20° to the south. Vs for the top four sub-layers increases from 2.3 km/s to 4.0 km/s gradually, and then Vs for the fifth layer decreases to 3.7 km/s (Figure 5.11). Because the top layers are not allowed to change, the model modified from the initial model is generated by only 500 iterations for the minimum misfit. The layers for upper, middle, lower crust and mantle have relatively broad boundaries.

The main crustal layers do not vary much from the initial model according to the prior information, with an average S-wave velocity of about 3.5 km/s. The thicknesses of the upper, middle, and lower crust are 9 km, 11.5 km, and 9.3 km, respectively (Figure 5.11). The arrival at about 4.2 seconds is produced by the Moho, at the 34.8 km depth, similar to that at SULB. SULB and THMB are located along about the same longitude, separated by about 80 km. Since geological differences in this basin are predominately east-west, SULB and THMB generally have more similar crustal structure to each other than to CLSB, such as the dip direction and the Moho depth. The trough before the Moho arrival for THMB is created by the low velocity zone at the bottom of the crust (Figure 5.10 and Figure 5.12). The high amplitude of this arrival indicates a sharp Moho with large Vs contrast; however, the low velocity layer makes this contrast even larger. The S-wave velocity at the bottom of the lower crustal layer is 3.58 km/s, and upper most mantle is 4.80 km/s; resulting a Vs contrast of about 1.3 km/s across the Moho.

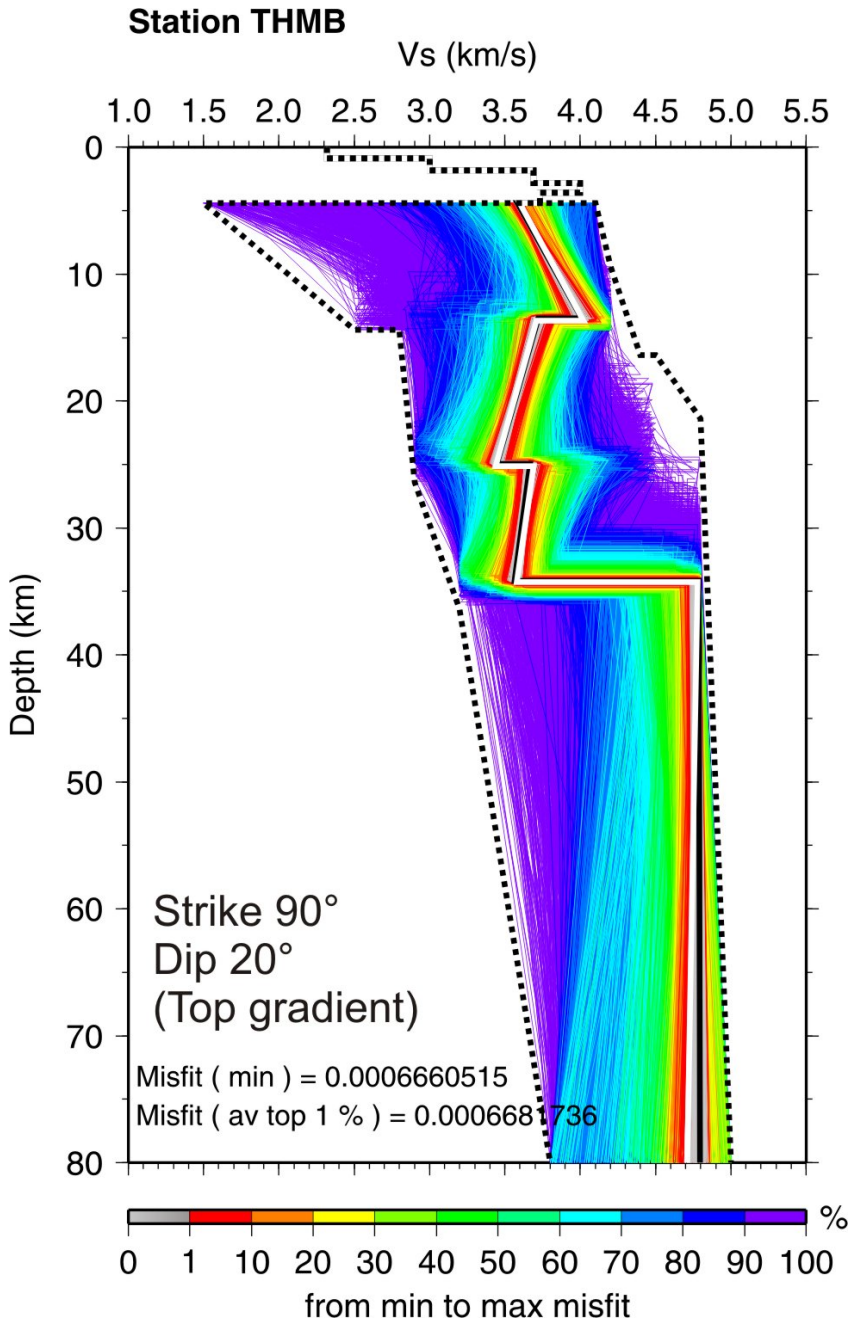

Figure 5.11 S-wave velocity model of THMB, in terms of a density plot of the 500 best-fitting models generated by the NA. The best-fitting model is plotted in white, and the average model computed from the 1% of models with the lowest misfit is plotted in black. The misfit of the best-fitting model and top average 1% models are given. The rainbow colour scale shows decreasing misfit, from purple to red and grey. The velocity structure of the top five layers to a depth of 5 km is fixed (based largely on borehole data) and dipping at an angle of 20° with strike of 90° for all top 5 layers.

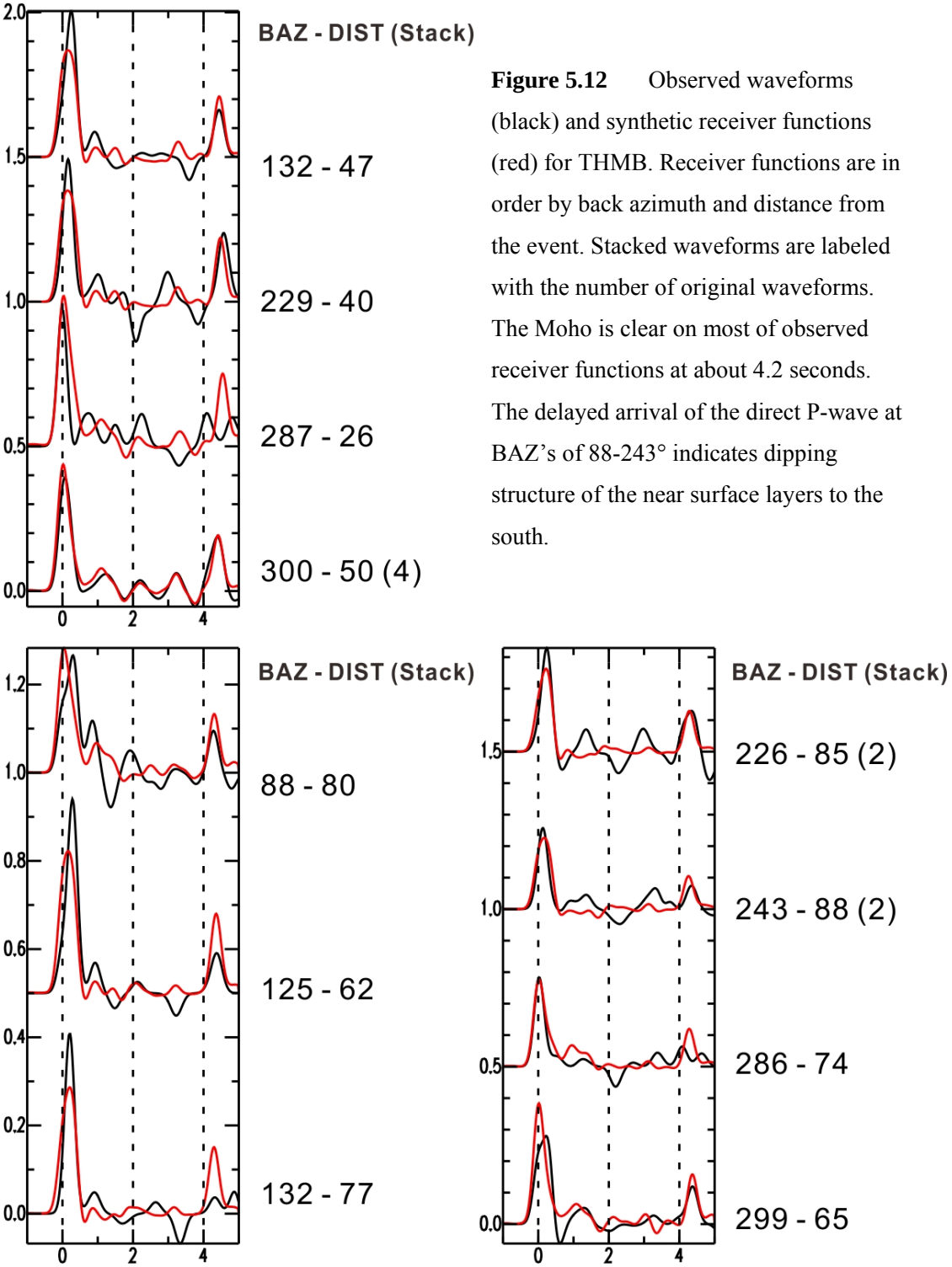

Figure 5.12 Observed waveforms (black) and synthetic receiver functions (red) for THMB. Receiver functions are in order by back azimuth and distance from the event. Stacked waveforms are labeled with the number of original waveforms. The Moho is clear on most of observed receiver functions at about 4.2 seconds. The delayed arrival of the direct P-wave at BAZ's of 88-243° indicates dipping structure of the near surface layers to the south.

5.4 ALRB

ALRB, the western-most station of the POLARIS Nechako array, is located near Anahim Lake, BC (latitude 52.5103 N, longitude 125.0844 W, elevation 1.237 km). This station does not have any usable information from the previous geophysical studies or bore holes. It may not have been included in previous studies because it is located on the western margin of the Nechako basin while most studies focused on the center of the basin. The only study which went through this region is the BATHOLITH project (Zandt, 2009); however, the result from BATHOLITH illustrates structure to the west of it and primarily shows a Moho depth of about 33 km.

The initial attempts at modeling ALRB data utilized high frequency ($a = 5$) receiver functions. The first arrival is complicated and comprised of two or three peaks rather than simple single peak observed at other stations (SULB or THMB), and the amplitudes of these peaks vary strongly with back azimuth. However, it is impossible to construct a crustal model with only six or seven horizontal layers that reproduce the complicated high-frequency peaks in the observed receiver functions. Thus, it becomes necessary to generate models with the low frequency ($a = 2$) receiver functions for this station (Figure 5.13).

One of the valid models for ALRB is generated by inverting a single low frequency receiver function (distance 48°, back azimuth 300° - see the 4th waveform on the left column in Figure 5.13 and Figure 5.15). As all observed receiver functions have similar phase shift for the direct P-wave arrival, regardless of back azimuth, the crustal structure must have near-surface low velocity sediments. For this reason, minimum Vs of 0.5 km/s was utilized for the top two layers. Otherwise, the starting model is similar to

the initial model for the previous stations: 6 horizontal layers of near-surface sediments, volcanic layer, upper crust, middle crust, lower crust, and the upper mantle.

The Vs for the shallowest layer decreases from 1.5 km/s to 1.2 km/s over the 0.9 km layer. This layer may represent Quaternary deposits on the surface, according to the geological map of Ferri and Riddell (2006). The second layer, which is generally expected to be the volcanic cover, has a Vs increasing from 2.2 km/s to 3.8 km/s at a depth of 3.7 km. This large gradient may be made due to a change from sediments to the high velocity volcanics.

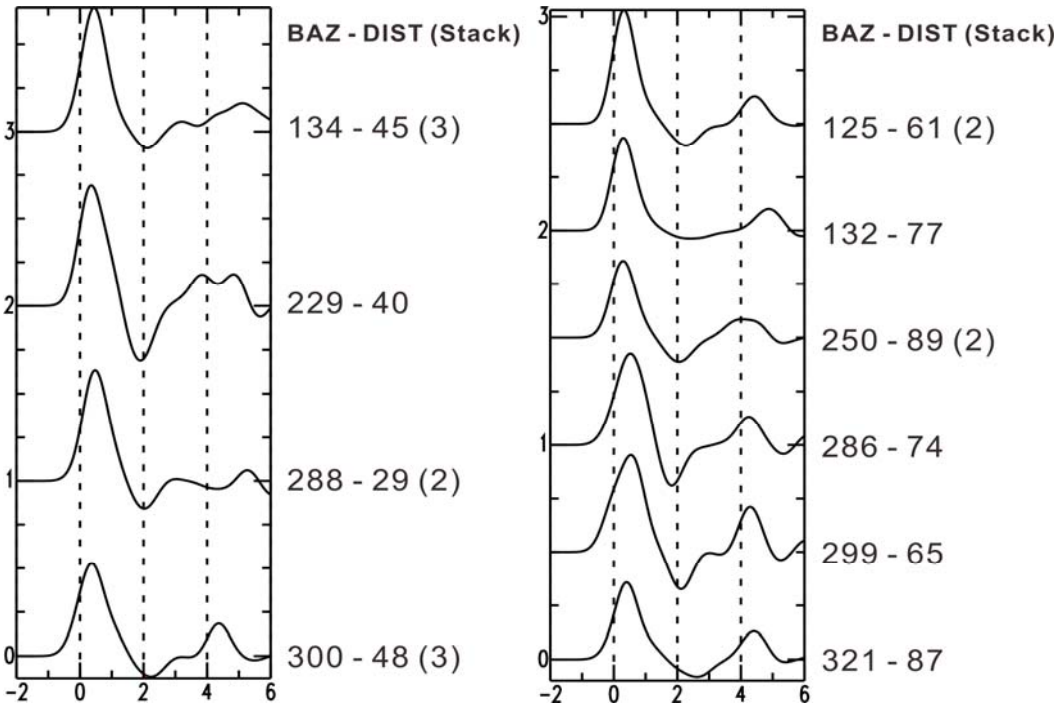

Figure 5.13 Observed radial receiver functions for ALRB, plotted in order of back azimuth (BAZ) and distance (DIST) from the event. Stacked waveforms are labeled with the number of original waveforms included in the stacked trace. The Moho Ps is at about 4.1 s, but some of these arrivals from the south cannot be clearly distinguished. All waveforms show the similar time delay of the direct P-wave arrival which indicates a near-surface thick sediment layer with low S-wave velocity.

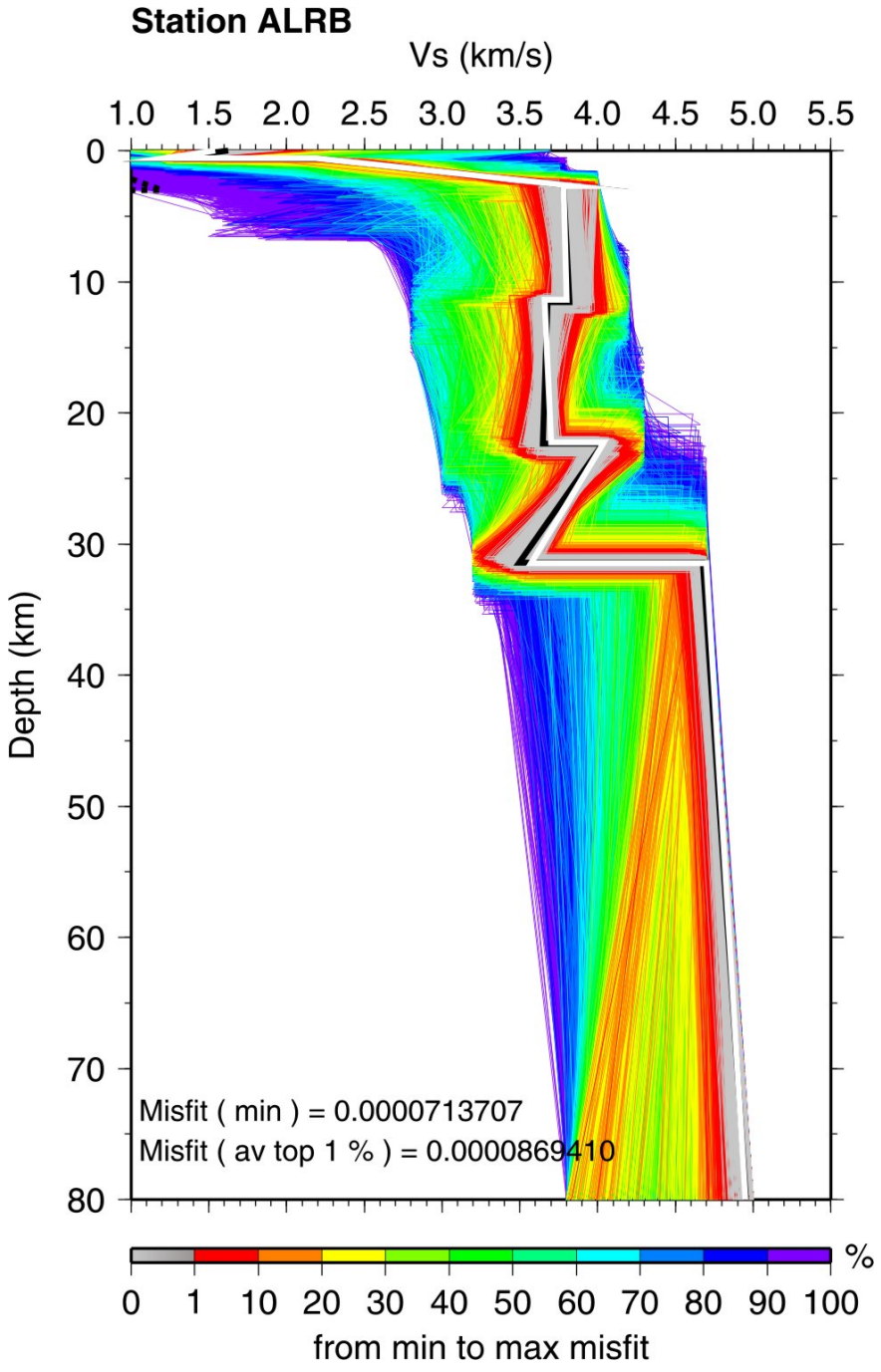

Figure 5.14 S-wave velocity model of ALRB, in terms of a density plot of the 2000 best-fitting models generated by the NA. The best-fitting model is plotted in white, and the average model computed from the 1% of models with the lowest misfit is plotted in black. The misfit of the best-fitting model and top average 1% models are given. The rainbow colour scale shows decreasing misfit, from purple to red and grey. Third and fourth layers (upper and middle crusts) can be merged together.

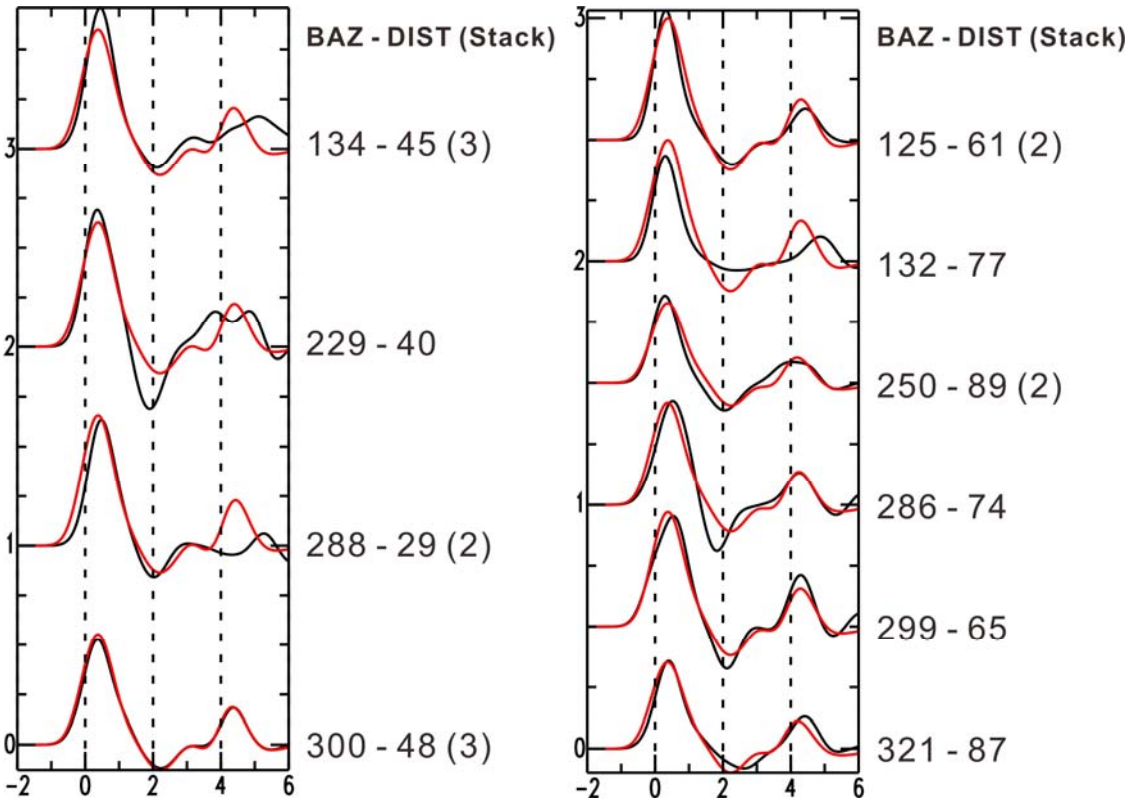

Figure 5.15 Low frequency (a = 2) observed (black) and synthetic receiver functions (red) for ALRB. Receiver functions are in order by back azimuth (BAZ) and distance (DIST) from the event. Stacked waveforms are labeled with the number of original waveforms included in the stack. The Moho Ps is at about 4.1 s, but some of these arrivals from the south cannot be clearly distinguished. All waveforms show the time delay of the direct P-wave arrival which indicates a near-surface thick sediment layer with low S-wave velocity.

The upper and middle crusts are 9 km and 10.5 km thick, respectively, with an average S-wave velocity of 3.7 km/s. Although the middle crust has a lower Vs than the upper crust, the difference is only about 0.1 km/s without gradients. Therefore, it is not critical to divide the upper and mid crust, and merging them into single layer does not change the data misfit. The model for ALRB also includes a low velocity zone above the Moho, as at all previous stations. The S-wave velocity for this zone is as low as 3.5 km/s at the bottom of the lower crust.

In general, predicting some of the main features, such as the Moho depth, by examining the observed receiver functions is the first step in order to construct the Earth model. However, some observed receiver functions at ALRB do not clearly show the Moho phase - especially the closer events (Δ=30-60°), even though the model (Figure 5.14) has a sharp Moho with large Vs contrast (1.1 km/s) at 31.5 km depth. Therefore, having an unclear or smaller Moho phase for ALRB may be related to deconstructive phases from multiples.

The model shown in Figure 5.14 has a much smaller misfit match than the second model presented below (Figure 5.16) particularly for back azimuths of 280-300°. A second model for ALRB was obtained by inverting three receiver functions simultaneously with back azimuths of 125-135°, i.e., in the opposite direction to the previous case. This model is based on the first model shown in Figure 5.14 in that the top two layers are fixed to the same values because the first direct P-wave arrivals are similar in all receiver functions. Also, the same parameterization is applied for the second model. Since these two layers are fixed, only 500 iterations are required to minimize the misfit function.

The upper and middle crust of the second model (Figure 5.16) do not vary much from the first model (Figure 5.14), with about the same thickness and mean velocity for each layer. The main difference between the two models is the lower crust and Moho. The velocity for the lower crust changes from 3.6 km/s to 4.1 km/s; this makes the Moho contrast smaller because the Vs at the top of the mantle stays approximately the same (4.7 km/s). Not only does Vs change, but also the depth of Moho changes, becoming 3.4 km deeper compared to the first model as the thickness of the lower crust increases. The

deeper Moho is predictable for the second model because the Moho phase in the input (SE) receiver functions arrives at about 4.8-5 s compared to the 4.1 s for the first model (developed for the NW). The Moho depth variation with back azimuth may be real, since ALRB is located at the edge of the Nechako basin. The inner side of the basin has deeper Moho (~35 km) like other inside stations, but since it is close to the edge, the Moho depth may become shallower (~31.5 km) outward.

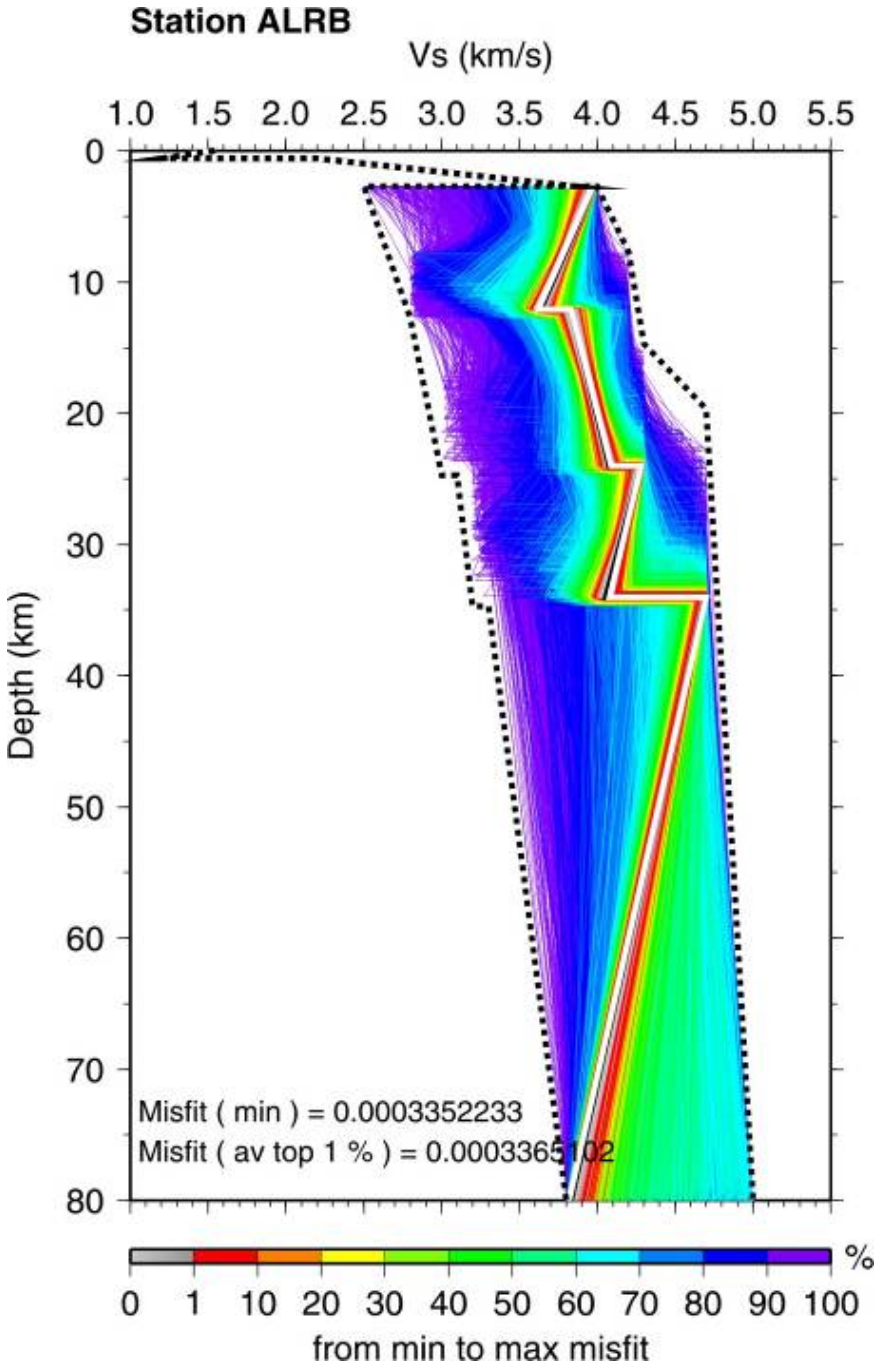

Figure 5.16 S-wave velocity model of ALRB, in terms of a density plot of the 500 best-fitting models generated by the NA. The best-fitting model is plotted in white, and the average model computed from the 1% of models with the lowest misfit is plotted in black. The misfit of the best-fitting model and top average 1% models are given. The rainbow colour scale shows decreasing misfit, from purple to red and grey. The velocity structure of the top two layers is fixed (based on the first model in Figure 5.14).

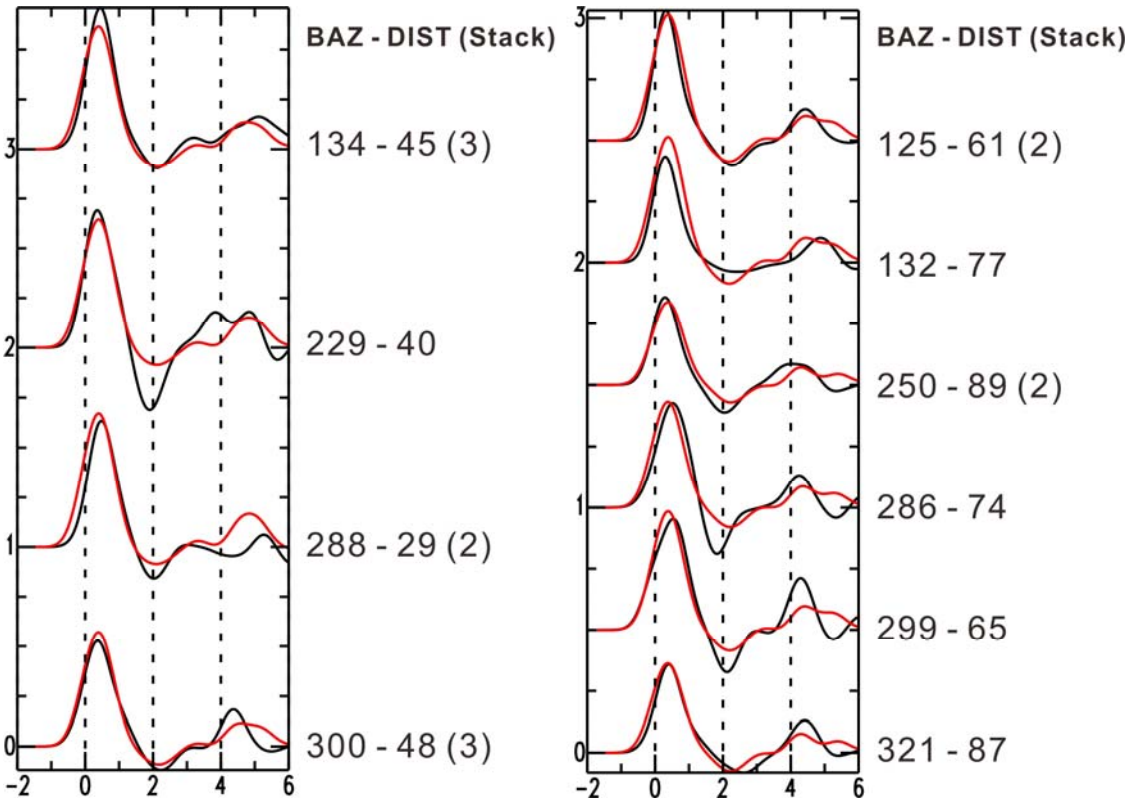

Figure 5.17 Low frequency (a = 2) observed (black) and synthetic receiver functions (red) for ALRB. Receiver functions are in order by back azimuth (BAZ) and distance (DIST) from the event. Stacked waveforms are labeled with the number of original waveforms included in the stack. The Moho Ps is at about 4.1 s, but some of them from south direction are not clear to distinguish. All waveforms show the time delay of the direct P-wave arrival which indicates a near-surface thick sediment layer with low S-wave velocity.

5.5 TALB

Station TALB is located in the southwest region of the basin in the western Redstone area, near Tatla Lake (52.0147 N, 124.2536 W, elevation 1.127 km). Like ALRB, TALB has no relevant geophysical constraints from previous studies. The closest boreholes (c-75-A and d-94-G) are about 65-70 km away from the station, and TALB is also about the same distance from the closest MT study lines (Profile F, Spratt and

Craven, by personal communication, 2009). Block B of the study area of first-arrival tomographic inversion that includes a single seismic line is about 40 km from TALB. Also, the result from block B was not presented because it may be unable to be modeled by the 2-D tomographic methods or not modeled yet (Howard and Calvert, 2010).

In the previous section for ALRB, the high frequency (a = 5) receiver functions were too complicated to construct an Earth model beneath the station, but low frequency receiver functions were adequate to recover the main features of the crust. The observed TALB receiver functions are even more complicated than those for ALRB. In my initial modeling I considered the low frequency (a = 2) receiver functions. However, this did not work for TALB due to the unusual ringing-like shape of the observed receiver functions. The inversion code recognized the ringing peaks as the Moho arrival, and considered the correct Moho arrival to be the multiple from other discontinuities in the shallow structure. Hence, the use of a = 5 receiver function (Figure 5.18) was critical for TALB although the model could not create the synthetics with small misfits.

Similar to ALRB, the first phase of the observed receiver functions calculated for TALB consists of complex triple or quadric peaks due to the multiples from the thick low velocity sediment layer. According to this information, Vs boundaries for the surface layer of the model were set at 0.5 km/s as the minimum and 1.0 km/s as the maximum. Moreover, the thickness of the top layer was allowed to vary between 1 km and 3 km.

The crustal model underneath TALB is constructed from a single receiver function (Figure 5.18, distance 50°, back azimuth 299°, 5 receiver function stack) which contains the greatest number of waveforms. It is not possible to obtain one best solution

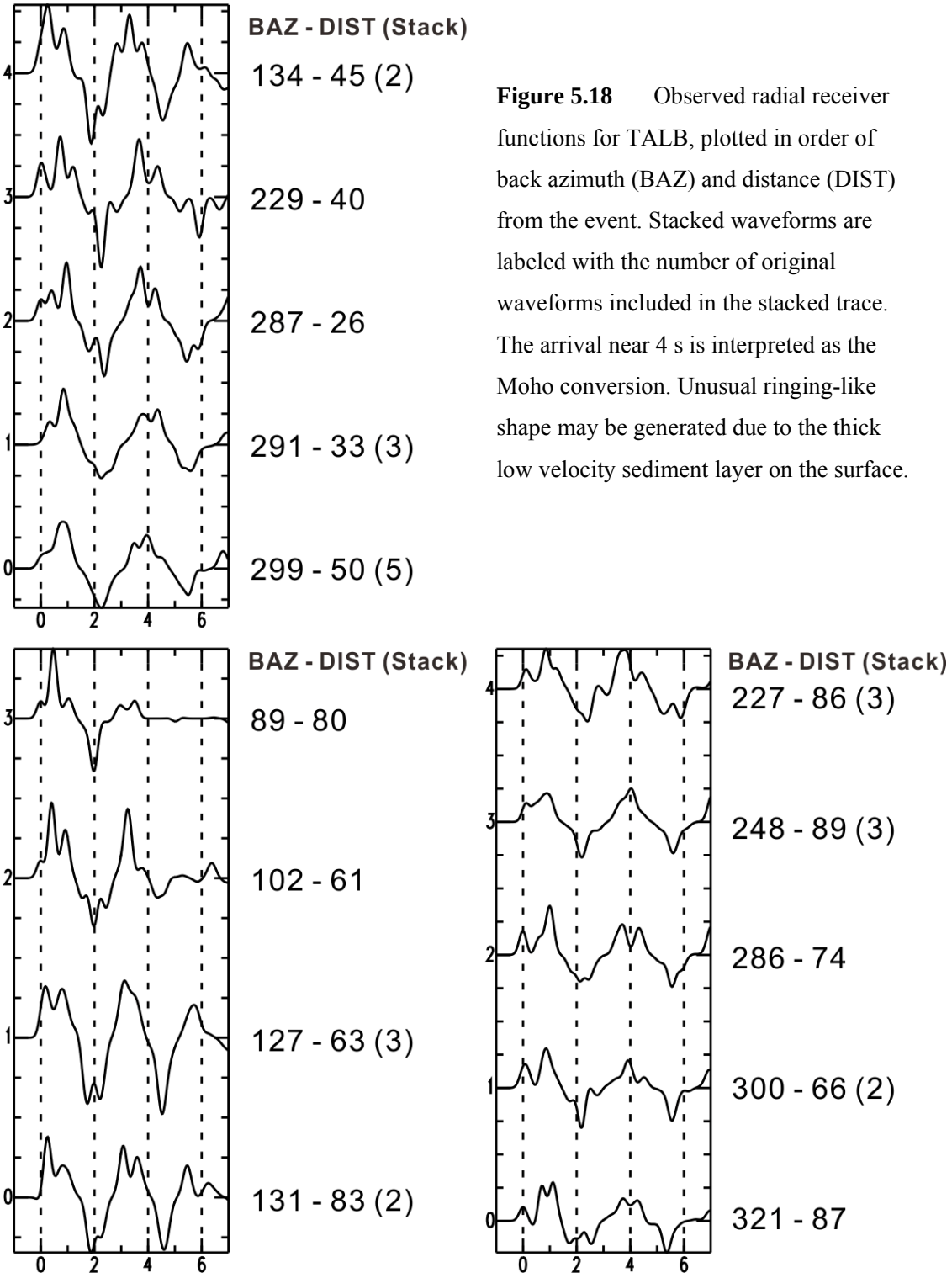

Figure 5.18 Observed radial receiver functions for TALB, plotted in order of back azimuth (BAZ) and distance (DIST) from the event. Stacked waveforms are labeled with the number of original waveforms included in the stacked trace. The arrival near 4 s is interpreted as the Moho conversion. Unusual ringing-like shape may be generated due to the thick low velocity sediment layer on the surface.

fitting all receiver functions at this station because the observed receiver functions vary significantly with back azimuth, and have too complicated phase patterns to be modeled.

The model parameterization for TALB is the same as at most other stations with 6 horizontal layers, except for the low minimum boundary of S-wave velocity for the top layer as explained above. In inversion result is shown in Figure 5.18. Vs of the first layer starts from 0.8 km/s at the surface, and then gradually increases to 1.8 km/s at 1.1 km depth. Vs in the second layer changes from 1.9 km/s to 3.9 km/s. This type of near-surface structure is common in the Nechako basin, with low velocity surface sediments above the high velocity volcanic layer.

While the near-surface structure for TALB is predictable as explained above, the upper, middle, and lower crust layers are less obvious than at other stations. The mean S-wave velocity is about 3.3 km/s whereas others are about 3.5-3.7 km/s. The lower crust has the low velocity zone that has been generally observed for most areas in the Nechako basin, but at this site, the middle crust has a very low Vs of 2.8 km/s. Forward modeling shows that it is possible to merge the middle and lower crust into one low velocity zone with a large gradient. The most extraordinary feature in the model of TALB is the Moho depth. The Moho phase arrives at about 4 s, which is similar to CLSB, but the Moho is located at a much shallower depth: 29 km for CLSB, but 22.4 km for TALB. The very shallow Moho at this site may be real, but this does not follow the common characteristics of the crustal structure in the basin.

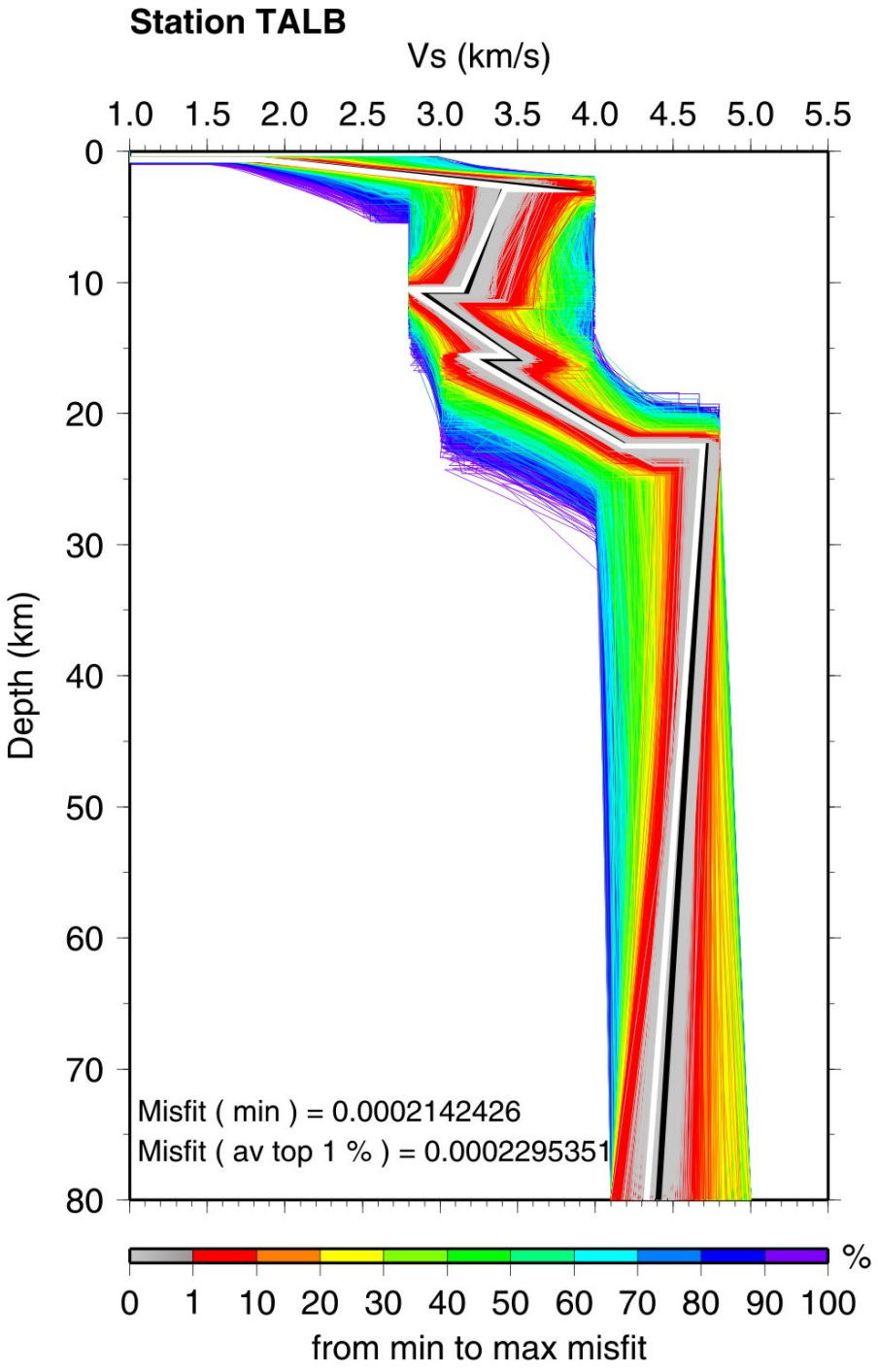

Figure 5.19 S-wave velocity model of TALB, in terms of a density plot of the 500 best-fitting models generated by the NA. The best-fitting model is plotted in white, and the average model computed from the 1% of models with the lowest misfit is plotted in black. The misfit of the best-fitting model and top average 1% models are given. The rainbow colour scale shows decreasing misfit, from purple to red and grey.

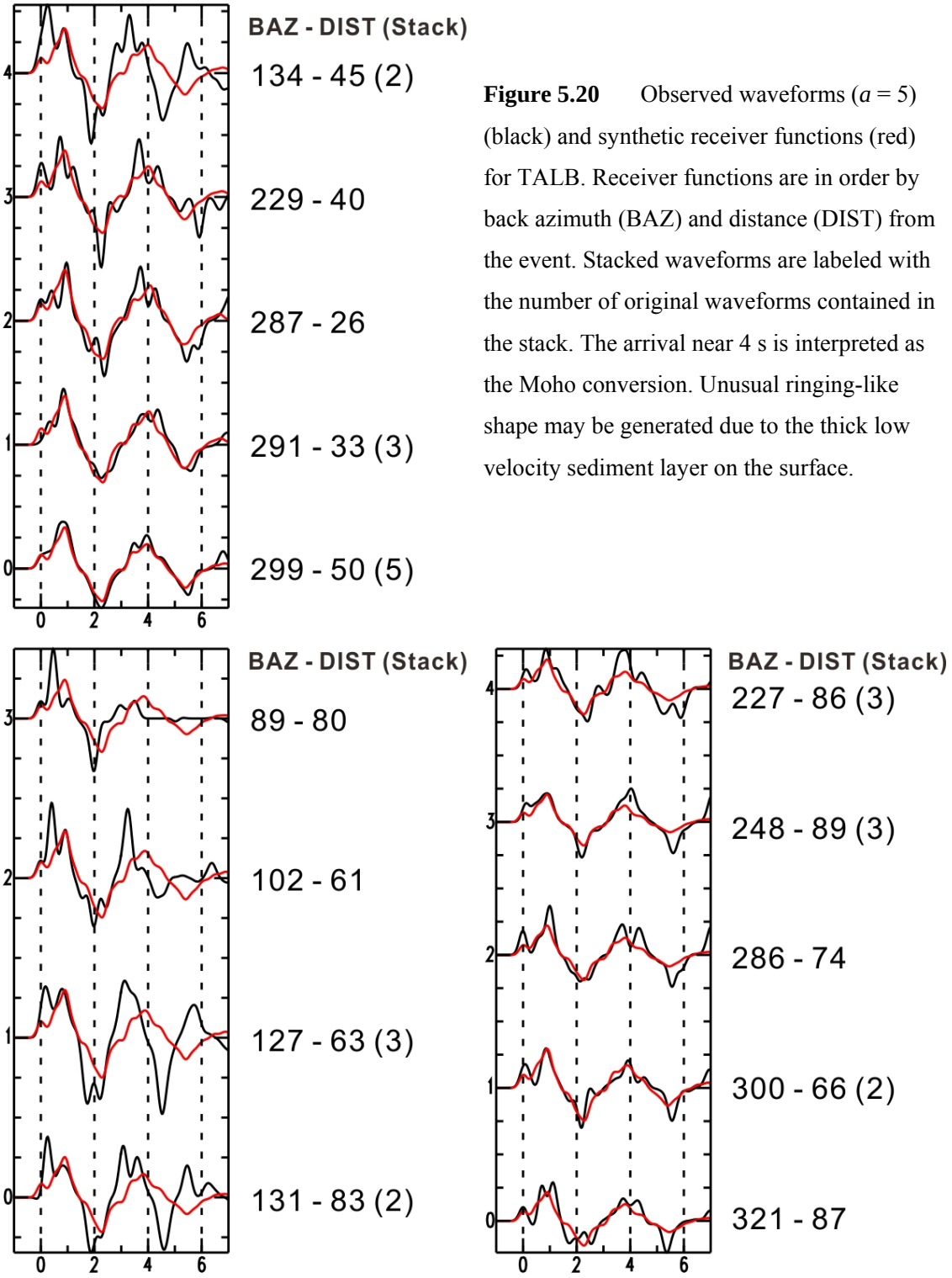

Figure 5.20 Observed waveforms (a = 5) (black) and synthetic receiver functions (red) for TALB. Receiver functions are in order by back azimuth (BAZ) and distance (DIST) from the event. Stacked waveforms are labeled with the number of original waveforms contained in the stack. The arrival near 4 s is interpreted as the Moho conversion. Unusual ringing-like shape may be generated due to the thick low velocity sediment layer on the surface.

The model shown in Figure 5.19 generates synthetics (Figure 5.20) that have a minimum misfit for the northwest direction, but not for the opposite direction, 125-140°. The arrivals in the observed receiver functions from the southeast appear earlier, with the the Moho arrival coming in about 0.5 s earlier. However, this compressing-like effect for the southeast direction is likely due to thicker sediments on the surface rather than representing evidence of shallower discontinuities. According to forward modeling, the arrival time of each peak in the southeastern receiver functions matches synthetics for a model with about 5 km thick sediments on the surface. Therefore, the thickness of sediments on the surface near TALB may vary along the back azimuths: about 5 km thick to the southeast and 1 km thick to the northwest. As a result of the thick sediment layer, TALB has abnormal ringing-like arrivals in all observed receiver functions which complicate the modeling process.

5.6 RAMB

RAMB is located in the Nazko area: about 40 km from the Nazko cone to the southeast (52.632 N, 123.1227 W, elevation 1.259 km). It is one of the central stations of the POLARIS array in the Nechako basin. There are several other geophysical studies in this region. Therefore, it is relatively straightforward to obtain information from previous (and ongoing) geophysical studies for better constraints of the inversion model. The area around RAMB includes 3 boreholes (a-4-L, b-96-E, b-16-J), the seismic lines 159-01 to 159-15 and 162-02 for the first-arrival tomographic inversion (Figure 2.1; Hayward and

Calvert, by personal communication, 2010). Profile B of MT study also goes through this area (Figure 2.5).

Among the wells near RAMB, b-16-J is the closest to the station: about 10 km to the northwest direction. According to the borehole data from b-16-J, the Eocene volcanic Endako Group is present from the surface to the depth of 0.6 km with a mean S-wave velocity of 2.2 km/s. Below the volcanics, the sediment layer, which may be Ootsa Lake Group consisting of conglomerate and sandstone, is about 0.3 km thick. However, two other boreholes (d-96-E and a-4-L) show only Cretaceous sediments (a mixture of conglomerate, sandstone, and shale) from the surface to 0.6 km depth with an average Vs of 1.6-1.8 km/s. This variation between boreholes may result from the two strike-slip faults between the boreholes and therefore different structures.

The MT study by Spratt and Craven (by personal communication, 2010) is ongoing near RAMB; the southern end of profile B is near the well a-4-L. The MT study indicates that the Cretaceous sediment layer on the surface (with lower resistivity) is about 2.5 km thick, a deeper and older volcanic layer is about 2 km thick, and Hazelton basement with higher resistivity is present beneath them.

According to the information above, the search bounds for the first sedimentary layer were set to 1.5-2.0 km/s for Vs and 1.5-3.0 km for layer thickness. For the second layer of the old volcanics, Vs was set to 2.8-3.8 km/s. The parameter bounds were set similar to those for the other stations except the top two layers.

The initial inversion for RAMB utilized only a single receiver function that contained the largest number of waveforms in the stack. However, the three receiver functions for the closest events (Δ=30-60°) showed significant variatioins with back

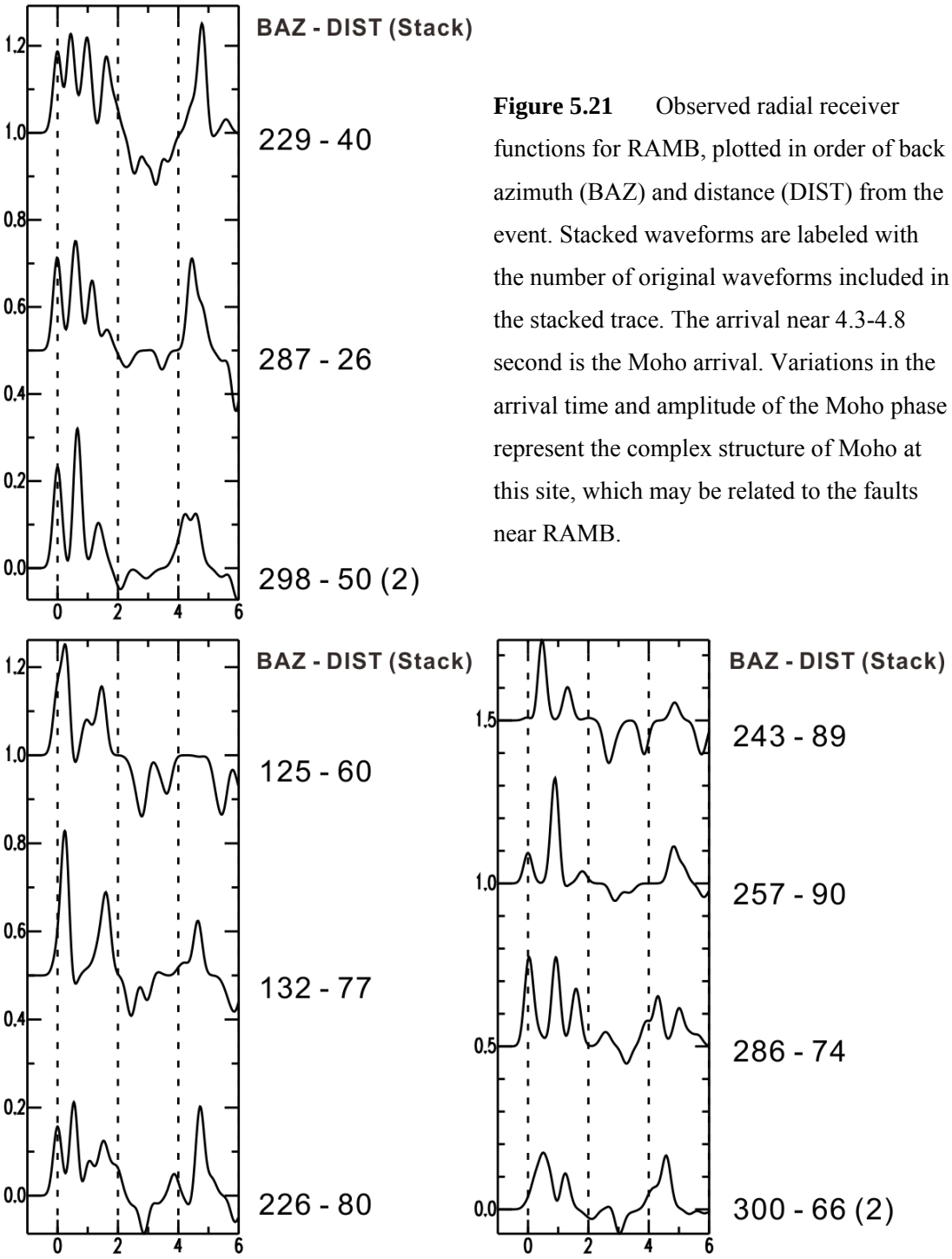

Figure 5.21 Observed radial receiver functions for RAMB, plotted in order of back azimuth (BAZ) and distance (DIST) from the event. Stacked waveforms are labeled with the number of original waveforms included in the stacked trace. The arrival near 4.3-4.8 second is the Moho arrival. Variations in the arrival time and amplitude of the Moho phase represent the complex structure of Moho at this site, which may be related to the faults near RAMB.

azimuth and cannot be explained by one model. Therefore, these three receiver functions (Figure 5.21 top left) were utilized simultaneously as input for the the next inversion

attempt. The starting model had six horizontal layers like most of the previous models. Although the misfit of the horizontal layer model was acceptable, I attempted a dipping layer for the first discontinuity because of some observations in the receiver functions – the time delay of the first peak for events from the southeast direction and the second, and third peaks in most receiver functions. This improved the misfit between observed and synthetics, especially for the arrivals in the first 2 seconds.

The final model for RAMB (Figure 5.22) has 6 layers with the first layer dipping 18.6° to the west with a strike of 162.6°. The first (sedimentary) layer has Vs = 1.8 km/s with a thickness of 1.8 km, and the second (volcanic) layer has Vs increasing from 2.8 km/s to 2.9 km/s over the 3.1 km thick layer. This result is consistent with the information from both the well log and MT study. However, I did a forward modeling study to investigate possible variation of Vs for the second layer. When Vs for the second layer is changed to 3.1-3.3 km/s with a gradient instead of 2.8-2.9 km/s as stated above, the amplitude of the second peak becomes higher which fits better with the observed receiver function. However, the trough at 2 s has a worse fit than the original.

Another modeled feature of interest at this station is the Moho depth. The top of Figure 5.21 and 5.23 shows receiver functions of RAMB within a distance range of 30-60°. The arrivals for the Moho are at 4.3-4.8 s in the plot. However, the amplitude and arrival time of the Moho phase is variable with back azimuth. The arrival comes later with higher amplitude for the event from southeast whereas the arrival comes earlier with smaller amplitude for the event from northwest. Along different back azimuths, the Moho arrival also changes into double peaks. This may be due to the faults in this region or to the variation of Moho depth along different directions near RAMB.

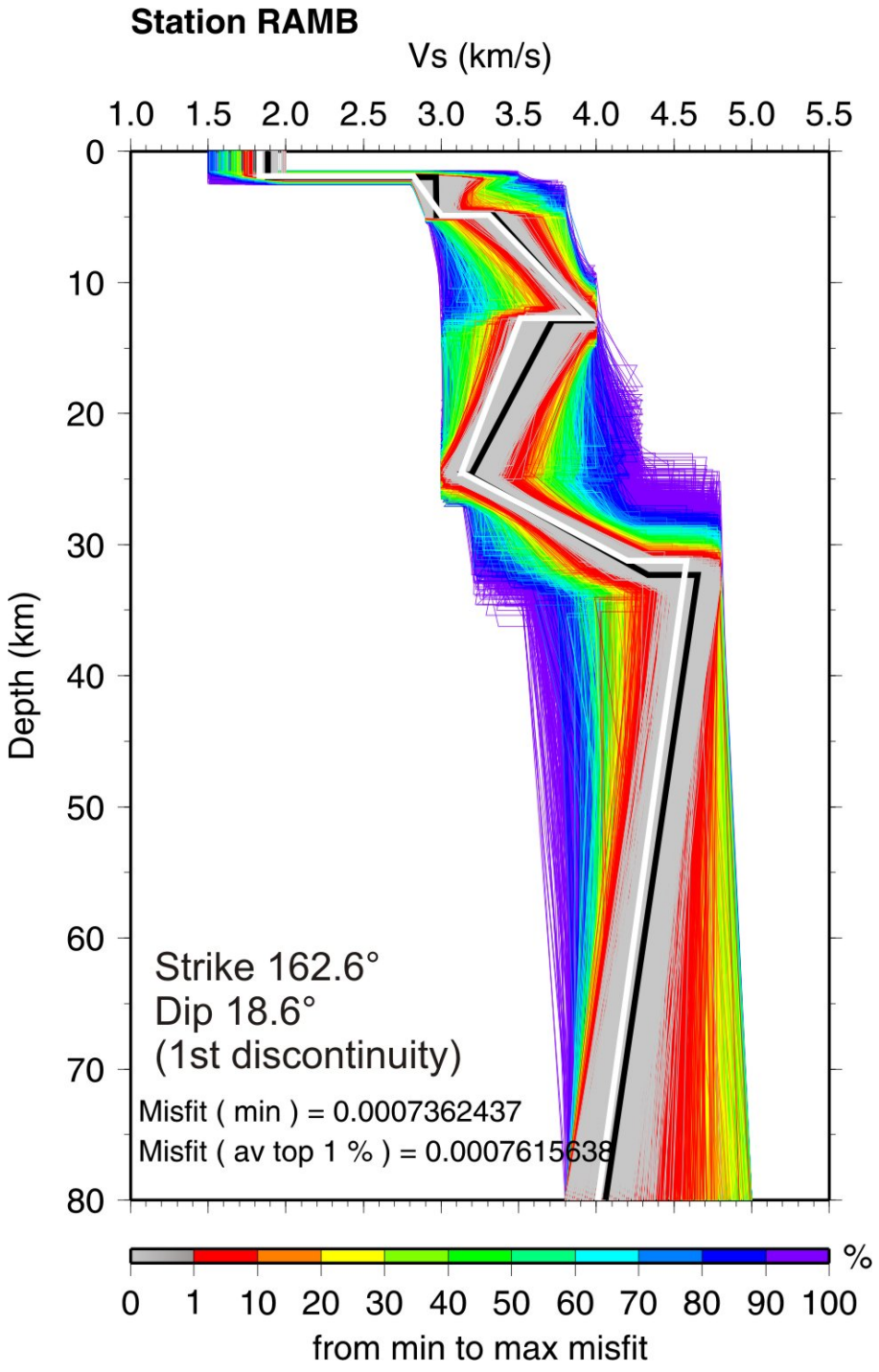

Figure 5.22 S-wave velocity model of RAMB, in terms of a density plot of the 1000 best-fitting models generated by the NA. The best-fitting model is plotted in white, and the average model computed from the 1% of models with the lowest misfit is plotted in black. The misfit of the best-fitting model and top average 1% models are given. The rainbow colour scale shows decreasing misfit, from purple to red and grey.

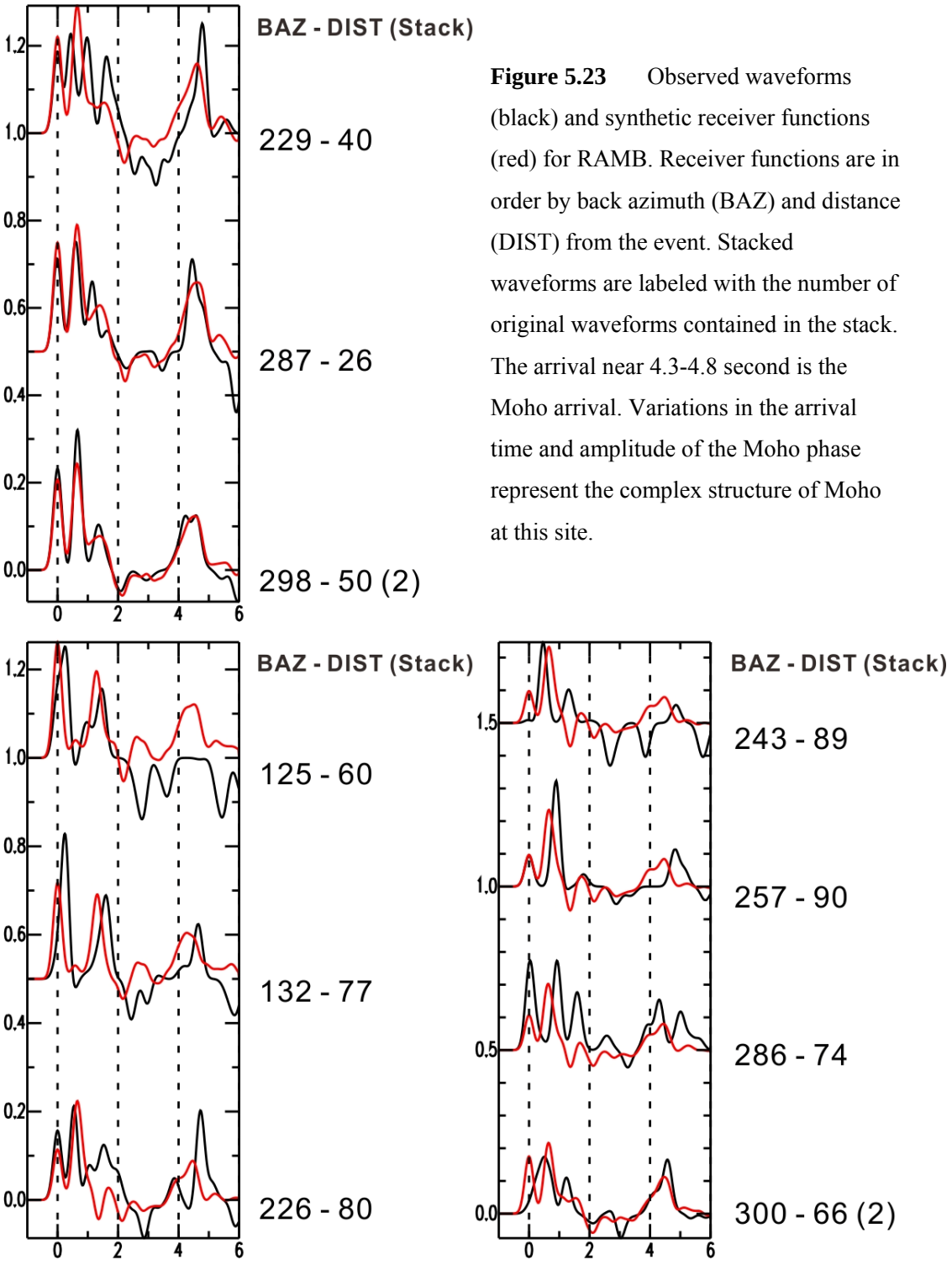

Figure 5.23 Observed waveforms (black) and synthetic receiver functions (red) for RAMB. Receiver functions are in order by back azimuth (BAZ) and distance (DIST) from the event. Stacked waveforms are labeled with the number of original waveforms contained in the stack. The arrival near 4.3-4.8 second is the Moho arrival. Variations in the arrival time and amplitude of the Moho phase represent the complex structure of Moho at this site.

The synthetics from the model (Figure 5.23) for the distant events (Δ=60-100°) do not fit as well with the observed receiver functions since it is impossible to construct a model to satisfy all receiver functions. Hence, this model is chosen as the final result for RAMB since it is compatible with the most number of observed receiver functions, especially those stacks that contain the greatest number of waveforms.

5.7 FLLB

The POLARIS seismic station FLLB is located in the southern Redstone area (51.739 N, 123.1059 W, elevation 1.189 km). FLLB is one of the stations which has a significant amount of information available from previous geophysical studies in the same area (within about 20-30 km of the station); including boreholes, active seismic studies, and an MT study (Figures 2.1 and 2.5). Two boreholes, b-82-C and d-94-G, are located 20 km and 40 km to the northwest of FLLB, respectively. Seismic lines 160-01 to 160-19 (in Block A of the first-arrival tomographic inversion result) are also in this area (Hayward and Calvert, by personal communication, 2010). In addition, Profile G and H of the MT study are located in the same region; in particular, the southwestern end of profile H is within 5 km from the station. Therefore, it is relatively straightforward to set the constraints for the near surface structure compared to most other stations in the Nechako Basin.

Based on the well description and sonic log from b-82-C and d-94-G, the Cretaceous sediments (mainly sandstone) of the Taylor Creek group overly the volcanic rocks of the Spences Bridge Group, and the mean S-wave velocity from the surface to

about 2 km depth is 2-2.5 km/s. If the layers are constrained according to the information from MT, the uppermost 10 km can be divided into 3 separate layers: the first layer from the surface to about 2 km depth with low resistivity, the second layer from 2-9 km depth, and an underlying third layer. There are a number of thrust and strike slip faults in this region, and they pass through the site location.

Similar to RAMB, due to the significant differences in the receiver functions with backazimuth and distance, it is difficult to construct one model that matches all of the data. To develop and explore possible models, I began by inverting those single receiver functions stacked from the largest number of events in the stack (for events at Δ=30-60°, the third receiver function in the top plot of Figure 5.24). The parameter limits for the inversion are based on the general broad boundaries of SULB, except that strict constraints are not applied for the minimum Vs of the top layer at FLLB.

The result of the inversion (Figure 5.25) is in good agreement with other studies; the average Vs of the top layer is about 2.7 km/s and the thickness is 2.5 km. There is nothing special for the main crustal layers other than the low velocity zone in the lower crust. This feature has been identified at all Nechako Basin stations. The low velocity zone above the Moho at FLLB is 6.8 km thick with Vs as 3.1 km/s.

Because of the low velocity zone, there is a large velocity contrast at the Moho from 3.1 km/s to 4.7 km/s. This matches the observed receiver functions which often have a sharp and strong Moho arrival (e.g. 289-31 in Figure 5.26). However, while some receiver functions show this feature, others have no or very weak Moho arrivals (e.g., 130-77 in Figure 5.26). This may be caused by varying Moho characteristics in the region or constructive/destructive multiples from other discontinuities.

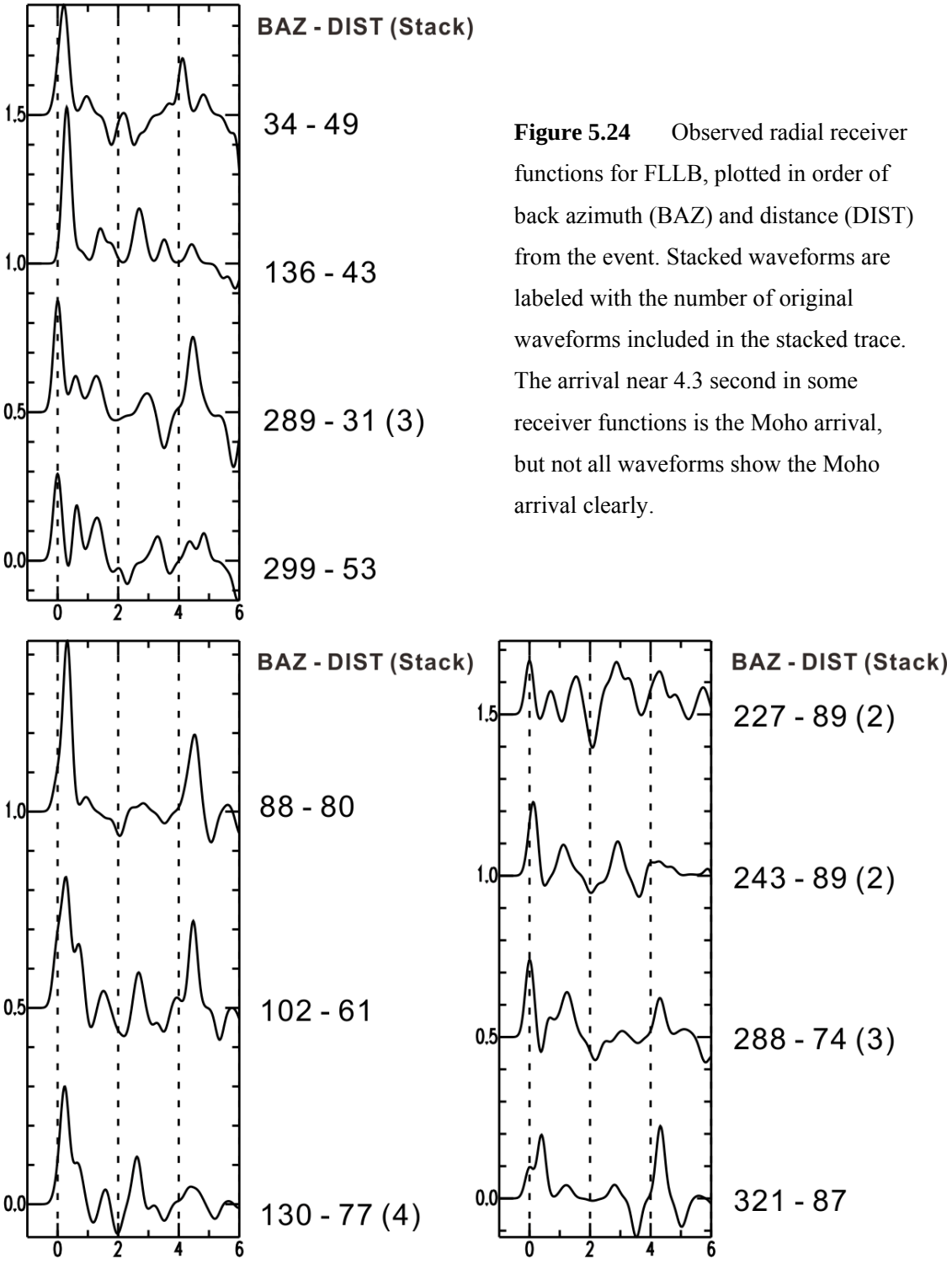

Figure 5.24 Observed radial receiver functions for FLLB, plotted in order of back azimuth (BAZ) and distance (DIST) from the event. Stacked waveforms are labeled with the number of original waveforms included in the stacked trace. The arrival near 4.3 second in some receiver functions is the Moho arrival, but not all waveforms show the Moho arrival clearly.

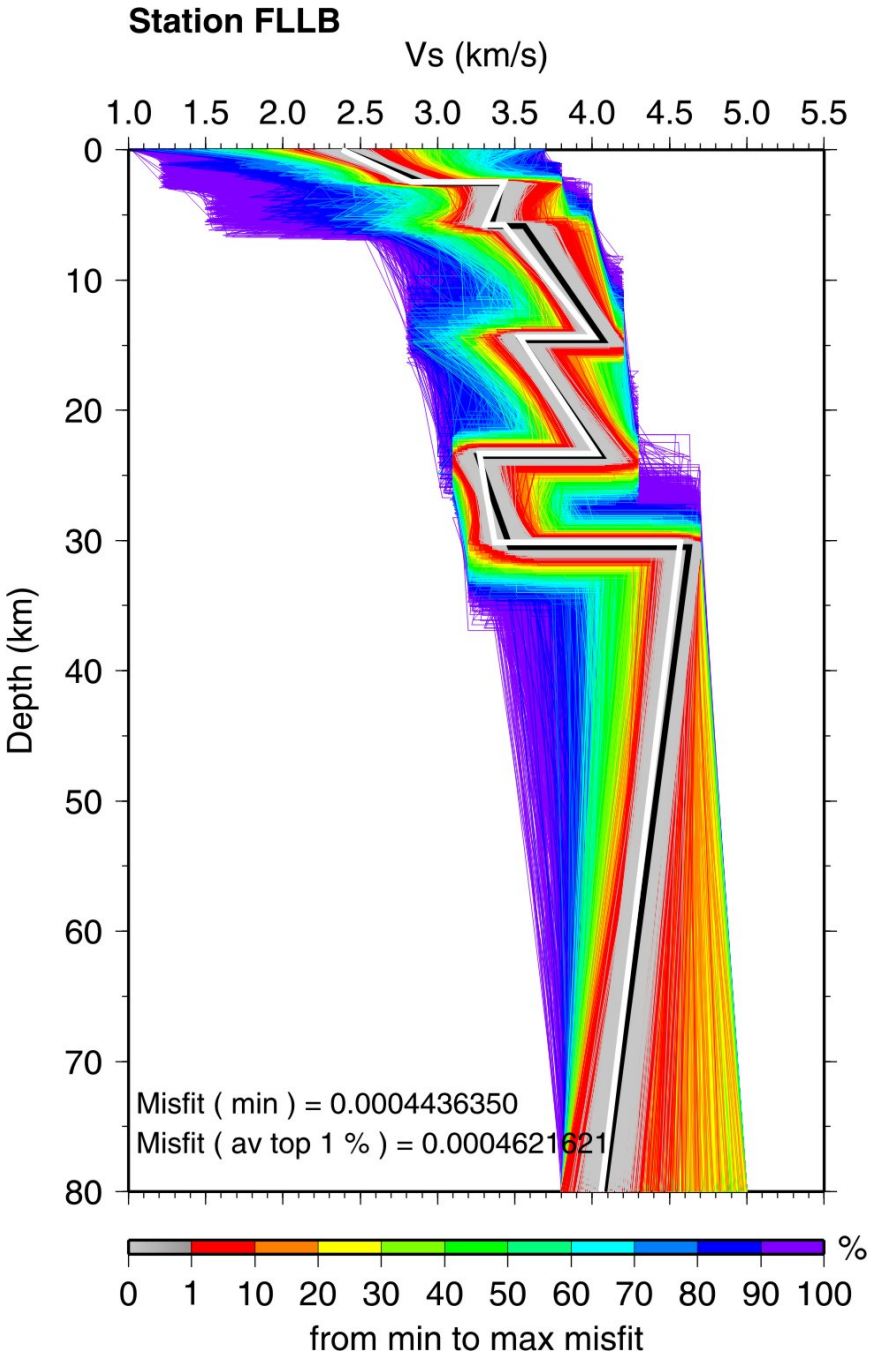

Figure 5.25 S-wave velocity model of FLLB, in terms of a density plot of the 2000 best-fitting models generated by the NA. The best-fitting model is plotted in white, and the average model computed from the 1% of models with the lowest misfit is plotted in black. The misfit of the best-fitting model and top average 1% models are given. The rainbow colour scale shows decreasing misfit, from purple to red and grey.

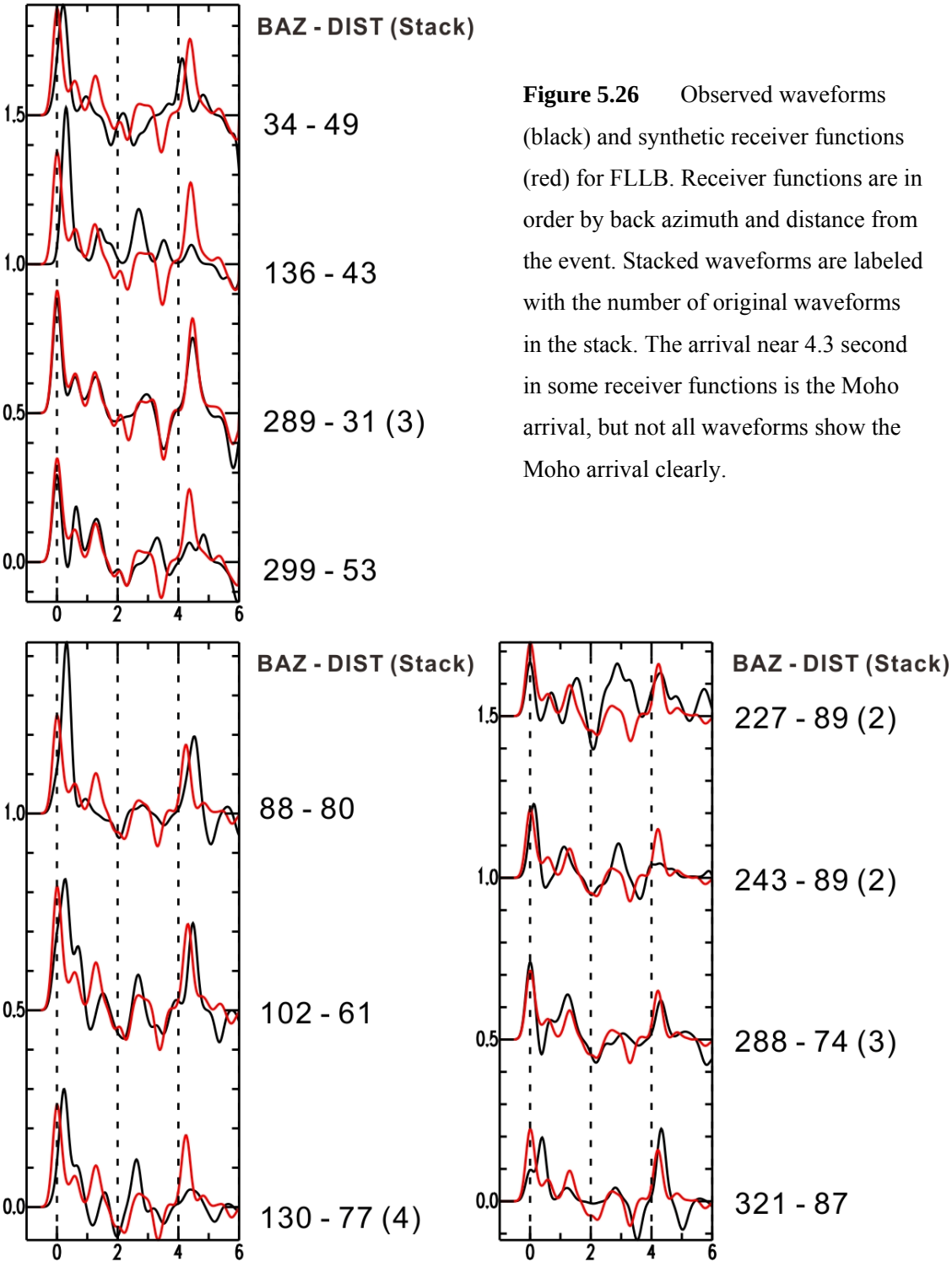

Figure 5.26 Observed waveforms (black) and synthetic receiver functions (red) for FLLB. Receiver functions are in order by back azimuth and distance from the event. Stacked waveforms are labeled with the number of original waveforms in the stack. The arrival near 4.3 second in some receiver functions is the Moho arrival, but not all waveforms show the Moho arrival clearly.

There is evidence of dipping structure underneath FLLB since only the receiver functions with back azimuths to the southeast have shifted first direct P-wave arrivals. However, both forward modeling and inversion were not successful in delineating the dipping structure.

5.8 UBRB and FPLB

Two additional stations, UBRB and FPLB, were deployed to help monitor seismic activity in the vicinity of the Nazko volcanic cone in the central Nechako basin in October and November, 2008 respectively. UBRB is located at 52.8918 N, 124.0832 W with an elevation of 1.241 km. It is about 20 km from well b-22-K to the northeast, and about 30 km from station THMB. FPLB is located near Fishpot Lake, which is close to the Nazko cone (latitude 52.954 N, longitude 123.779 W, elevation 1.005 km). Since these stations were operated for a relatively short time, there are only a few high-quality receiver functions which could be utilized for inversion..

The receiver functions for UBRB and FPLB both have double peaks for the first arrival (Figure 5.29 and Figure 5.30), likely due to near-surface sediments. The Moho arrivals are at about 4.3 s for both stations, suggesting a similar Moho depth. The inversion method was applied using a single receiver function and six horizontal layers.

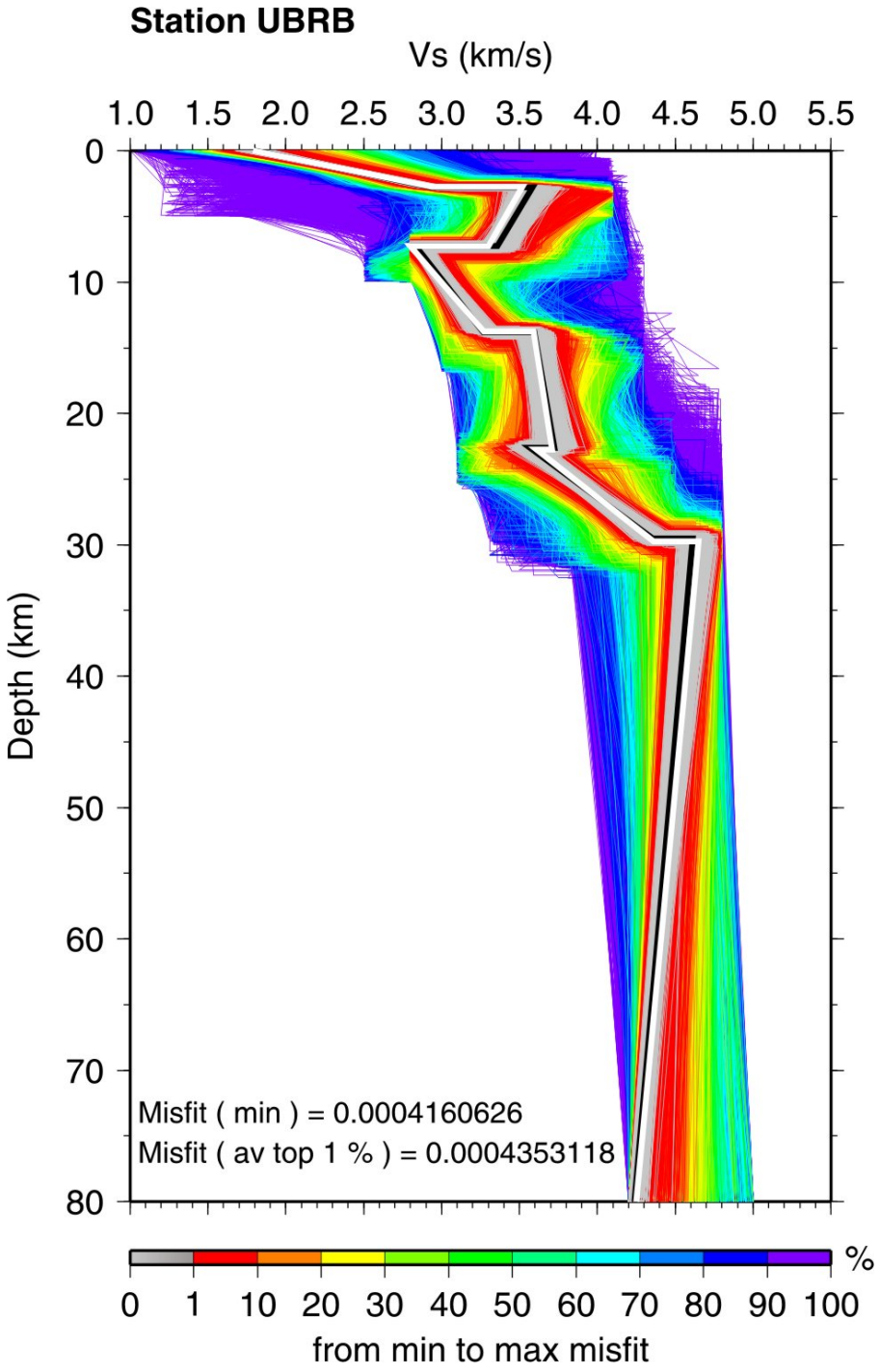

Figure 5.27 S-wave velocity model of UBRB, in terms of a density plot of the 2000 best-fitting models generated by the NA. The best-fitting model is plotted in white, and the average model computed from the 1% of models with the lowest misfit is plotted in black. The misfit of the best-fitting model and top average 1% models are given. The rainbow colour scale shows decreasing misfit, from purple to red and grey.

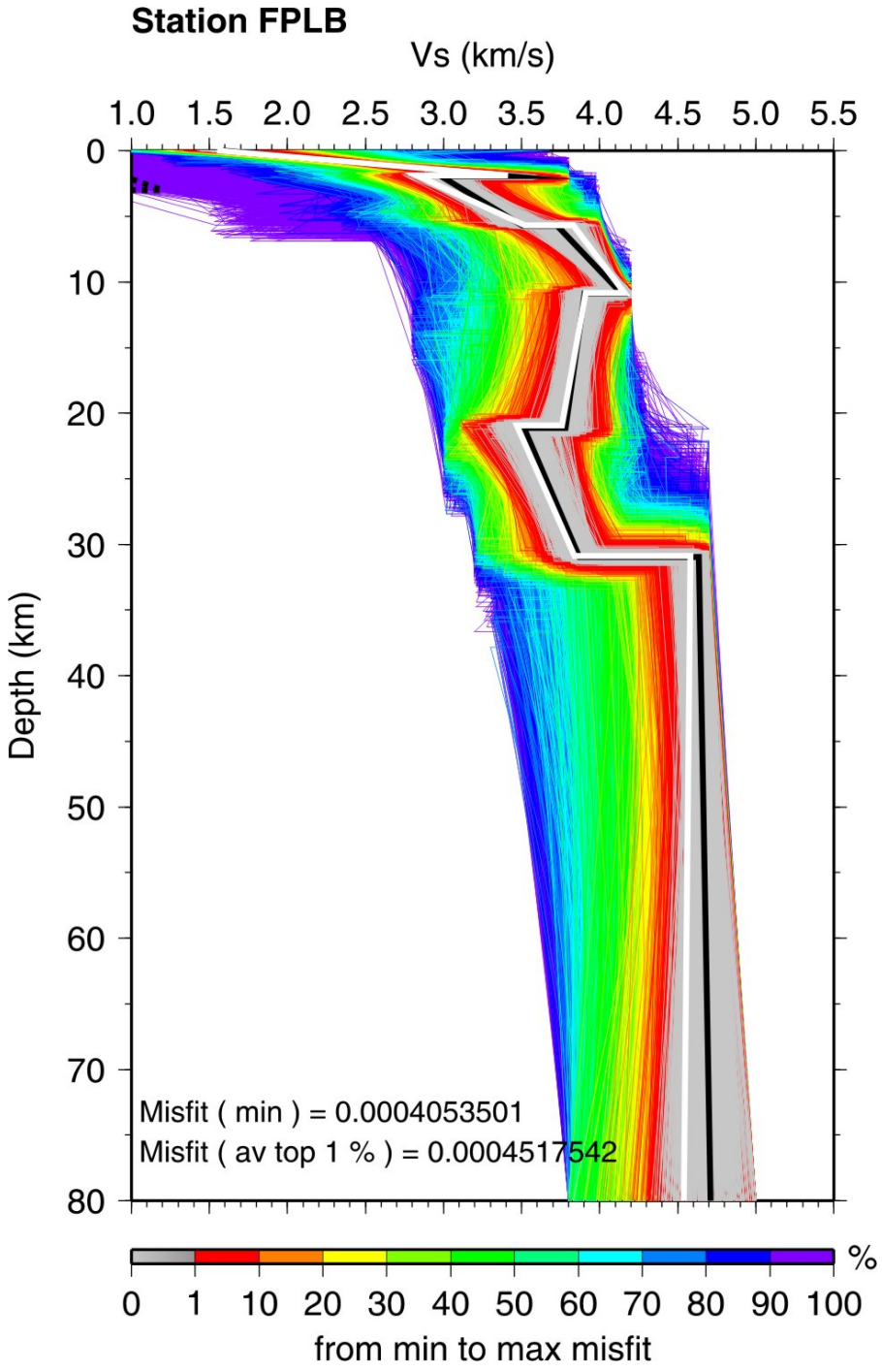

Figure 5.28 S-wave velocity model of FPLB, in terms of a density plot of the 2000 best-fitting models generated by the NA. The best-fitting model is plotted in white, and the average model computed from the 1% of models with the lowest misfit is plotted in black. The misfit of the best-fitting model and top average 1% models are given. The rainbow colour scale shows decreasing misfit, from purple to red and grey.

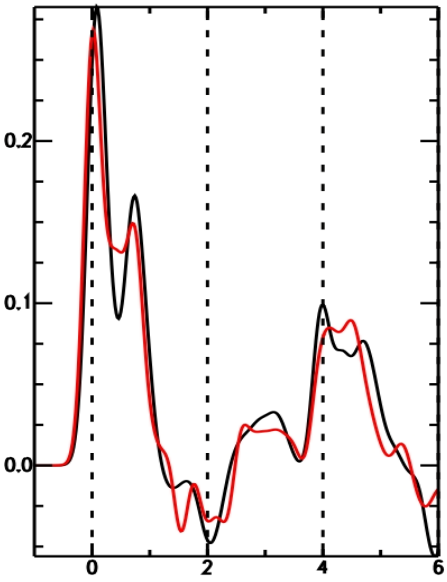

Figure 5.30 Observed waveform (black) and synthetic receiver function (red) for UBRB. This receiver function has distance 59° and back azimuth 300°, and represents a stack of 3 receiver functions. The arrival near 4.1 s is the Moho arrival.

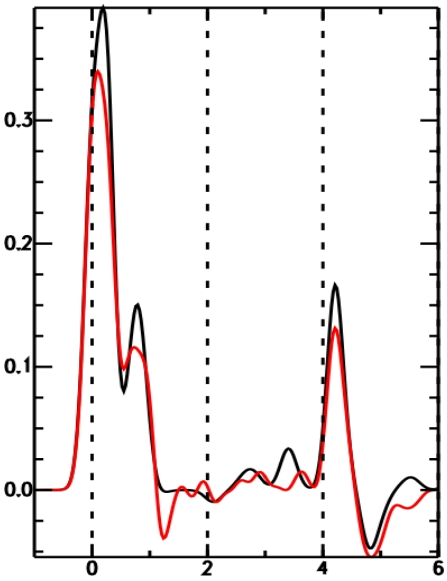

Figure 5.29 Observed waveform (black) and synthetic receiver function (red) for FPLB. This is a single receiver function whose back azimuth is 136° with distance of 43°. The arrival near 4.1 s is the Moho arrival.

The best-fitting models obtained are shown in Figure 5.27 for UBRB and 5.28 for FPLB. Both models require near-surface sediments with Vs of 1.5-1.8 km/s that are 2.7 km thick for UBRB and 1.8 km thick for FPLB. Moreover, like most other Nechako Basin stations, both models have a low velocity zone directly above the Moho. The key features of both models are similar, including the Moho depth of ~31 km.

Chapter 6 Discussion and Conclusion

It has long been recognized that the Nechako basin is a region of significant hydrocarbon and mineral potential. In this study, the receiver function method and neighborhood algorithm inversion are utilized to map the basin structure, including the shear-wave velocity and thickness of the sediments, volcanic cover and entire crust. Seven broadband seismic stations were deployed in the Nechako Basin in 2006. These were supplemented by two additional broadband stations deployed in late 2007. In this study, I analyze the data collected over a 2-year period (2006 to 2008).

6.1 Discussion

In general, the crustal models have six layers: the sediments on the surface, volcanic cover, upper, middle, lower crust, and upper mantle. Models developed for some stations have additional layers (e.g., THMB with 8 layers in total) if additional near-surface structure is required (e.g., gradients, dipping interface).

The thickness of the top sediments and the volcanic layer within the basin are shown in Figures 6.1 and 6.2, respectively. The surface sediments range in thickness from about 0.8 to 2.7 km. In general, they are the thickest in the south (FLLB) and central parts of the basin (e.g., THMB and UBRB). The volcanic layer ranges in thickness from about 2.3 to 4.7 km. In general, the volcanic layer is also the thickest in the central part of the basin, e.g., UBRB and FPLB.

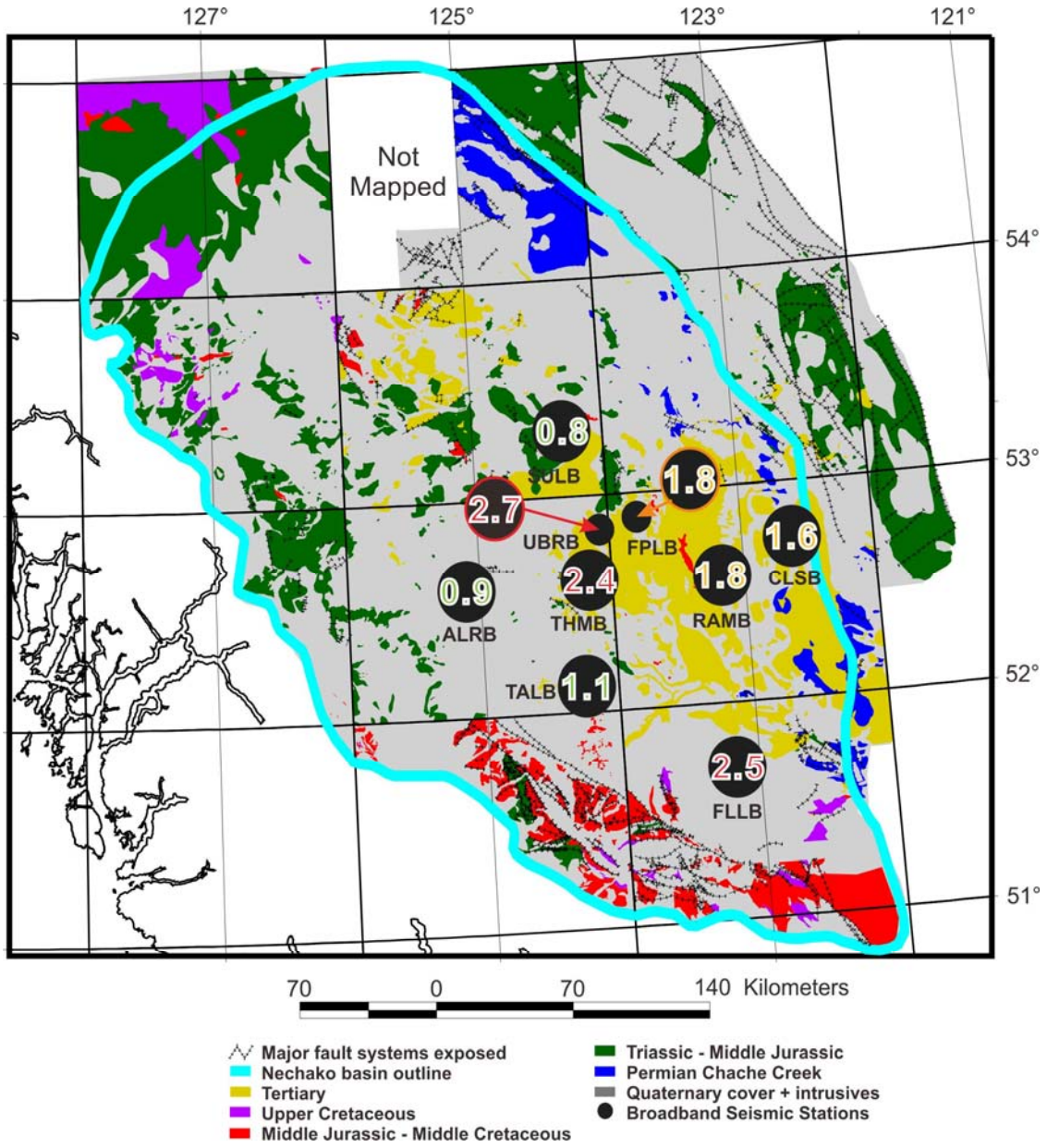

Figure 6.1 The thickness of the sediments on the surface for the final model of each seismic station in the Nechako basin (base map from Hayes et al., 2002, and modified in this study). The number in the black circles is the surface sediment thickness (in kilometers). A red number indicates thicker sediments and a green number indicates thinner sediments.

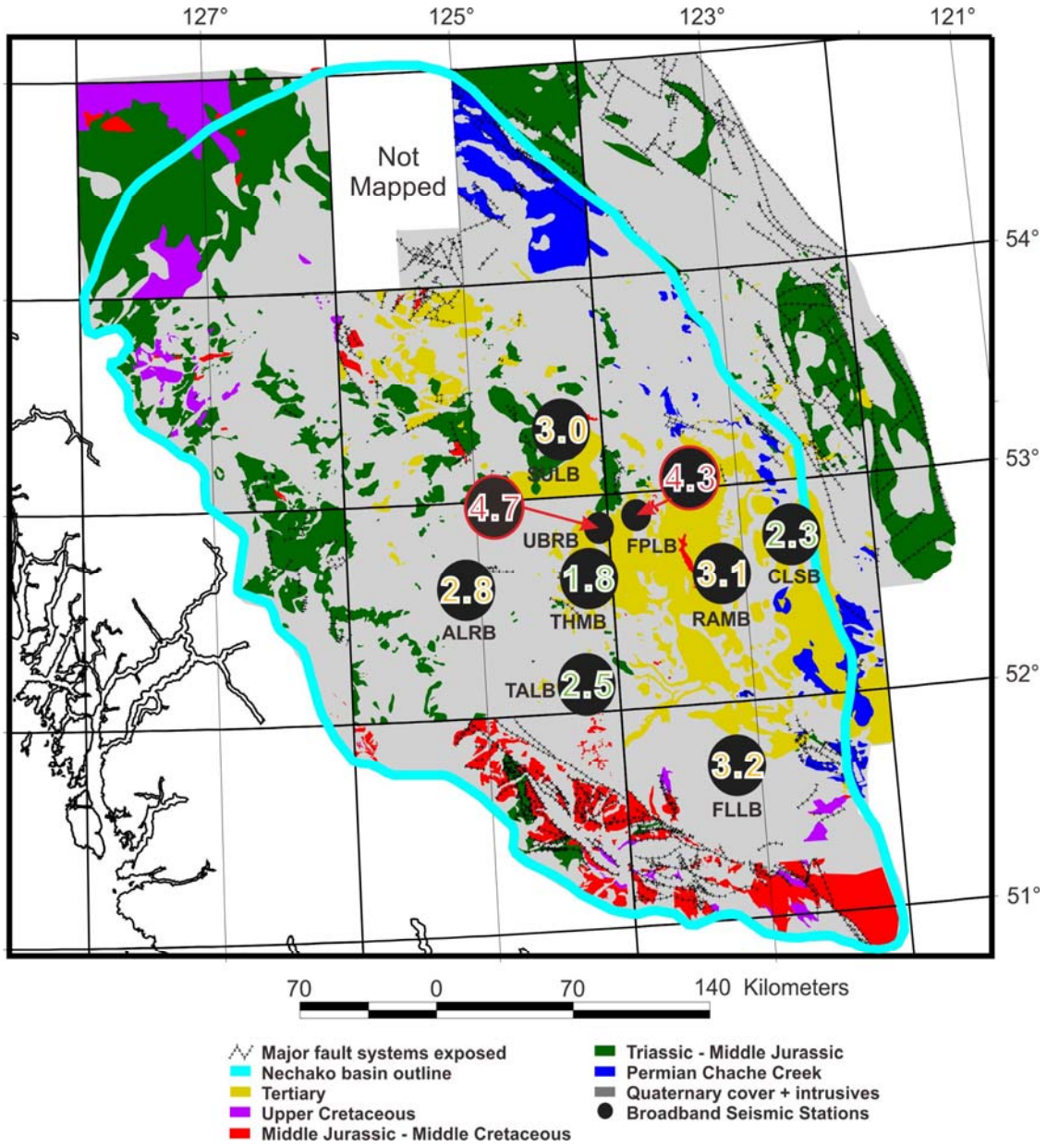

Figure 6.2 The thickness of the volcanic cover near surface for the final model of each seismic station in the Nechako basin (base map from Hayes et al., 2002, and modified in this study). The number in the black circles is the thickness of the volcanic layer (in kilometers). A red number indicates thicker volcanics and a green number indicates thinner volcanics.

The upper and middle crusts at most stations have a similar thickness; the upper crust is about 8-9 km thick and the middle crust is about 12 km thick. The two stations located in the southern part of the basin have thinner middle crust (less than 10 km). Although the upper and middle crusts have about the same thickness, the lower crust varies in thickness from about 5 km to 9 km.

The total crustal thickness (Moho depth) ranges from about 22 km to 36 km across the basin (Figure 6.3). The thickest crust is observed in the central northern part of the basin beneath station SULB and THMB with a Moho depth of 35-36 km. ALRB at the western edge of the basin also has a relatively thicker crust (34 km). In contrast, stations near the other edges of the basin have relatively thinner crusts. For example, stations CLSB and RAMB near the eastern edge have a crustal thickness of 29-31 km, and FLLB at the southern edge has a crustal thickness of 30 km. Therefore, the Nechako basin appears to have a thicker crust in the middle and western area with thinning towards the eastern and southern edges of the basin.

Station TALB appears to have an abnormal Moho depth of only 22 km. While this may be real, I have less confidence in this result for two reasons: 1) the receiver functions at this station have a complex, “ringing” appearance that may cause difficulties with the inversion program; and 2) other studies in the Nechako basin near TALB show Moho depths of about 32-34 km. The uncertainties in modeling and interpreting receiver functions for this station are discussed in detail in section 5.5.

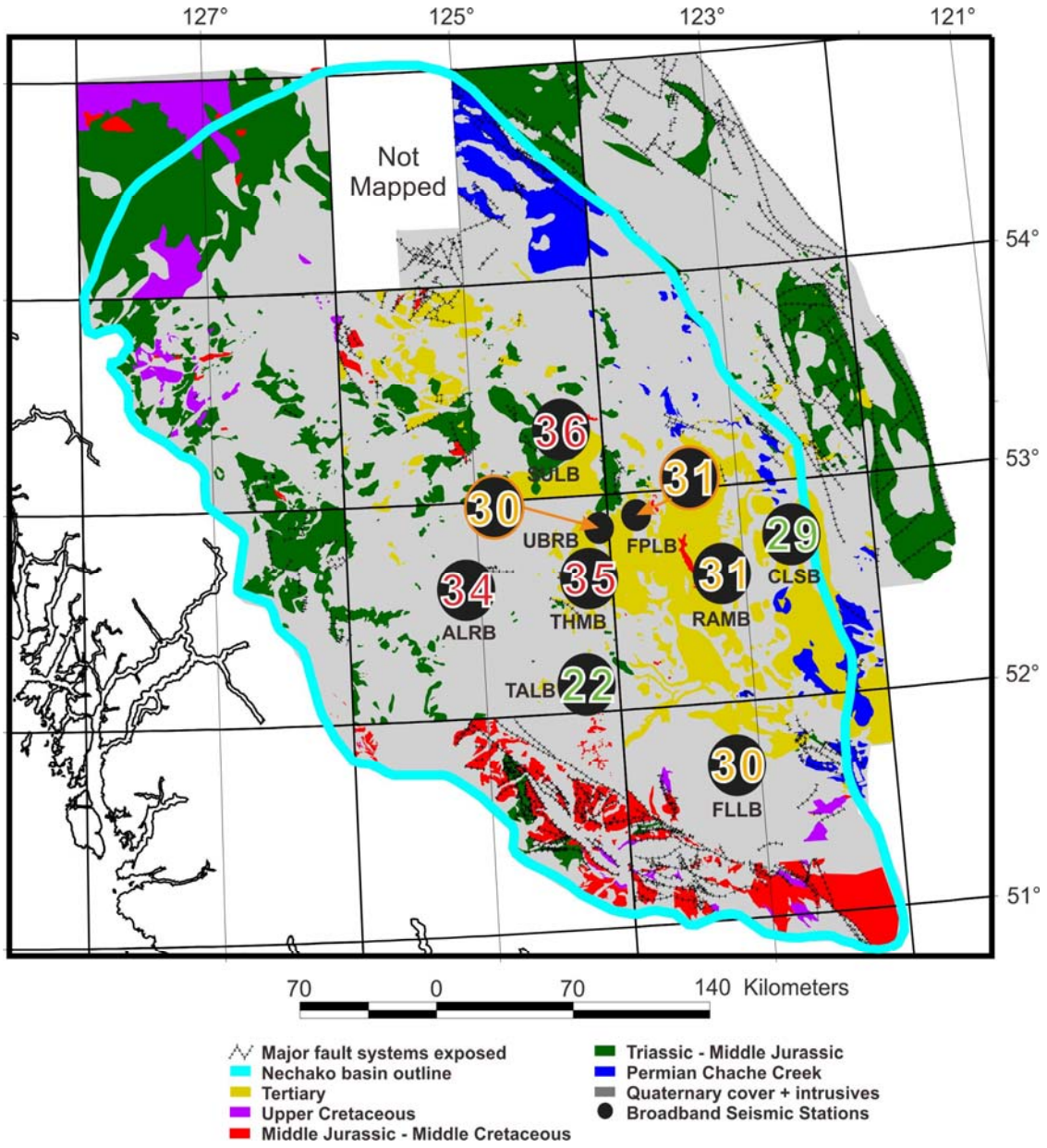

Figure 6.3 The Moho depth (total crustal thickness) from the final model of each seismic station in the Nechako basin (base map from Hayes et al., 2002, and modified in this study). The numbers in the black circles are thicknesses (in kilometers). A red number indicates a thinner crust and a green number indicates a thicker crust.

Figures 6.1 to 6.3 represent the depths of layers (sediments on the surface, volcanic cover, and the Moho respectively) in map view. This illustrates the distribution of each layer in 2-D, but it is difficult to show how the thickness of the layers change across the basin. Figure 6.4 is a cross-section of the S-wave velocity models within the basin (east-west and north-south). This represents the changing of thicknesses of layers across the basin.

The models consist of sediments, volcanic cover, upper crust, middle crust, lower crust, and upper mantle respectively from the top to bottom. Both the sediments on the surface and underlying the volcanic cover (first and second division in Figure 6.4) become thicker in the central region of the basin compare to the basin edge. However, the Moho depth (connected by the deepest red dashed line in Figure 6.4) is thicker on the west side of the basin than on the east side.

The top two layers (sediments on the surface and the volcanic cover underneath it) in this region appear to be dipping structures. Three of the stations which are located in the middle of the basin (SULB, THMB, and RAMB, shown in red in Figure 6.5) have dipping structure for the top two layers as mentioned above. The dipping directions of the surface layers at these three stations are shown as arrows in Figure 6.5. SULB and THMB, which are located in the central area of the basin, have similar dipping direction - southward dipping layers (strike direction from 86˚ to 90˚), whereas RAMB (located near the eastern edge of the basin) has westward dipping layers (strike direction around 163˚). The dip angle for the northern most station, SULB, is only 5˚-7˚, but the dip angles for THMB and RAMB are around 18˚-20˚.

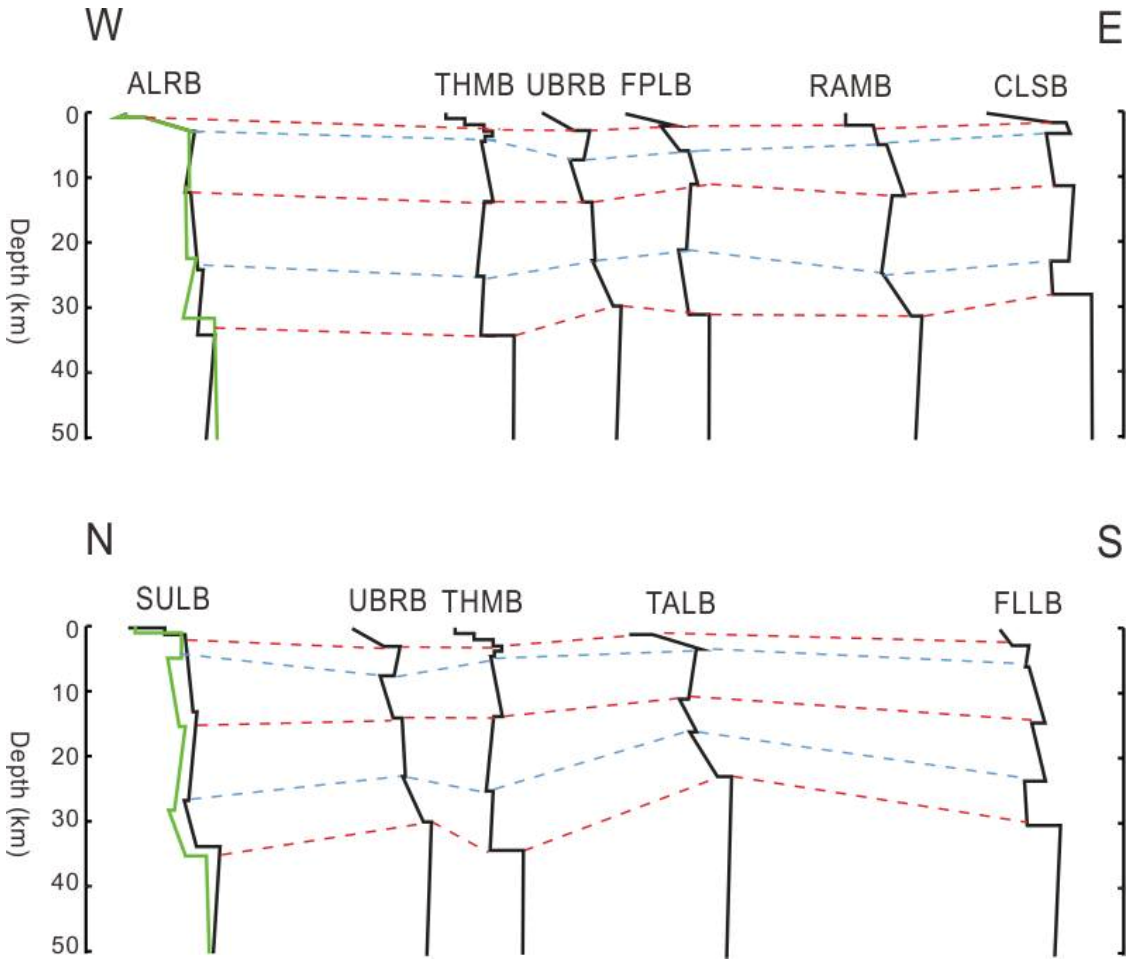

Figure 6.4 A schematic W-E (top) and N-S (bottom) cross-section of the S-wave velocity models (presented in Chapter 5.) within the Nechako Basin. The distances between stations are not to scale. The layers divided by red and blue dashed lines represent sediments, volcanic cover, upper crust, middle crust, lower crust, and upper mantle respectively from the top to bottom. As there are two best-fit models each for ALRB and SULB, one is shown in black and another in green. The dashed lines are connected the middle point of the two models.

FLLB is exceptional among all 9 stations (indicated in orange color in Figure 6.5). The receiver functions calculated for FLLB suggest the presence of dipping structure as there is an azimuthal variation in the time delay of the direct P-wave arrival. However, it is difficult to generate a single model that incorporates all of these observations. Therefore, the final model of FLLB does not include dipping layers.

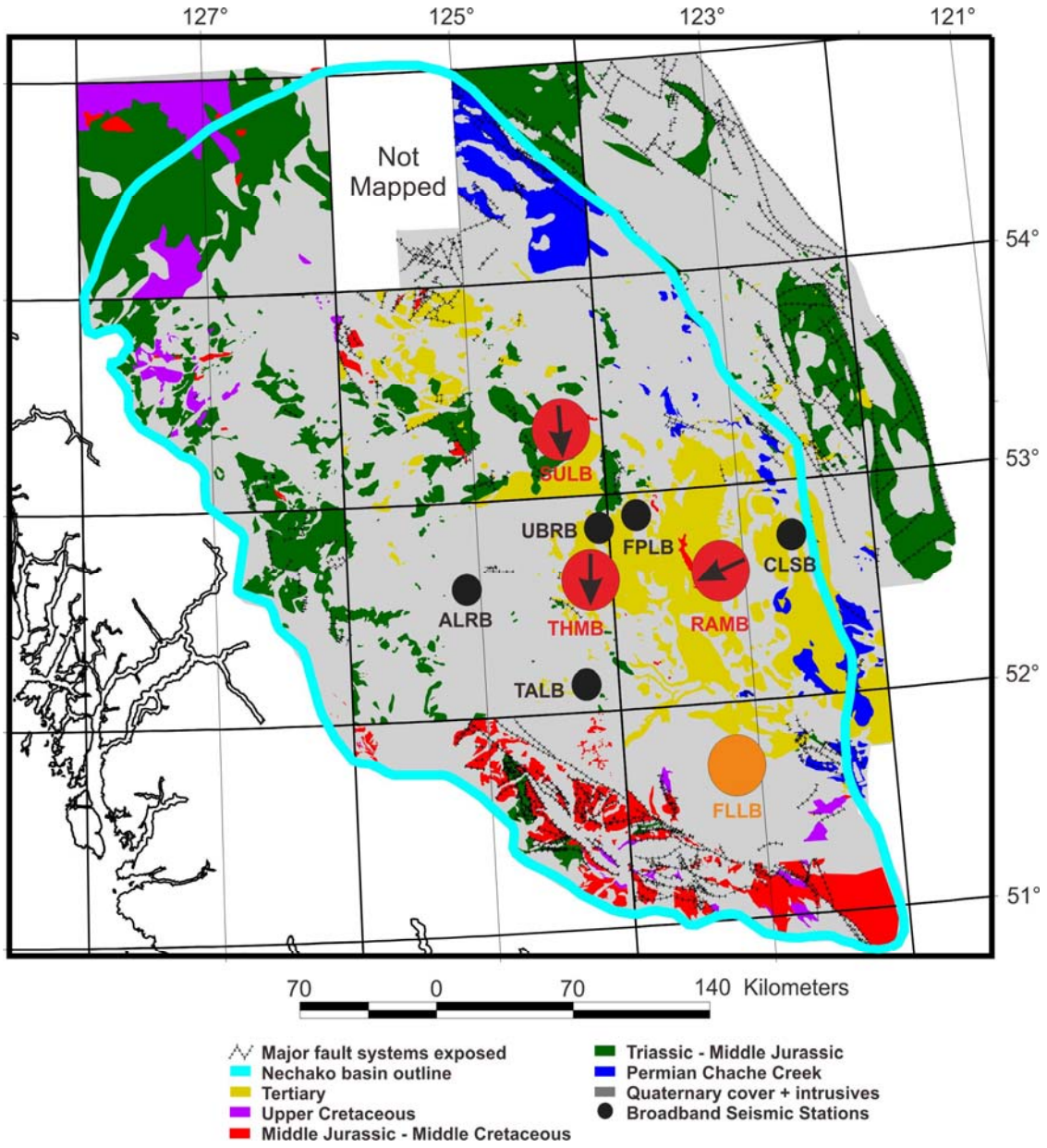

Figure 6.5 The seismic stations in the Nechako basin which have dipping structure near the surface (base map from Hayes et al., 2002, and modified in this study). The black circles indicate the stations with horizontal near-surface layers, and the red circles indicate the station with dipping structure near the surface (arrow in the red circle indicates the dipping direction). The orange-colored station (FLLB) may have dipping structure (see discussion in text).

6.2 Conclusion

This study provides site-specific images of subsurface structures in the Nechako Basin. Specifically, I determined the thickness of the sediments on the surface, the volcanic cover, and the total crust across the basin. The layer for sediments on the surface varies from 0.8 to 2.7 km thick, and the volcanic layer varies from 1.8 to 4.7 km thick. The total crustal thickness in the Nechako Basin ranges from 29 to 36 km.

A number of geophysical studies have been conducted in this area, but most of them concentrated only on the shallow structures, from the surface to 5-10 km depth: the studies which sampled the deeper structure were based on MT and ambient noise data. MT investigates the crustal structure from the surface to about 10 km depth, and the ambient noise study constructed the whole crustal model down to the Moho discontinuity. The result from MT (Spratt and Craven, by personal communication, 2010) should be similar to the result from this study since the thickness and rock property information of some top layers (surface to ~10 km depth) from MT are used as constraints (e.g. section 5.6 RAMB).

The result from the ambient study (Idowu, 2009) also has some main features which are comparable to the conclusion of this study; for example, the average Moho depth across the basin is about 30-32 km. Although the total crustal thickness is similar, each layer's thickness is different since Idowu (2009) used a different setting for his base model. Although Idowu (2009) also used six layers in his base model, he divided them differently as: low velocity sediments, high velocity volcanic cover, low velocity thin (~3 km thick) layer, upper crust, lower crust, and upper mantle. This changed the thicknesses of sediments and volcanic cover to be thinner than the result of this study. The

sedimentary layer that Idowu (2009) suggested is 0.3-1 km thick and the volcanic layer is 0.6-1.2 km thick whereas this study proposes a 0.8-2.7 km thick sedimentary layer and a 1.8-4.7 km thick volcanic layer.

Another main difference between this study and the ambient noise study is the consistent presence of a low velocity zone in the lower crust that is obtained in this study. The base model used in the ambient noise study divided the main crust into two layers (upper and lower) while the crust in this study is divided into three layers (upper, middle, and lower; lower crust is considered as the low velocity zone). There is a lot of uncertainty for this low velocity zone; it may be related to the magma in the lower crust. In 2008, an earthquake swarm was detected near the Nazko cone (UBRB was deployed on the swarm area; THMB is ~36 km away to the north). There was no seismicity in this area since 1965, but thousands of tiny (M 2-3) earthquakes occurred in 2008 at the same depth as this low velocity zone. The movement of magma in the low velocity zone (in the lower crust) may have caused this earthquake swarm by fracturing rocks (Cassidy et al., by personal communication, 2008).

Most research in the Nechako basin, carried out in the past and currently ongoing, has concentrated on imaging the near surface structures. This study complements other studies in providing information on crustal structure from the surface to the Moho. In particular, this is the first study to provide detailed constraints on S-wave velocity structure across the Nechako Basin.

Bibliography

Ammon, C. J. 1991. The isolation of receiver effects from teleseismic P waveforms, *Bull. Seism. Soc. Am.* 81, 2504-2510.

Ammon, C. J. 1997. Receiver Function Overview, Penn State University, Retrieved Dec. 2010 < http://eqseis.geosc.psu.edu/~cammon/HTML/RftnDocs/rftn01.html>

Berry, M. J. and Forsyth, D. A. 1975. A. Structure of the Canadian Cordillera from Seismic Refraction and Other Data. *Can. J. Earth Sci.* 12(2), 182-208

Best, M. E., 2004. Qualititative interpretation of potential field profiles: southern Nechako Basin. in summary of activities 2004, *BC ministry of Energy, Mines and Petroleum Resources*, 73-77.

Best, M.E., and Lankings. J., 2007. Preliminary results from a microsismic noise test utilizing passive seismic transmission tomography, *Nechako Basin (NTS 092O/11, 14), south-central British Columbia*, 243-246.

Cassidy, J. F. 1992. Numerical Experiments In Broadband Receiver Function Anaysis. *Bull. Seism. Soc. Am.* 82, 1453-1474.

Clayton, R. W. and Wiggins, R. A. 1976. Source Shape Estimation and Deconvolution of Teleseismic Bodywaves, *Geophys. J. R. astr. Soc.*, 47, 151-177.

Cosgrove, D. T. 1981. Well history report on Canadian Hunter *et al.* Redstone b-82-C/92-O-14; *B.C. Ministry of Energy, Mines and Petroleum Resources,* Well File 5680.

Cosgrove, D. T. 1986. Well history report on Canadian Hunter Redstone d-94-G/92-O-12; *B.C. Ministry of Energy, Mines and Petroleum Resources,* Well File 6438.

Fernandez-Viejo, G., Clowes, R. M., Welford, J. K., 2005. Constraints on the composition of the crust and uppermost mantle in north-western Canada: Vp/Vs variations along Lithoprobe SNorCLE trasect, *Canadian Journal of Earth Sceinces*, 42, 1205-1222.

Ferri, F., Osadetz, K., and Evenchick, C., 2004. Petroleum source rock potential of Lower to Middle Jurassic clastics, Intermontane Basins, British Columbia; in summary of activities 2004, *BC Ministry of Energy, Mines and Petroleum Resources summary of activities 2004*, 87 – 97.

Ferri, F. and Riddell, J., 2006. The Nechako Basin Project: new insight from the southern Nechako Basin; in summary of activities 2006, *BC Ministry of Energy, Mines and Petroleum Resources summary of activities 2006*, 89 – 124.

Gabrielse, H., Monger, J. W. H., Tempelman-Kluit, D. J., and Woodsworth, G. J., 1991a. Srtuctural styles, Chapter 17 in Geology. In: H. Gabrielse and C.J. Yorath (ed.), *Geological Survey of Canada*, Geology of Canada , 4, 571-675.

Gabrielse, H., Monger, J. W. H., Wheeler, J. O., and Yorath, C. J., 1991b. Part A, Morphological belts, tectonic assemblages, and terranes: in chapter 2 of the Geology of the Cordilleran Orogen of Canada. In: H. Gabrielse and C.J. Yorath (ed.), *Geological Survey of Canada*, Geology of Canada , 4, 15-28.

Gallagher, K., Sambridge, M. 1994. Genetic algorithms: a powerful tool for large-scale non-linear optimization problems *Comput. Geosci.*, 20(7/8), 1229–1236.

Hammersley, J. M. & Handscomb, D. C., 1964. Monte Carlo Methods, *Chapman & Hall, London.*

Hayes, B. J. R., Fattahi, S., and Hayes, M., 2002. The Nechako Basin-frontier potential close to home. *CSPG diamond jubilee convention proceedings*, 157 pages.

Hayward, N., and Calvert, A. J., 2008. Structure of the southeastern Nechako Basin, south-central British Columbia (NTS 092N, O; 093B,C: Preliminary results of seismic interpretation and first arrival tomographic modeling; in Geoscience BC summary of activities 2007, *Geoscience BC*, Report 2008-1, 129-134.

Holland, J. H., 1975. Adaptation in Natural and Artificial Systems, *Ann Arbor, University of Michigan Press.*

Hunt, J. A. 1992. Stratigraphy, Maturation and Source Rock Potential of Cretaceous Strata in the Chilcotin-Nechako Region of British Columbia, unpublished M.Sc. thesis, *University of British Columbia,* Vancouver, British Columbia, 448 pages.

Idowu, O. 2009. Surface wave tomography of the Nechako Basin, British Columbia, using ambient seismic noise, M.Sc. Thesis, *University of Manitoba*, Winnipeg, Manitoba, 221 pages.

Kirkpatrick, S. C., Gelatt, D. & Vecchi, M. P., 1983, Optimization by simulated annealing, *Science,* 220, 671–680.

Langston, C. A. 1977. The effect of planar dipping structure on source and receiver responses for constant ray parameter, *Bull. Seism. Soc. Am.* 67, 1029-1050.

Langston, C. A. 1979. Structure under Mount Rainier, Washington, inferred from teleseismic body waves, *J. Geophys. Res.* 84, 4749-4762.

Majorowicz, J. A., and Osadetz, K., 2008. Cordilleran Intermontane thermotectonic history and implications for neotectonic structure and petroleum systems, British Columbia, Canada. *International Journal of Earth Science*, 97, 269-287.

Monger, J. W. H., Nokleberg, W. J., 1996. Evolution of the northern North American Cordillera: generation, fragmentation, displacement and accretion of successive North American Plate margin arcs. In: Coyner, A.R., Fahey, P.L., (ed.) geology and ore deposits of the American Cordillera, Geology and ore deposits of the American Cordillera, *Geological society of Nevada Symposium Proceedings*, Reno/Sparks, Nevada, April 1995, 1133-1152.

Monger, J. W. H., Price, R. A., and Tempelman-Kluit, J. D., 1982. Tectonic accretion and the origin of the two major metamorphic and plutonic welts in the Canadian Cordillera, *Geology*. 10, 70-75.

Monger, J. W. H., Souther, J. G., and Gabrielse, H., 1972. Evolution of the Canadian Cordillera-aplate tectonic model, *American Journal of Science*, 272, 557-602.

Okabe, A., Boots, B. Sugihara, K., 1992. Spatial Tessellations Concepts and Applications of Voronoi Diagrams, *John Wiley & Sons*, *New York.*

Osadetz, K., Ferri, F., Stasiuk, L., Reyes, J., and Thorsteinsson, E., 2007. Indications for active petroleum systems in Nechako Basin, Intermontane Belt. *Intermontane Basin Workshop 2007*.

Owens, T. J. 1984 Determination of crustal and upper mantle structure from analysis of broadband teleseismic P-waveforms, *Ph.D. Thesis, University of Utah*, Salt Lake City, 146 pages.

Sambridge, M., 1999. Geophysical inversion with a neighbourhood algorithm - I. Searching a parameter space, *Geophys. J. Int.*, 138, 479-494.

Sambridge, M., Braun, J. & McQueen H., 1995. Geophysical parametrization and interpolation of irregular data using natural neighbours, *Geophys. J. Int.*, 122, 837–857.

Sen M., Stoffa, P. L., 1995. *Global* Optimization Methods in Geophysical Inversion, Advances in Exploration Geophysics Vol. 4, *Elsevier, Amsterdam.*

Stoffa, P. L., Sen, M. K., 1991. Nonlinear multiparameter optimization using genetic algorithms: Inversion of plane wave seismograms, *Geophysics*, 56, 1794–1810.

Spratt, J. E., and Craven, J., 2008. Initial results of a test survey in the Nechako Basin, B.C., designed to determine the usefulness of the Magnetotelluric method in oil and gas exploration. *2008 CSPG CSEG CWLS convention*, 707 – 711.

Shibutani, T., Sambridge, M. & Kennett, B., 1996. Genetic algorithm inversion for receiver functions with application to crust and uppermost mantle structure beneath Eastern Australia, *Geophys. Res. Lett.*, 23(14), 1829–1832.

Watson, D.F., 1992. Contouring: A Guide to the Analysis and Display of Spatial Data, *Pergamon, Oxford.*

Welford, J.K., Clowes, R.M., Ellis, R.M., Spence, G.D., Asudeh, I., and Hajnal, Z., 2001. Lithospheric structure across the craton-Cordilleran transition of northeastern British Columbia. *Canadian Journal of Earth Sciences*, 38. 1169-1189

Wickens, A.J., 1971. Variations in lithospheric thickness in Canada, *Canadian Journal of Earth Sciences*, 8, 1154 – 1162.

Wickens, A.J., 1977. The upper mantle of southern British Columbia, *Canadian Journal of Earth Science*, 14, 1100 – 1115.

Wiggins, R.A., 1969. Monte Carlo inversion of body wave observations, *J. geophys. Res.*, 74, 3171–3181.

Yorath, C.J., 1991. Upper Jurassic to Paleogene assemblages, Chapter 9 in Geology of the Cordilleran Orogen in Canada, H. Gabrielse and C.J Yorath (ed.); *Geological Survey of Canada*, Geology of Canada, 4, 329-371.

Zandt, G., Frassetto, A.M., Cassidy, J.F., Bostock, M.G., 2009. Regional variations of mantle anisotropy across the Canadian Cordillera from teleseismic shear-wave splitting, Eos Trans. AGU, 90(52), Fall Meet. Suppl., Abstract S11A-1685